Automotive Polarimetric Radar for Enhanced Road Surface Classification & Vulnerable Road User Identification

Bouwmeester, W.

DOI
10.4233/uuid:e4556562-e997-4000-add8-d9f87d9caef3

Publication date
2024

Document Version
Final published version

Citation (APA)
Bouwmeester, W. (2024). *Automotive Polarimetric Radar for Enhanced Road Surface Classification & Vulnerable Road User Identification*. [Dissertation (TU Delft), Delft University of Technology]. https://doi.org/10.4233/uuid:e4556562-e997-4000-add8-d9f87d9caef3

Automotive Polarimetric Radar for Enhanced Road Surface Classification & Vulnerable Road User Identification

Automotive Polarimetric Radar for Enhanced Road Surface Classification & Vulnerable Road User Identification

Dissertation

for the purpose of obtaining the degree of doctor
at Delft University of Technology
by the authority of the Rector Magnificus, Prof. dr. ir. T.H.J.J. van der Hagen,
chair of the Board for Doctorates
to be defended publicly on
Wednesday 18 September 2024 at 17:30 o'clock

by

Wietse BOUWMEESTER

Master of Science in Electrical Engineering,
Delft University of Technology, The Netherlands
born in Sneek, The Netherlands

This dissertation has been approved by the promotors.

Composition of the doctoral committee:

Rector Magnificus,	chairperson
Prof. Dsc. A. Yarovoy	Delft University of Technology, promotor
Dr. F. Fioranelli	Delft University of Technology, promotor
Independent members:	
Prof. dr. ir. G.J.T. Leus	Delft University of Technology
Prof. dr. ir. H.J.W. Russchenberg	Delft University of Technology
Dr. ir. R.F. Remis	Delft University of Technology
Prof. dr. C. Silveira Vaucher	Delft University of Technology / NXP, NL
Prof. dr. L. Ferro-Famil	Université de Toulouse / ISAE-SUPAERO, FR

This research has been carried out at the Delft University of Technology in the Microwave Sensing, Signals and Systems (MS3) group

Keywords: Automotive Radar, Polarimetry, Road Surface, Vulnerable Road Users.

Printed by: Proefschriftspecialist, 1506RZ Zaandam, The Netherlands.

Front & Back: Design by Wietse Bouwmeester.

ISBN/EAN: 978-94-6384-626-4 (Paperback/Softback)
ISBN/EAN: 978-94-6384-628-8 (E-Book/PDF)

An electronic version of this dissertation is available at
`http://repository.tudelft.nl/`.

Author e-mail: wietse.bouwmeester@gmail.com

Foar Pake, Heit en Mem.

Contents

List of Acronyms

ABS	Anti-lock Breaking System
ADAS	Advanced Driver Assistance Systems
ADC	Analog to Digital Converter
CNN	Convolutional Neural Network
CT	Computer Tomography
EM	Electromagnetic
ESC	Electronic Stability Control
FFT	Fast Fourier Transform
FMCW	Frequency Modulated Continuous Wave
H	Horizontal
KA	Kirchhoff Approximation
LNA	Low Noise Amplifier
MIMO	Massive Input Massive Output
MoM	Method of Moments
MLFMM	Multilevel Fast Multipole Method
ND	Negative Diagonal
NRCS	Normalised Radar Cross Section
PA	Power Amplifier
PD	Positive Diagonal
RCS	Radar Cross Section
RMS	Root Mean Square
RTS	Radar Target Simulator
RX	Receiver
SAR	Synthetic Aperture Radar
SNR	Signal to Noise Ratio
SPM	Small Perturbation Method
SUT	Surface Under Test
TDM	Time Domain Multiplexing
TX	Transmitter
V	Vertical
VNA	Vector Network Analyser
VRU	Vulnerable Road User

Summary

Due to recent advances in miniaturisation and cost reductions of radar systems, an increasing amount of vehicles is equipped with automotive radar systems to enable advanced driver assistance systems (ADAS) which improve driving comfort and road safety. Examples of these systems include automatic braking as well as adaptive cruise control. To advance the capabilities of these systems and to take another step towards enabling autonomous driving, the next generation of radar sensors aims to enhance the situational awareness of the driver and the vehicle by, amongst others, classifying objects in the surrounding area of the car. Arguably, the most important objects to correctly classify in this process are vulnerable road users (VRUs).

With the largely completed transition of automotive radar systems from the previously used 24 GHz band to the new 77 GHz band, the performance of automotive radar systems has improved further due to larger available bandwidths and reduced wavelengths. The reduced wavelengths allow for an increased angular resolution with the same aperture size while the increased bandwidth results in enhanced range resolution. However, all currently commercially available automotive radar systems are single-polarised and therefore do not consider an important source of information, namely the polarisation state of the backscattered radiation, which can benefit classification of objects greatly.

To gain better insight in the benefits of this factor, this thesis is concerned with investigating the effectiveness of polarisation information for classification of objects in the automotive scenario. In particular, two types of objects are considered, namely road surfaces and their conditions, as well as vulnerable road users.

Chapter 2 considers the scattering of electromagnetic waves from road surfaces. Measurements on multiple different road surface materials are performed and their electrical properties are determined. These measurement results are subsequently used to simulate scattering from road surfaces at mm-wave frequencies using numerical methods. Also, a new method for computing the range-Doppler signature of road surfaces in dynamic scenarios is proposed.

In chapter 3, to accompany the numerical results from the previous chapter, a method is developed to determine statistical polarimetric radar cross section models of road surfaces at mm-wave frequencies. Measurements are performed and the radar cross section models of several types of surfaces and road surface conditions are determined. These models are subsequently used to simulate polarimetric backscattering from road surfaces as well as to determine the optimal sensing wave polarisation to be used for single-polarised radar systems.

Chapter 4 considers the classification of road surfaces and road surface conditions using H, α, and A features. For the first time, these features are adapted for road surface classification purposes in the automotive scenario and it is shown that these features can benefit surface classification.

Chapter 5 shifts the attention from classification of road surface conditions to classification of vulnerable road users. In order to do this, a novel automotive polarimetric MIMO radar system with corresponding signal processing algorithms has been developed and is presented in this chapter. This radar is subsequently used for measurements of moving VRUs and several features are considered to classify them. It is demonstrated that polarimetric information is indeed able to increase classification perfomance of VRUs compared to single polarised radar.

This thesis demonstrates that polarimetric radar is useful in the automotive scenario besides the fields in which it has already been established such as synthetic aperture radar and meteorological radar applications. The methods proposed within this dissertation can be used to enhance classification accuracy of road surface condition which may lead to improvements in road safety by for example enhancing the performance of anti-lock breaking systems. Also, the methods proposed in this thesis to use polarimetric information for classifying vulnerable road users are shown to improve classification performance of this type of objects which could help enable autonomous driving in the future.

Samenvatting

Door recente ontwikkelingen in de miniaturisering en het goedkoper worden van radarsystemen, worden voertuigen in toenemende mate uitgerust met automobiele radarsystemen om advanced driver assistance systems (ADAS) mogelijk maken en daarmee het comfort en veiligheid te vergroten. Voorbeelden van dergelijke systemen zijn automatische remsystemen en adaptive cruise control. Om de mogelijkheden van deze system verder uit te breiden en een stap dichter bij autonoom rijden te komen, richt de volgende generatie radarsystemen zich op het vergroten van de omgevingsbewustheid van de bestuurder en het voertuig zelf door onder andere objecten in de omgeving van de auto te classificeren. De belangrijkste objecten om hierbij correct te classificeren zijn wellicht kwetsbare weggebruikers.

De prestaties van automobiele radarsystemen zijn verder verbeterd door de grotendeels voltooide transitie van automobiele radarsystemen van de in het verleden gebruikte 24 GHz band naar de nieuwe 77 GHz band vanwege de grotere beschikbare bandbreedte en kortere golflengtes. Kortere golflengtes leiden namelijk tot een hogere hoekresolutie met dezelfde apertuurgrote en grotere bandbreedtes zorgen voor een betere afstandsresolutie. Desalniettemin, alle huidige commercieel beschikbare automobiele radarsystemen zijn enkelvoudig gepolariseerd en kunnen daarom niet de informatie gebruiken die in de polarisatiestaat van de teruggekaatste golf zit. Deze informatie kan de classificatie van objecten verbeteren.

Om beter inzicht te krijgen in de voordelen die deze factor oplevert, wordt in dit proefschrift de effectiviteit van polarisatieinformatie voor het classificeren van objecten in de automobiele omgeving onderzocht. Hierbij worden met name twee type objecten onderzocht, namelijk wegoppervlaktes en hun condities, en ook kwetsbare weggebruikers.

Hoofdstuk 2 richt zich op de terugkaatsing van elektromagnetische golven van wegoppervlakten. Metingen van verscheidene wegoppervlaktes worden gedaan en de elektrische eigenschappen van deze oppervlaktes worden bepaald. Deze meetresultaten worden vervolgens gebruikt om terugkaatsing van wegoppervlaktes op mm-golflengtes te simuleren met numerieke methodes. Ook wordt een nieuwe methode voorgesteld om de afstand-Doppler signatuur van wegoppervlaktes in dynamische scenario's te berekenen.

In hoofdstuk 3 wordt een methode ontwikkeld om statistische polarimetrische radardoorsnedes van wegoppervlaktes te bepalen om de resultaten van het vorige hoofdstuk aan te vullen. Metingen worden gedaan en de radardoorsnedes van verscheidene wegoppervlaktes worden vastgesteld. Deze modellen worden vervolgens gebruikt om polarimetrische terugkaatsing van wegoppervlaktes te simuleren, alsmede om de optimale polarisatie van een tastgolf voor een enkelvoudig gepolariseerd radarsysteem te bepalen.

Hoofdstuk 4 beschouwt classificatie van wegoppervlaktes en wegcondities door middel van H, α en A kenmerken. Voor het eerst worden deze kenmerken aangepast voor gebruik in classificatie van wegoppervlaktes in automobiele toepassingen en wordt aangetoond dat deze kenmerken de wegoppervlakteclassificatie ten goede komt.

Hoofdstuk 5 verschuift de aandacht van classificatie van wegoppervlaktes naar classificatie van kwetsbare weggebruikers. Om dit te bewerkstelligen werd een nieuw automobiel polarimetrisch MIMO radarsysteem met bijbehorende signaalverwerkingsalgoritmes ontwikkeld dat gepresenteerd wordt in dit hoofdstuk. Deze radar wordt vervolgens gebruikt voor metingen van bewegende kwetsbare weggebruikers en verschillende kenmerken worden onderzocht om hen te classificeren. Er wordt gedemonstreerd dat polarimetrische informatie inderdaad in staat is om de classificatieprestaties van kwetsbare weggebruikers te verbeteren in vergelijking met enkelvoudig gepolariseerde radar.

Dit proefschrift demonstreert dat polarimetrische radar ook nuttig is in automobiele toepassingen naast gevestigde toepassingen zoals synthetic aperture radar en meteorologische radartoepassingen. De methodes die in dit proefschrift voorgesteld worden, kunnen gebruikt worden om de classificatieprestaties van wegoppervlaktes te verbeteren wat tot verbeteringen in veiligheid kan leiden door bijvoorbeeld de prestaties van antiblokkeersystemen te verbeteren. Ook laat deze thesis zien dat de in dit proefschrift voorgestelde methodes om gebruik te maken van polarisatieinformatie voor het classificeren van kwetsbare weggebruikers de classificatieprestaties voor dit type object verbetert wat in de toekomst zou kunnen helpen om autonoom rijden mogelijk te maken.

Preface

While I was writing this preface, sitting at my desk on the 20th floor, I was struck with a sudden thought. While I was looking out of the window, enjoying the view from one of the highest vantage points in Delft, I realised that this dissertation is not only the culmination of the four years of research work corresponding to this PhD project, but that it also is the end of the 11 years that I have spent studying in Delft.

Looking back on those 11 years, it has been an interesting path, certainly not one that I had imagined when I first arrived in Delft in 2013. It has taken me to many interesting places, where I met many new friends and where I did many great things. The path has had its ups and downs, but the mean gradient was certainly positive. This last sentence I write with a little tear and a big smile, as this sentence marks both the end of a beautiful chapter and the beginning of a brand new one.

Wietse Bouwmeester
Delft, August 2024

1

Introduction

1.1. Automotive Radar

Arguably, the car is one of mankind's most important inventions. It has revolutionised the way we get around and the distances that we can easily and quickly cover. The car has transformed how economies operate and has had huge impact on the way we construct our cities and infrastructure.

However, with the advantages that the car brings, such as greatly reduced travel times, there are also downsides. One of these important downsides is safety. Collisions involving cars are one of the leading, if not number one, cause of injury related deaths. Even though throughout the century new safety measures have been introduced such as air bags and seat belts, which have reduced the amount of serious injury drastically, as of 2023 still 1.19 million people were killed in traffic accidents globally [1]. Especially, with the increasing amount of sold vehicles due to the rise of China's and India's welfare levels, without additional safety measures one can only expect the amount of accidents to increase. Therefore, increasing automotive safety is paramount.

With the technological progress that has taken place during the last century, new safety features were made possible, such as anti-lock breaking systems (ABS) and electronic stability control (ESC). Currently, we find ourselves in a very interesting point in time where more and more aspects of driving become automated and fully autonomous vehicles seem to be on the horizon instead of merely being an idea taken straight out of science fiction. To enable this increasing degree of automation found in advanced driver assistance systems (ADAS), and perhaps to enable fully autonomous driving in the near future, advancing the degree to which a vehicle is able to percept its environment is key. Luckily, due to technological improvements a new type of sensor has become available which is well suited to tackle this problem. This sensor is radar. [2]

Due to innovations in electronics, radar sensors can nowadays be miniaturised and produced cheaply. This development has made radar much more widely applicable, in contrast to the for example large, powerful, and expensive radar systems found in military applications. This has lead to the fact that many cars are already equipped with radar systems nowadays, which enable ADAS features like automatic breaking and adaptive cruise control.

With the largely completed transition of automotive radar systems from the previously used 24 GHz band to the new 77 GHz band, performance of radar sensors can be improved further due to larger available bandwidths and reduced wavelengths. The increase in bandwidth results in better range resolution while the reduction of the wavelength allows for higher angular resolution for a given aperture size than at 24 GHz. These enhancements make more ADAS functions possible as they enable a better perception of the environment.

1.2. Research Question and Approach

Even though radar polarimetry has proven to be very effective in the previously mentioned applications, it has not found its way to commercial automotive applications yet. Also, the literature on polarimetric automotive radar is far from extensive, especially at 77 GHz. Therefore, the goal of this thesis is to extend the state-of-the-art of this research area to further determine how useful the extra information provided by polarimetric radar in automotive scenarios is. This could assist designers of automotive radar systems to make a better trade-off between dedicating radar channels to implement polarimetry or dedicate them to increase angular resolution in the traditional sense as is done currently.

However, as automotive polarimetric radar can be used for many different applications and could provide benefits in many different automotive scenarios, about which many dissertations could be written, this thesis specifically considers the use of polarimetry for the purposes of identifying and classifying road surface conditions and vulnerable road users (VRUs). Therefore, the central question in this thesis is:

> *"How effective is mm-wave polarimetric radar in automotive scenarios for identifying road surface conditions and classifying vulnerable road users?"*

To answer this question, a number of key questions need to be considered first. These questions are:

1. How do road surfaces and VRUs scatter electromagnetic radiation?

2. How can polarimetry be used to identify and classify road surfaces and VRUs based on their scattering behaviours?

3. How do the classification results from fully and partially polarimetric radar compare to those of single-polarised radar for VRUs and road surface conditions?

The approach taken in this thesis is to consider these key question in this order since the answer from the previous question is required to answer the next question. Each key question itself comprises a number of questions. For example, to answer the first question, *"How can scattering from VRUs and road surface conditions be simulated?"*, *"How can scattering from VRUs and road surface conditions be measured?"*, and so on and so forth.

1.3. Main Results and Novel Contributions

The main results achieved in this PhD thesis are listed here.

- For the first time, statistical full-wave numerical results of scattering from road surfaces in automotive scenarios in the W-band are presented.

- A novel road surface scattering modelling method for mm-wave automotive radar systems based on a dense grid of uncorrelated scattering elements has been introduced.

- A new measurement procedure has been proposed for measuring normalised radar cross sections of rough surfaces, showing that road surfaces have distinct polarimetric normalised radar cross sections depending on their condition.

- A novel road surface condition classification method based on an adapted polarimetric $H\alpha A$-decomposition has been introduced that exploits the differences in the statistical properties of polarimetric scattering of various road surface conditions.

- For the first time, it has been shown that the dynamic polarimetric signatures of cyclists and pedestrians are structured and differ significantly from each other.

1.4. Thesis Outline

The remaining part of this thesis is organised as follows. First, the modelling, measuring, and classifying electromagnetic scattering at mm-wave frequencies from road surface conditions is considered. Afterwards, the thesis considers measurements of scattering from vulnerable road users and classification of such targets.

Chapter 2 - *Polarimetric Scattering from Road Surfaces*
In this chapter, scattering of electromagnetic waves from road surfaces is considered. Measurement procedures and results on the electrical properties of road surface materials is presented. Furthermore, a numerical method to simulate scattering from road surface materials at mm-wave frequencies is described. Lastly, a numerical method is introduced for computing the dynamic radar signatures of road surfaces as observed by an automotive radar system.

Chapter 3 - *Polarimetric NRCS Road Surface Models and its Applications in Automotive Radar*
In this chapter, a measurement procedure is presented to measure and formulate normalised radar cross section models of road surfaces in automotive scenarios. This measurement procedure is subsequently performed on multiple types of road surfaces under various weather conditions. Furthermore, two applications of the measured normalised radar cross section models are presented. Firstly, a procedure to synthesise road surface clutter is described, that can be used to efficiently simulate clutter caused by road surfaces in automotive radar simulation software. Secondly, a method is introduced for determining the optimal sensing wave polarisation to be used in single-polarised automotive radar systems, for either rejecting or enhancing (certain types of) road surface returns.

Chapter 4 - *Classification of Road Surfaces using Polarimetric H/α/A Features in Automotive Scenarios*
This chapter introduces a new method to classify road surfaces based on backscattered radiation received by a polarimetric radar system. The classification method is based on entropy (H), alpha angle (α), and anisotropy (A) features that have also proven to be effective in other radar applications, which have been adapted to the automotive scenario. The signal processing pipeline to compute these features in the automotive scenario is described and subsequently applied to measurements of an asphalt road surface in various conditions. Lastly, also the convergence of these features is discussed.

Chapter 5 - *Vulnerable Road User Recognition using MIMO Polarimetric Radar*
A new polarimetric MIMO automotive radar is presented in this chapter. This new radar is used to measure polarimetric returns from three classes of vulnerable road users, namely cyclists, pedestrians, and a motorcyclist. Subsequently, the measurement data is processed and analysed to evaluate the effectiveness of polarimetric radar for classification of VRUs. In this analysis, the mean polarimetric ratio for each radar frame corresponding to the measured target is considered for this purpose, as well as the distribution of the polarimetric ratios of the invidual detections that comprise the total extended target that the vulnerable road surface user presents.

Chapter 6 - *Conclusions and Recommendations for Future Research*
This chapter presents the conclusions and major contributions to the state-of-the-art provided by this thesis. Also, recommendations for future research projects that continue on the work presented in this thesis are listed.

2

Polarimetric Scattering from Road Surfaces

The first step in successfully classifying road surfaces in various conditions at mm-wave frequencies is to study how these targets scatter the electromagnetic fields emitted by the automotive radar. Namely, this information is essential for designing and determining the effectiveness of classification algorithms. This data can be obtained in two ways: numerical analysis and experimental measurements. This chapter is concerned with numerical analysis, while the following chapters are concerned with gathering surface scattering data through experimental measurements.

Parts of this chapter have been published as:

W. Bouwmeester, F. Fioranelli, and A. Yarovoy, "Dynamic Road Surface Signatures in Automotive Scenarios", in *2021 18th European Radar Conference (EuRAD)*, London, United Kingdom, 2022.

2.1. Introduction

Currently, radars are widely used in autonomous vehicles to realise functionalities like adaptive cruise control and all-weather assisted driving. Throughout the years, several frequency bands have been made available for automotive radar purposes, starting with the 24 GHz band and nowadays the main 77-81 GHz band. At these higher frequencies, more bandwidth is available, which results in better range resolution [3]. Furthermore, the higher frequency, and therefore smaller wavelength of the electromagnetic radiation, results in a size reduction for the antennas, but also changes the scattering behaviour of targets. For instance, a road surface may act as a flat smooth surface at 24 GHz, while it could appear rough at 79 GHz. Thus, at 24 GHz the road surface would not be detectable by radar as the radiation is scattered in the forward direction, while at 79 GHz some backscattering may occur.

This presents an unique opportunity to enhance the performance of road safety and driving comfort systems such as anti-lock breaking and traction control. Namely, if these systems could be provided with an estimation of the road surface conditions up ahead, they can already be set to expect a specific surface friction coefficient and therefore find more quickly their optimal control inputs. In the case of anti-lock breaking, this could result in a quicker stop. Furthermore, in the case of autonomous driving, potential hazards such as puddles of water or patches of ice could even be avoided altogether by exploiting the backscattering from road surfaces for automatic classification purposes.

In this chapter, a method is presented to compute the signature of road surfaces, which can be exploited in future research to automatically identify dangerous surfaces (e.g. patches of water and ice) ahead of the vehicle. This method considers road surface scattering from the radar's point of view and takes the dynamics of the automotive scenario into account. This fills the gap in literature for road surface scattering in dynamic scenarios as previous research has mainly focused on road surface scattering in the static case [4], [5]. Besides this, other research in the area of road surface classification has been measurement-focused ([6], [7]), whereas the method developed here may be used for a more analytical approach to road surface classification, and thereby gain more physical insight in this challenging scattering problem. The presented method is also able to take undulations in the road surface in account.

This rest of this chapter is structured as follows: first, the electrical properties of the various road surface materials are determined in section 2.2. To perform Monte-Carlo simulations on many digital asphalt surface samples, a method to synthesise random rough surfaces with certain properties is, together with a numerical method to evaluate surface scattering, discussed in section 2.3. Section 2.4.3 describes how to use RCS models of road surfaces to numerically compute their dynamic range-Doppler signatures. Finally, the chapter closes with conclusions.

2.2. Electrical Parameters of Asphalt

To accurately model road surface materials, its electrical properties need to be known. The relevant electrical parameters of a material to evaluate its surface scattering properties are its permittivity and its conductivity. While measurements of dielectric permittivity of road surfaces have been undertaken before, literature on the subject of the exact permittivity and conductivity of asphalt at high frequency is relatively limited. In Table 2.1, a few values

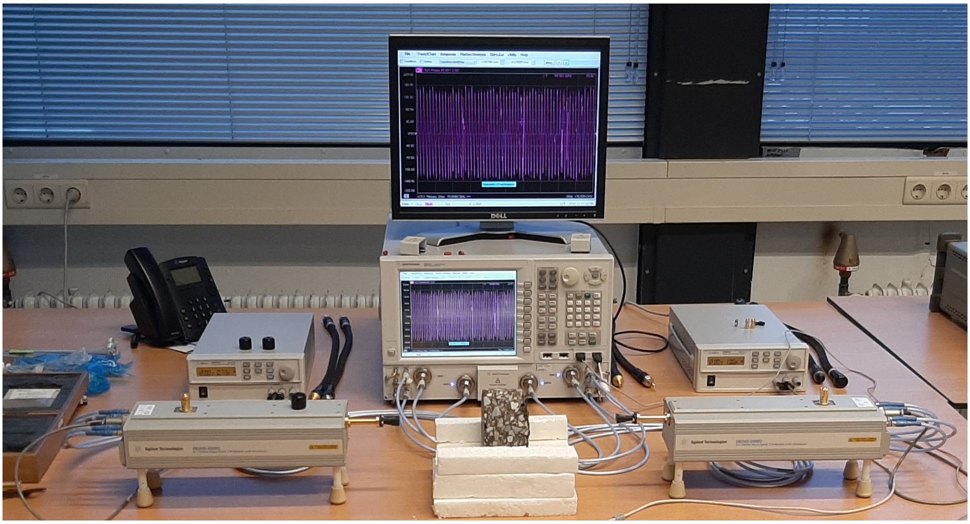

Figure 2.1: Measurement setup for measuring the permittivity of a road surface sample.

Table 2.1: Comparison of measured values of the permittivity of asphalt by various authors.

Author	Frequency	ϵ'	ϵ''
Peake [8]	Ka-band	2.5	0.6
Kulemin [9]	136 GHz	2.55	0.18
Sarabandi [4]	94 GHz	3.3	0.1
Schneider [10]	77 GHz	4.4	0.3

found from literature are shown.

As can be seen from this Table 2.1, results vary from publication to publication. An explanation for the variability of the values of the permittivity and conductivity of asphalt is that it may also depend heavily on the specific mix used. As rough surface scattering may distort the permittivity measurement, measurement differences may also arise from the way authors dealt with the compensating for this effect. As very few measurements of the permittivity of asphalt and other road surfaces have been performed before at frequencies in the 77 GHz band, new measurement results are presented in this chapter.

As permittivity determines the attenuation and speed of a wave travelling through a material, this parameter can be measured by means of transmission measurements. A picture of the measurement setup used to conduct these transmission measurements is shown in Fig. 2.1. The measurement setup comprises of a N5242A Vector Network Analyser (VNA) with two N5260-60003 frequency extenders, equipped with horn antennas, enable measurements in the frequency band ranging from 75 to 85 GHz. As can be seen from Fig. 2.1, the sample-under-test is placed on a styrofoam jig to ensure the beam is centred on the sample. Also, the distance between the horn antennas and sample is selected in such a way there there is minimal amount of antenna beam spillover while far-field conditions are maintained.

After a short-open-load-through calibration, the first step in the measurement procedure

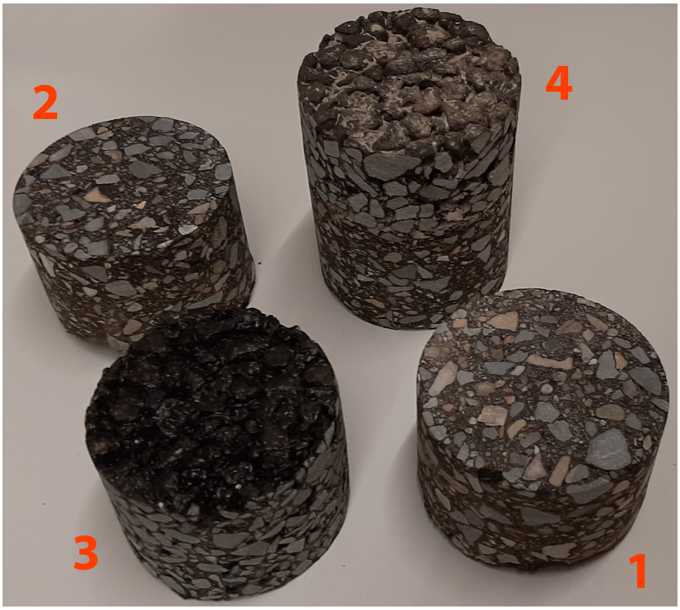

Figure 2.2: Asphalt samples of which the permittivity is measured. The samples are labelled 1 to 4.

was to collect reference measurements of free-space propagation by performing a measurement without the to-be-measured sample present in the styrofoam jig. Styrofoam was used as it has a permittivity that is close to that of air and thus should not influence the measurements significantly. This reference measurement is used to determine the additional attenuation and propagation delay introduced by the sample-under-test, from which its permittivity and conductivity can be determined. Subsequently, measurements were performed on various road surface samples. These measurements included 4 types of asphalt and 3 types of brick. Also, a sample made out PTFE was measured to validate the measurement procedure as the permittivity of this material is well-known. A picture of the measured asphalt samples is shown in Fig. 2.2.

The real part of the permittivity, which determines the propagation speed of a EM wave travelling through a medium, can thus be determined by finding the extra propagation delay caused by the sample-under-test with respect to the free-space reference measurement. As a VNA performs measurements in the frequency domain, to find this extra time delay, first the S-parameter measurements of the VNA are converted to time domain by means of an inverse Fourier transform. The results of this procedure for the free-space reference measurement is shown in Fig. 2.3.

Subsequently, the delay introduced by a sample-under-test can be found by convolving its corresponding time domain measurement with the time domain transformed reference measurement. The result of this procedure for the PTFE sample is shown in Fig. 2.4. From the time delay, indicated by Δt, the real part of the relative permittivity, denoted by ϵ_r', can be found using (2.1) as the length of the sample l_{sample} is known. Furthermore, in (2.1), c

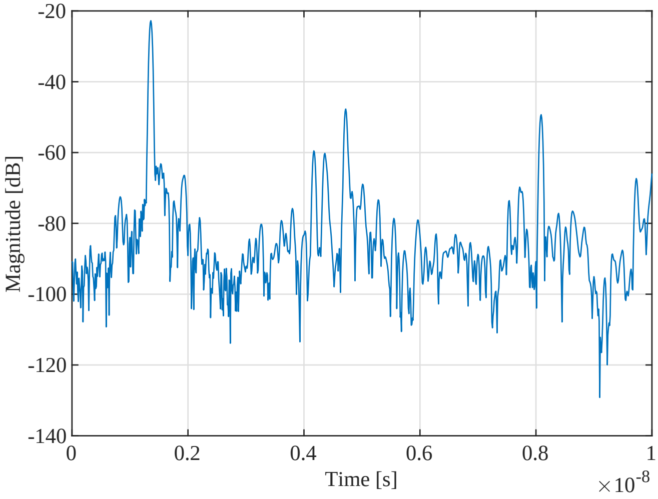

Figure 2.3: Measurement results of the free-space reference measurement converted to time domain.

indicates the propagation speed of EM-waves in free space.

$$\epsilon_r' = \left(\frac{c\Delta t + l_{sample}}{l_{sample}}\right)^2 \tag{2.1}$$

It should be noted that the time resolution is dependent on the bandwidth setting of the VNA. For these measurements, the measurements were performed in the W-band, at frequencies ranging from 75 to 110 GHz. This also implies that effective permittivity over the entire W-band is measured instead of a frequency dependent measurement.

Using the described measurement procedure, the real part of the relative permittivity of the PTFE sample was found to be 2.05. This corresponds well to results from literature and therefore it can be concluded that this measurement method is valid. The measurement procedure was subsequently repeated for the road surface samples. The measurement results are shown in table 2.2.

In this table, ”Inverted” means that the sample has been rotated by 180° so that the wave propagates from back to front instead of the other way around. The brick samples are either measured horizontally or vertically. Horizontal indicates that the brick is placed on the jig in such a way that it is laying on its largest side. Vertical means that the brick is laying on its second largest side. Furthermore, Translated indicates that the sample has been moved on the jig so that the antenna beam illuminates another part of the sample. Lastly, wet indicates if the sample has been wetted to simulate the effects of rain.

A first observation that can be made from table 2.2 is that the measured bricks and asphalt samples are quite isotropic as the translated and inverted measurements results are very close to each other. There is however an observable difference between the bricks when measured horizontally and vertically. This is likely due to the brick not covering the antenna beam completely while performing the measurement.

A second observation that can be made is that there does not seem to be a significant

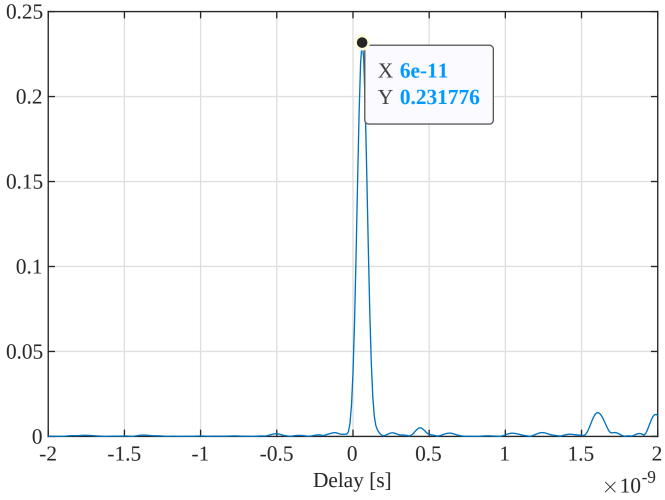

Figure 2.4: Measurement of a PTFE cylinder after matched filtering.

Table 2.2: Measurment results of the real part of the relative permittivity of various road surface materials.

Sample	Real part of Relative Permittivity
PTFE Reference	2.1
Asphalt 1	4.8
Asphalt 2	4.1
Asphalt 2 (Inverted)	4.2
Asphalt 3	4.3
Asphalt 3 (Wet)	4.1
Brick 1 (Horizontal)	3.0
Brick 1 (Horizontal, Translated)	3.0
Brick 1 (Vertical)	3.9
Brick 1 (Vertical, Translated)	3.9
Brick 5 (Horizontal)	3.4
Brick 5 (Vertical)	4.6
Brick 5 (Vertical, Wet)	4.4
Brick 6 (Horizontal)	3.6
Brick 6 (Vertical)	4.8

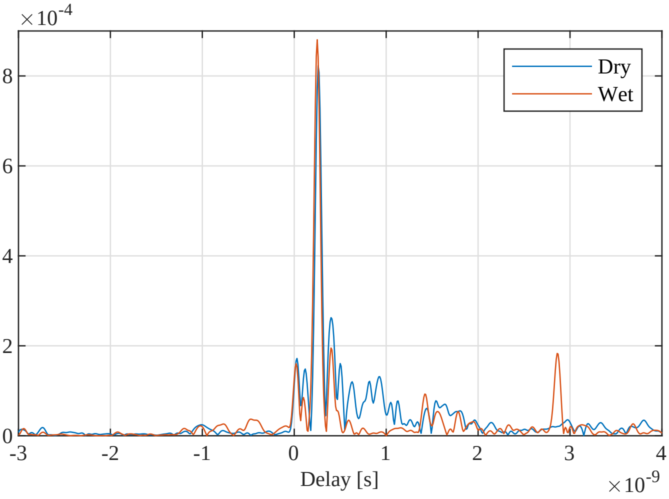

Figure 2.5: Comparison of matched filtered output for the wet and dry measurement of the asphalt 3 sample.

difference between the wet and dry samples. This could be explained by the fact that most asphalt road surfaces are designed to be porous so that water quickly drains from it to keep roads from becoming slippery. This was also observed when pouring the water on the sample as it would almost instantly drain out. Fig. 2.5 shows a comparison of the matched filtered output of the wet and dry samples. It can be seen that the wet sample causes a strong multipath reflection which is likely caused by the high conductivity of the remaining thin water layer that stuck to the sample when the majority of the water had drained out.

Now that the real part of the permittivity is known, the conductivity which is related to the complex part of the permittivity, can be computed. To compute the conductivity of the measured asphalt material, a new method of computing conductivity was devised. Since the measured asphalt sample is a very lossy medium in the measured frequency range, the power lost due to the sample-under-test can be modelled by three electromagnetic interactions.

The first interaction occurs when the transmitted power reaches the air-to-asphalt interface. Namely, due to the difference in permittivity between air an asphalt, part of the power is reflected back to the transmitting antenna. The second interaction is the attenuation of the wave that penetrated the air-asphalt interface. This attenuation results from the conductivity of the medium.

Lastly, the wave propagating inside of the sample reaches the asphalt-to-air interface at the back of the sample and again a portion of the power is reflected towards the transmitting antenna. This reflected wave is attenuated again during propagation back to the first interface. Due to the asphalt being very lossy, by the time this wave reaches the first interface, it has become strongly attenuated that its contribution to the received power can be neglected. In a material that is not very lossy, this approximation would not hold as this second internal reflection is not negligible and will cause in turn a third reflection. This third reflection will in turn cause a fourth reflection and so forth. This creates a standing wave inside the material that must be taken into account when computing conductivity of materials with low losses.

Thus the losses L_{total} caused by the asphalt can be modelled as shown in equation 2.2.

$$L_{total} = \frac{1}{1-\Gamma_{air\to asphalt}} L_{propagation} \frac{1}{1-\Gamma_{asphalt\to air}} \tag{2.2}$$

In this equation, $\Gamma_{a\to b}$ represents the lost power due to reflection for a wave travelling from medium a to medium b. Furthermore, $L_{propagation}$ represents the losses caused by the conductivity of the material.

The reflected power can be computed using equation 2.3.

$$\Gamma_{a\to b} = \left|\frac{\eta_b - \eta_a}{\eta_b + \eta_a}\right|^2 \tag{2.3}$$

In this equation η_a represents the characteristic impedance of medium a which can be computed using equation 2.4.

$$\eta_a = \frac{j\mu\omega}{\gamma} \tag{2.4}$$

Here, μ is the permeability of the material and omega the angular frequency of the propagating wave. The parameter γ is the propagation constant of the material which can be calculated using equation 2.5.

$$\gamma = j\omega\sqrt{\mu\epsilon}\sqrt{1-\frac{j\sigma}{\omega\epsilon}} \tag{2.5}$$

In this equation, ϵ is the real part of the permittivity of the medium and σ is the conductivity of the medium.

The propagation losses can be computed as shown in (2.6).

$$L_{propagation} = e^{2Real(\gamma)d} \tag{2.6}$$

In this equation, d is the thickness of the sample.

Putting these equations together and solving the equation numerically for a measured L_{total} = 46.8 dB, results in a conductivity of 0.767 S/m for the measured asphalt sample.

This value was subsequently validated by performing a simulation of the measurement set-up. This resulted in a simulated measured loss of 45.5 dB, which is similar to the actual measured value of 46.8 dB. Therefore, it can be concluded that a value of 0.767 S/m is an accurate estimate of the conductivity of the asphalt sample and that the three-interaction model is a valid approximation.

2.3. Numerical Simulations on Road Surface Scattering

2.3.1. Generation of Surface Realisations

The first step in setting up the numerical simulation is to define the road surface model. To simulate real asphalt surfaces as closely as possible, first the statistical properties of the

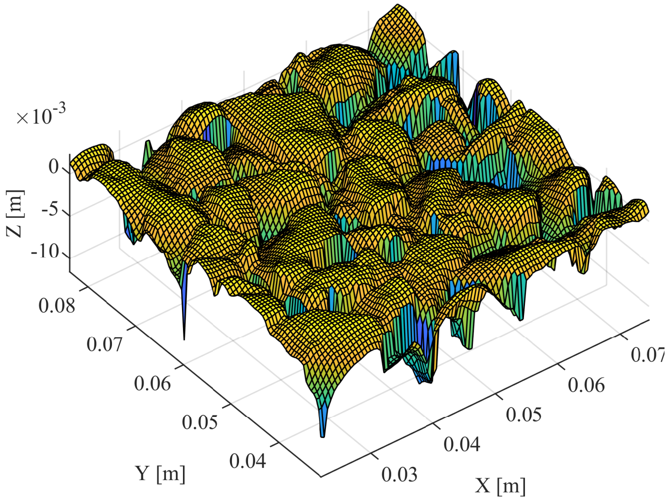

Figure 2.6: Digitised asphalt road surface sample.

surface geometry of a real asphalt road surface sample need to be determined. This was done by digitising the surface profile of an asphalt sample from a CT-scan, provided of the Pavement Lab of the CITG faculty of TU Delft. From this digitised surface shown in Fig. 2.6, it is determined that the RMS height of this scanned sample is 2.1 mm and that its correlation length is 2.2 mm. It should be noted that at a frequency of 79 GHz, these statistical properties are more than half a wavelength and thus surface roughness should be taken in account.

Since the asphalt surface geometry differs from patch to patch, the RCS may differ from patch to patch as well. Therefore, the statistical properties of the NRCS of the road surface should be determined. In order to do this, a Monte-Carlo approach is taken. In this method, the RCS of many surface samples is determined to find the statistical properties. However, the digitisation of asphalt surface profiles using CT-scans is a complex and expensive process, infeasible for all possible surfaces, and thus an alternative way to obtain realisations of asphalt road surface samples needs to be considered. Therefore, a method is developed that allows for generating synthetic asphalt surface samples based on the statistical properties found from the digitised surface that was obtained by CT-scan.

This method works by generating a random uniformly distributed surface which to which which is subsequently filtered in the spatial spectral domain. This shape of the this filter can be computed by using the Wiener-Khinchin theorem. This theorem states that the Fourier transform of a signal's auto-correlation function equals the power spectral density of said signal. This theorem can also be used for surfaces, where a surface can be considered as a space-varying signal instead of a time-varying signal. From this, it can therefore be seen that the Fourier transform of a surface correlation function equals the spatial power spectral density of the surface, which can be used to base the spectral filter on. Using this method, not only surfaces with Gaussian correlation functions, but also surfaces with exponential or other correlation functions can be generated. Finally, probability transforms are applied to achieve the correct cumulative distribution function of the surface heights. A stepwise description of this procedure is shown below. The impact of these transforms on the correlation function of the surface is minimal and thus surfaces with arbitrary height distributions and correlation functions can be generated.

1. Generate normally distributed random surface with a variance selected such that its spectrum has a magnitude of 0 dB on average.
2. Compute the spectral filter from the target surface correlation function using a Fourier transform.
3. Apply filter to the spectrum of the generated normally distributed random surface.
4. Transform the filtered surface back to spatial domain by means of an inverse Fourier Transform.
5. Use an inverse integral probability transform followed by a regular probability transform to obtain the desired surface height distribution.

To demonstrate effectiveness, Fig. 2.7 shows a comparison of the requested correlation function and the actual achieved correlation function of a generated surface. As can be seen, the target correlation function and actual correlation function of the generated surface are almost exactly the same. Furthermore, also new surface realisations of arbitrary size with the same statistical properties as the scanned asphalt sample can be generated. Such a generated asphalt sample is shown in 2.8. It can be seen from this figure that the synthesized surface looks similar to the scanned surface model shown in 2.6. Fig. 2.9 shows a comparison of the probability density functions and cumulative distribution functions of the synthesized and scanned surface model. As can be seen, excellent agreement between the PDF/CDF of the input and synthesized models is obtained, thus further demonstrating the effectiveness of the developed surface synthesis method.

2.3.2. Numerical Simulation Procedure

To perform numerical simulations of surface scattering from asphalt road surfaces, the commercially available FEKO software package was used. This software package contains a full-wave solver based on the Method of Moments (MoM) and Multi-Level Fast Multi-pole Method (MLFMM) which is suitable to simulate scattering from large model meshes.

To set up the numerical simulations in FEKO, first the synthesised surface model is imported. As the MoM/MLFMM solver requires closed surface models, the synthesised surfaces are converted to closed volumes by adding walls and a bottom surface to them. The thickness of the bricks were selected such that standing wave interactions at the top surface are negligible as reflections from the bottom air-asphalt interface are attenuated sufficiently due to the losses caused by the conductivity of the asphalt material. To evaluate the fully polarimetric NRCS, the source was rotated by 90° to create orthogonally polarised sensing waves.

Subsequently, the source of the incident radiation is defined. A source comprising an array of linear dipoles was selected to provide a strongly polarised incident waves. Furthermore, the dipole elements were given binomial weights to eliminate side lobes so that

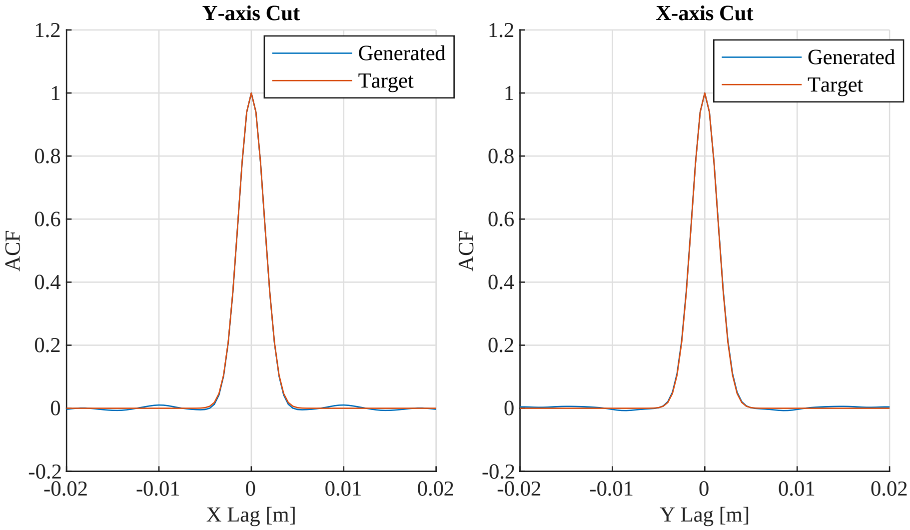

Figure 2.7: Comparison of the x and y cuts of the correlation function of a generated random surface to the x and y cuts of a target correlation function, which was specified as a gaussian correlation function.

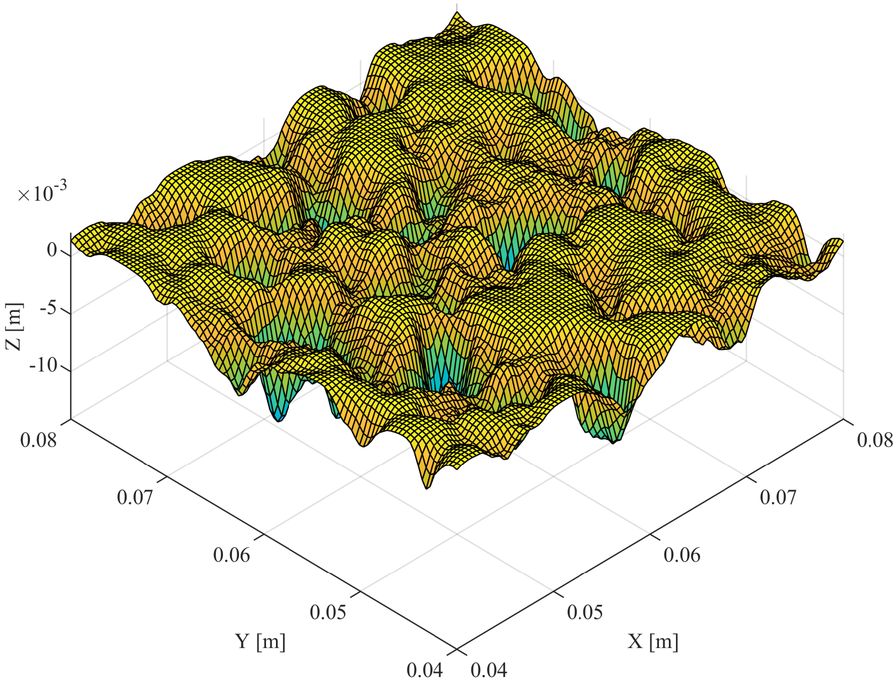

Figure 2.8: Synthetically generated model of an asphalt road surface.

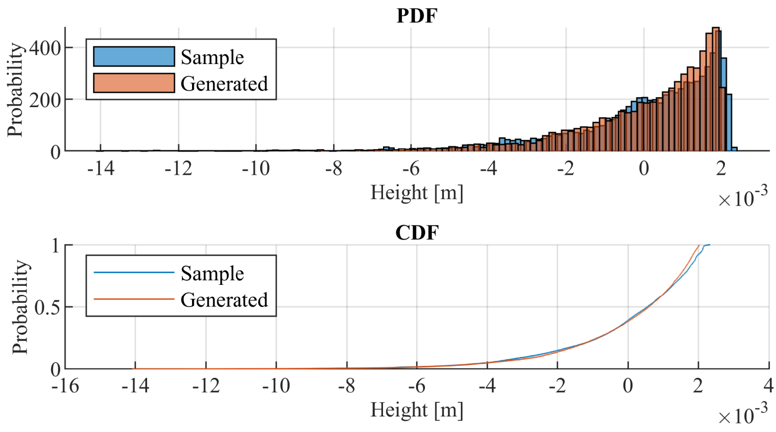

Figure 2.9: Comparison of the statistical distribution functions of the input and generated model.

the computed bi-static radar cross sections are not contaminated by forward scattering from these side lobes. The size of the array, in combination with the size of the road surface model chosen in such a way to reduce incident power on the surface model edges to suppress effects of edge diffraction on the NRCS results to simulate infinitely large media while keeping the computational requirements within realistic limits. The distance of the source to the model was selected such that far-field conditions were achieved while keeping the beam footprint small, again to reduce edge diffraction effects while keeping the computational requirements in check.

As scattering from a particular road surface model is influenced by its shape, multiple realisations for each parameter set were simulated to obtain statistical data on the NRCS for the considered parameter set. Fig. 2.10 shows a comparison of the mean far-field computed from simulations of 1, 10, 20, and 30 surface realisations. It can be seen that the results converge relatively quickly and that considering at least 10 realisations provide sufficiently converged results. Therefore, this amount of simulations provides a good trade-off between simulation results and quality of results.

2.3.3. Simulation Results

With the developed simulation procedure, the NRCS of surfaces with different surface characteristics can be studied. One of these parameters is the RMS height. This parameter determines the amplitude of the roughness variations around the mean surface. The results of variation in the RCS due to the RMS height of the surface are shown in Figs. 2.11 and 2.12. In Fig. 2.11, the RCS for horizontally polarised sensing waves is shown while Fig. 2.12 shows the results for vertically polarised sensing waves.

It can be seen that as the RMS height decreases, and thus the surface becomes flatter, the forward scattering increases while the backscattering decreases. Furthermore, the vertically polarised sensing wave shows a sharp decrease in forward scattered waves at an angle close to 60°, especially for the flatter surface. This dip is located at the Brewster's angle, at which

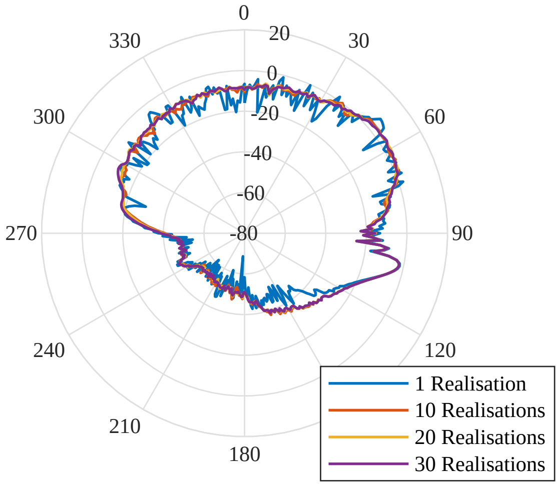

Figure 2.10: Comparison of averaged scattering results in dB using 1, 10, 20, and 30 surface realisations.

all incident power is transmitted into the dielectric medium and none is reflected. This transmitted radiation is subsequently absorbed by the asphalt, as it is a lossy dielectric.

2.3.4. Verification and Limitations

To verify the correctness of the simulation results, they were compared to results obtained by the small perturbation method (SPM) [11] for the same surface parameters. A comparison of RCS results from simulations and SPM for a surface with a RMS height of 0.2 mm and a correlation length of 0.4 mm is shown in Fig. 2.13. This figure shows that the simulation results are in good agreement with the results obtained by SPM. Similar comparisons were made for surfaces with that same correlation length, but RMS heights of 0.25 mm and 0.02 mm. These were also found to be in good agreement with each other.

Subsequently, to find the limits of the numerical approach, comparisons were made with SPM for surfaces with very large correlation lengths and thus with a small RMS slope of roughness. In these cases it was found that results of SPM and numerical results started to diverge as shown in Fig. 2.14. This is due to the fact that for this correlation length, the RCS becomes very small according to SPM. This leads to the numerical results becoming dominated by diffraction effects from the model edges, thus leading to inaccurate results.

From this investigation on model verification and its limitations, it could be seen that in the region of surface parameters where the backscattering is significant, the proposed numerical method provides accurate results that show good correspondence with results obtained by SPM. This also leads to a high degree of confidence in scattering results of rough surface with high RMS slope, such as real world asphalt, for which SPM does not provide valid results any more. Even though the proposed method shows good results for rough surfaces, it does diverge from SPM results for very smooth surfaces and should therefore be used with care when evaluating surfaces with low RMS slope.

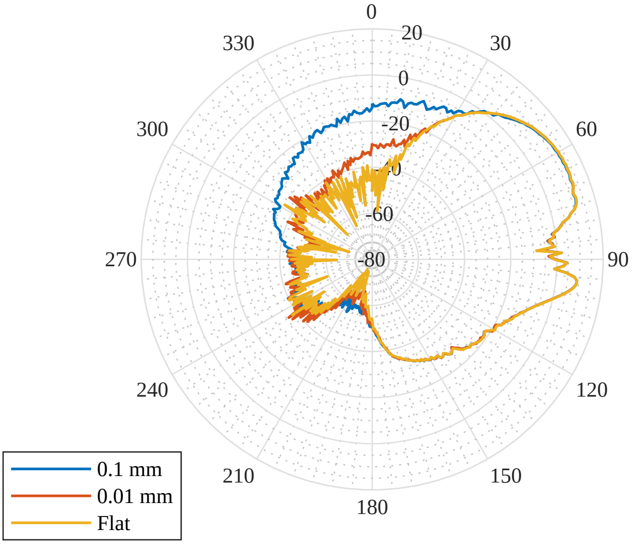

Figure 2.11: Comparison of scattering results as function RMS height of the surface for a horizontally polarised sensing wave, incident at 60°.

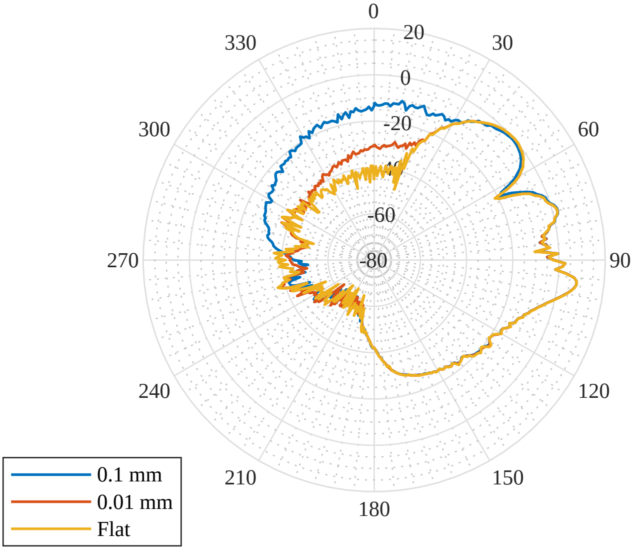

Figure 2.12: Comparison of scattering results as function RMS height of the surface for a vertically polarised sensing wave, incident at 60°.

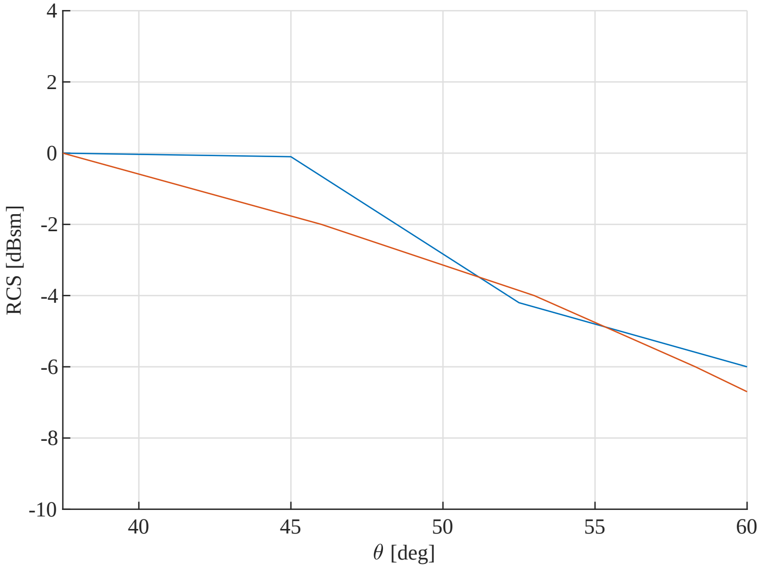

Figure 2.13: Comparison of normalised radar cross sections obtained with the proposed numerical method and the SPM for a surface with a RMS height of 0.2 mm and a correlation length of 0.4 mm as function of the angle of incidence θ.

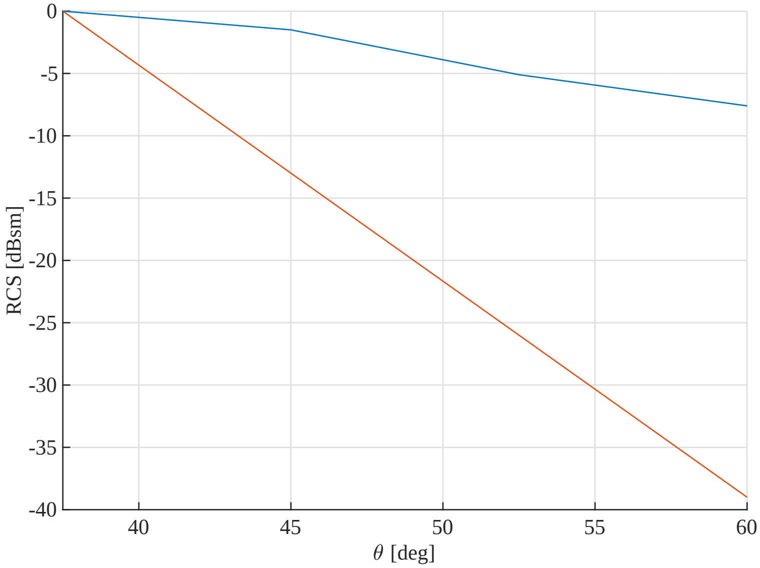

Figure 2.14: Comparison of of normalised radar cross sections obtained with the proposed numerical method and the SPM for a surface with a RMS height of 0.2 mm and a correlation length of 2 mm as function of the angle of incidence θ.

2.4. Road Surface Signatures in Automotive Scenarios

By using NRCS models of road surface scattering, the range-Doppler signatures as observed by automotive radar can be considered. In this section, a method to achieve this is presented.

2.4.1. Influence of Geometrical Effects on Road Surface Signatures

In the automotive radar scenario, there are two important factors that influence scattering from road surfaces that need to be considered. Firstly, the angle of incidence varies from range cell to range cell as well as with azimuth. Secondly, when the car is moving, a Doppler-shift will be induced depending on the radial velocity corresponding to the range-azimuth cell the radar is observing.

The first mentioned effect influences the amount of scattering that will happen within a range cell. To illustrate this, when the angle of incidence is close to the horizon, generally less radiation is scattered back from a rough surface than when the wave is incident from an angle close to the normal. The second mentioned effect will cause the signature of the road surface to spread along the Doppler axis of the range-Doppler map, i.e. a cell that is right in front of the car will have a higher radial velocity and thus a larger Doppler-shift than a cell orthogonal to the direction of travel.

In FMCW radar systems using multiple pulses per frame, the amount of range migration, variation in incident angle and Doppler-shift of a surface patch over the coherent processing interval must be considered. If this variation is significant, the observed scattering may be affected and more sophisticated electromagnetic techniques need to be developed to account for such variations. Equally, the variation of incident angle and Doppler-shift within one range cell must be considered. Lastly, the signature of the road surface is also influenced by the radiation pattern of the radar system. If the gain changes significantly from pulse to pulse within a range bin, this effect needs to be taken into account as well.

Here a method is presented to evaluate the severity of the mentioned effects for a specified road surface. First the definitions of geometrical parameters will be presented. Afterwards, the derivation of incident angle, radial velocity and local radar observation angle will be shown. The last mentioned quantity is required to calculate the radar antenna gain for that surface point.

Geometrical Parameter Definitions

The radar location is indicated by the vector $\vec{p_r} = \{0, 0, h_r\}$. Here, h_r indicates the height of the radar above ground level. The position of a point on the surface is indicated by the vector $\vec{p_s} = \{x_s, y_s, z_s\}$. Each surface point is also characterised by a normal vector, which is defined as $\hat{n_s} = \{x_{\hat{n}}, y_{\hat{n}}, z_{\hat{n}}\}$. The set of angles of incidence at a surface point are designated as θ_s and ϕ_s. Here, θ_s is the angle between the surface normal, representing the surface local z-axis, and the vector $\vec{r_{sr}}$, which is the vector pointing from the surface point to the radar. The surface local x-axis is defined in such a way that it lies on the global xz-plane. This surface local x-axis is used to compute the azimuth angle of the incident wave ϕ_s.

The radar local observation angles are defined by θ_r and ϕ_r. Here, the elevation θ_r

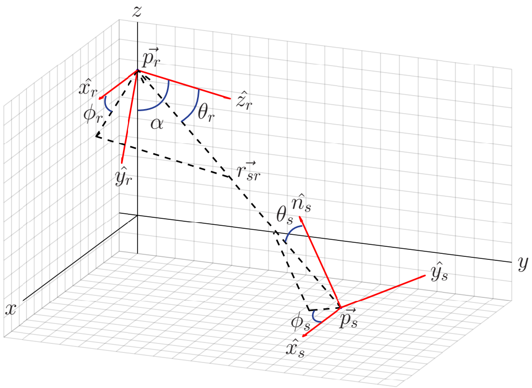

Figure 2.15: Geometrical parameters used for computing surface scattering.

is measured from the radar broadside direction, indicated by the z-axis in the radar local system. Likewise, ϕ_r is the azimuth measured from the x-axis in the radar local system. The angle between the radar local z-axis and the global x, y-plane is designated by the angle α.

Lastly, the velocity of the car is indicated by the vector $\hat{v_c} = \{0, v_c, 0\}$. Note from this vector that the car is travelling along the $\hat{y}$ direction. A summary of these geometrical parameters is shown in Fig. 2.15.

Derivation of Parameter Expressions

The angle θ_s can be found in a two-step process. The first step is to find the vector from the surface point to the radar location which can be calculated using $\vec{r_{sr}} = \vec{p_r} - \vec{p_s}$. Subsequently, using the relation between the dot product of two vectors and the angle between them, the surface local θ_s can be found using (2.7).

$$\theta_s = \cos^{-1}\left(\frac{\vec{r_{sr}} \cdot \hat{n_s}}{|\vec{r_{sr}}|}\right) \tag{2.7}$$

To find the surface local azimuth ϕ_s, first the surface local x-axis needs to be defined. As mentioned in section 2.4.1, this axis should lie within the global xz-plane. This combined with the fact that the surface local angle should be orthogonal to the surface normal vector, results in (2.8).

$$\hat{x_s} = \frac{\hat{y} \times \hat{n_s}}{|\hat{y} \times \hat{n_s}|} \tag{2.8}$$

The last remaining surface local axis, $\hat{y_s}$ can simply be found by computing $\hat{n_s} \times \hat{x_s}$.

The surface local azimuth can subsequently be found by transforming $\vec{r_{sr}}$ to the surface local system and then taking the arctangent of the x- and y-components, resulting in (2.9).

$$\phi_s = \tan^{-1}\left(\frac{\hat{y_s} \cdot \vec{r_{sr}}}{\hat{x_s} \cdot \vec{r_{sr}}}\right) \tag{2.9}$$

The radial velocity $\vec{v}_r$ can be found by computing the projection of the velocity of the car in the direction of $\vec{r}_{sr}$ as shown in (2.10).

$$v_r = \frac{\vec{r}_{sr} \cdot \vec{v}_c}{|\vec{r}_{sr}|} \tag{2.10}$$

As $\vec{r}_{sr}$ is the vector from the surface point to the radar, the radial velocity for objects moving towards the radar is negative, while the radial velocity for objects moving away is positive.

The radar local observation angles θ_r and ϕ_r can be found by first transforming $\vec{r}_{sr}$ to the radar local coordinate system and subsequently using a transformation to spherical coordinates. This transformation can be performed using (2.11).

$$\vec{r}_{sr,r} = \begin{bmatrix} 1 & 0 & 0 \\ 0 & \cos(\pi - \alpha) & -\sin(\pi - \alpha) \\ 0 & \sin(\pi - \alpha) & \cos(\pi - \alpha) \end{bmatrix} (\vec{p}_s - \vec{p}_r) \tag{2.11}$$

Transformation to spherical coordinates subsequently results in $\theta_r = \cos^{-1}\left(\frac{\vec{r}_{sr,r}}{|\vec{r}_{sr,r}|}\right)$ and $\phi_r = \tan^{-1}\left(\frac{\vec{r}_{sr,r} \cdot \hat{y}}{\vec{r}_{sr,r} \cdot \hat{x}}\right)$.

2.4.2. Application to Rough Surface without Undulations

Using the equations derived in section 2.4.1, the signature for a rough surface without undulations, i.e. a flat, straight surface, is computed. In this specific case, the surface z-coordinate for all surface points is 0 and the normal vector of this surface is equal to $\hat{z}$ everywhere. This also implies that the surface local system has the same orientation as the global system. Furthermore, it is assumed that the scattering from the road surface is isotropic, meaning that the radar cross-section (RCS) of a surface point is no longer a function of ϕ_s.

First, the θ_s^{flat} angle for the rough surface without undulations is derived. This is determined to be

$$\theta_s^{flat}(x, y) = \cos^{-1}\left(\frac{h_r}{\sqrt{x^2 + y^2 + h_r^2}}\right). \tag{2.12}$$

The radial velocity v_r^{flat} for this surface is found to be

$$v_r^{flat} = \frac{v_c y}{\sqrt{x^2 + y^2 + h_r^2}}. \tag{2.13}$$

The expressions for the local radar observation angles are a bit more intricate. The θ_r^{flat} angle can be computed using

$$\theta_r^{flat} = \cos^{-1}\left(\frac{y \sin(\pi - \alpha) - h_r \cos(\pi - \alpha)}{\sqrt{x^2 + y^2 + h_r^2}}\right). \tag{2.14}$$

Similarly, ϕ_r^{flat} can be calculated using

$$\phi_r^{flat} = \tan^{-1}\left(\frac{y \cos(\pi - \alpha) + h_r \sin(\pi - \alpha)}{x}\right). \tag{2.15}$$

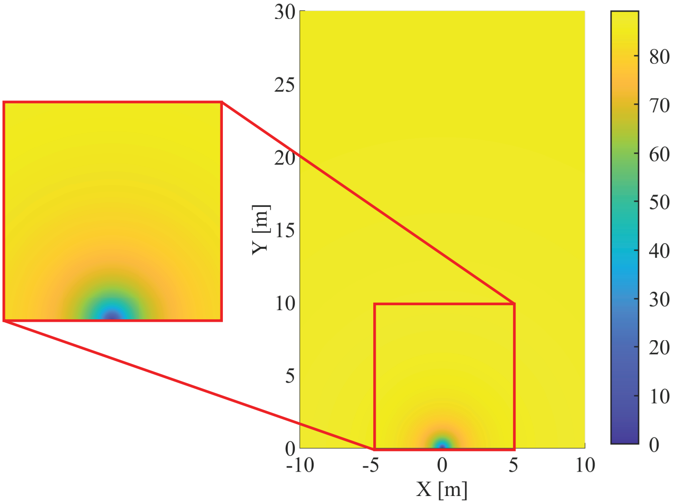

Figure 2.16: Angle of incidence θ_s^{flat} in degrees for a surface without undulations for a radar mounting height h_r of 50 cm.

Using the expressions derived above, the variation in radial velocity and incident angles over a rough surface without undulations can be studied. Fig. 2.16 shows θ_s^{flat} as function of x and y for such surface. From this picture, it can be seen that θ_s^{flat} varies strongly close to the car due to the mounting height of the radar, but this variation reduces quickly. When this angle is compared at 5 m and 6 m respectively, the difference between these ranges has dropped to below 1 degree. Depending on the scattering characteristics of the observed rough surface, the RCS of one range bin can be simulated by plane wave incidence.

Besides this, Fig. 2.16 can also be used to evaluate the change in incident angle over the coherent processing interval of the radar system. Assuming a coherent processing interval of 1 ms, an observed surface point will experience a range migration of 42 mm when the car is moving with a velocity of 150 km/h. This shows that the change in angle of incidence, and by extension the scattering characteristics, will not vary significantly over the coherent processing interval.

Fig. 2.17 shows the radial velocity of each point on the surface without undulations. Here it can be seen that the radial velocity over the surface does not vary significantly directly in front of the vehicle, but shows stronger variation directly to the left and the right of the car. This causes the road surface to have different radial velocities smearing its signature in a range bin over the Doppler domain. The severity of this effect depends on the cross-range resolution of the radar system and on the velocity of the car.

2.4.3. Range-Doppler Signature of a Flat Asphalt Surface

Using the results obtained from sections 2.4.1 and 2.4.2 plus information on the radiation pattern of the radar and the RCS σ_s of a surface patch, the range-Doppler signature can be derived. Regarding the radiation pattern of the radar, in this example a simple $\cos\left(\theta_r^{flat}\right)$ pattern is assumed.

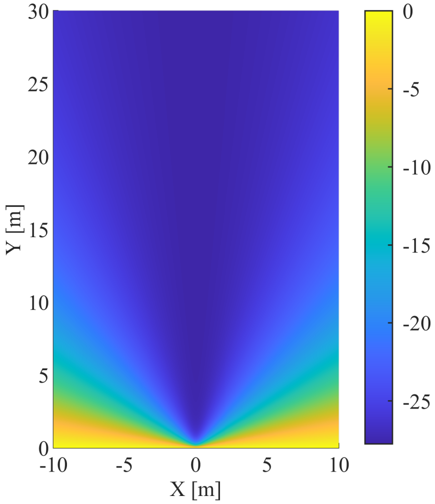

Figure 2.17: Radial velocity v_r^{flat} for a surface without undulations with a radar mounting height h_r of 50 cm and a platform velocity v_c of 100 km/h.

Numerical simulations to determine the statistics on the RCS of asphalt road surfaces is currently ongoing and expected to provide results in coming weeks. In order to already obtain a range-Doppler signature, the RCS of an asphalt surface patch in this example is assumed to be independent of angle of incidence and frequency. Hence, the RCS of each surface patch in this scenario is the same. To generate the range-Doppler map, the received power for each surface patch is calculated and then summed to the corresponding range-Doppler bin. This received power is calculated using the radar equation. This results in the range-Doppler map shown in Fig. 2.18 (left). This figure clearly shows the spreading of the road surface signature over the Doppler domain. Furthermore, it can be seen that the radar radiation pattern reduces the power received from cells that present low Doppler-shifts as these cells are orthogonal to the direction of travel of the car. Lastly, it can be seen that most of the backscattered signal is concentrated in close range bins due to the fourth power range dependence, and that more power is received from patches with high Doppler-shift compared to those with low Doppler-shift.

Besides this, Fig. 2.18 (right) shows also a range-Doppler map of an automotive radar measurement performed whilst driving at about 15 km/h on a public road. Here, the road surface signature can clearly be recognised, matching in shape with the proposed model. The measured range-Doppler map also contains another extended target at further range which corresponds to a building on the side of the road. In this measurement, the radar was mounted on the front bumper of a car at a height of approximately 40 cm and with an angle α of 90 degrees. The radiation pattern of the radar in this measurement can be approximated by a $\cos\theta$ shape.

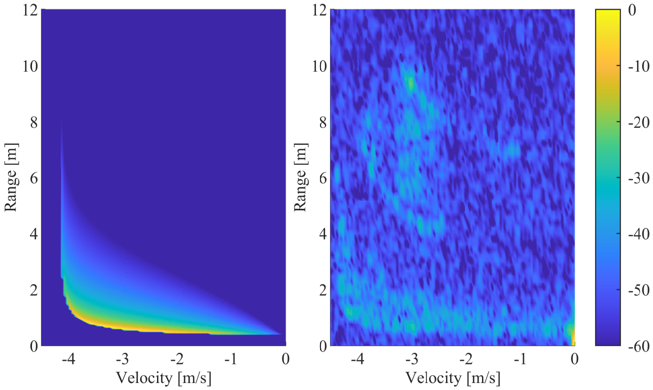

Figure 2.18: Comparison of predicted (left) and measured (right) normalised range-Doppler signatures in decibels of an asphalt road surface when the car is moving at a speed v_c of 15 km/h.

2.5. Conclusions

In this chapter, numerical investigations of road surface radar cross sections and road surface signatures were presented. To perform numerical simulations on radar cross sections of road surfaces, first the material parameters, i.e., permittivity and conductivity, of asphalt and other road surfaces were determined. This was done by means of transmission measurements through road surface samples using a measurement setup based on a vector network analyser. Subsequently, a method to determine the real part of the permittivity of the sample-under-test based on the extra propagation delay induced by the sample was presented. It was found that this method provides accurate estimates of the permittivity as good agreement was achieved between the measured permittivity of an PTFE reference sample and corresponding permittivity values from literature. Thereafter, a procedure to determine the conductivity of for lossy materials based on the attenuation of the sensing wave was described. This method uses a three-interaction scattering model which relates the conductivity of the material-under-test to the attenuation induced by the measured material sample. By solving this three-interaction model numerically, the conductivity corresponding to the surface-under-test could be determined successfully. The results were subsequently validated using full-wave simulations, showing good agreement between measured and simulated values. In the end, it was found that the real part of the relative permittivity of the considered asphalt samples is about 4 while the conductivity is measured to be 0.767 S/m.

Subsequently, a numerical method based on MoM/MLFMM to evaluate the radar cross sections of road surface samples was presented. The first step in the simulation procedure is synthesising accurate models of road surfaces. This is achieved using a surface generation procedure based on spatial spectral filtering and probability transforms. It was shown that this surface synthesis procedure is able to synthesise realisations of surfaces with arbitrary size, surface height cumulative distribution functions, and surface correlation functions.

Subsequently, scattering from the generated surface realisations using the MoM/MLFMM solver in the commercially available FEKO software package were performed. Using the developed simulation procedure, radar cross sections as function of surface RMS height and incident angle of the incoming radiation have been evaluated. The obtained results were verified by comparing these with results found using the small perturbation method. It was found that for surfaces where edge diffraction effects were negligible compared to surface backscattering, good correspondence between SPM and full-wave numerical results was obtained. This is true for surfaces with relatively high RMS slopes, such as real world asphalt road surfaces, thus providing confidence in obtained scattering results for this type of surface for which the surface parameters are outside the region of validity of the SPM.

Furthermore, this chapter has presented a method to compute the dynamic signature of road surfaces in automotive scenarios. This has been applied to a flat asphalt rough surface taken from a realistic road sample. For the first time in literature, road surface scattering has been analysed as a dynamic process and presented in the form of a range-Doppler plot. This result has been compared to an automotive radar measurement performed whilst driving on a public road and good agreement between model and measurement has been demonstrated.

Besides this, it has been concluded that over a coherent processing interval the Doppler-shift does not change significantly for an observed range cell. Similarly, the change in incident angle over a range cell has been shown to be small. However, depending on the scattering characteristics of the surface, this may be significant and needs to be taken into account for computation of backscattering from the road.

3

Polarimetric NRCS Road Surface Models and its Applications in Automotive Radar

Another way to obtain data on scattering from rough surfaces in automotive scenarios is by performing experimental measurements, which are complementary to data obtained by simulations as described in chapter 2. This chapter presents methods on how to perform these measurements and how to use the experimental measurements results to extract scattering models of rough surface materials. Besides this, also some applications of the found scattering models are presented.

Parts of this chapter have been published as:

W. Bouwmeester, F. Fioranelli, and A. Yarovoy, "Statistical Modeling of Polarimetric RCS of Road Surfaces for Scattering Simulation and Optimal Antenna Polarization Determination", *IEEE Journal of Selected Topics in Applied Earth Observations and Remote Sensing*, 2024.

W. Bouwmeester, F. Fioranelli, and A. Yarovoy, "Statistical Polarimetric RCS Model of an Asphalt Road Surface for mm-Wave Automotive Radar", in *2023 20th European Radar Conference (EuRAD)*, Berlin, Germany, 2023.

3.1. Introduction

The amount of vehicles that are equipped with advanced automotive radar systems operating in the 77 GHz band to enhance road safety is rising quickly [12], [13]. These radar systems are mainly used to detect, track, and often to also classify, other road users and obstacles that may be present around the car. Being more compact than their 24 GHz predecessors, modern mm-wave radar systems that operate at 77 GHz receive more intense backscattering from the road surface in front of the vehicle compared to 24 GHz radar systems due to the increased reflectivity of these surfaces at 77 GHz.

Due to the increased backscattering, scattering from road surfaces influences radar measurements more significantly and therefore it is important to formulate accurate radar cross section (RCS) models to properly evaluate the impact of road surface scattering in various automotive radar applications. One of the topics for which polarimetric models of road surfaces are of interest, is the recent research in the field of polarimetric automotive radar, a few examples of which can be found in [14–17]. In [16] and [17], specifically the benefits of polarimetric radar for road surface classification are studied. In [16], this is done by computing two features, namely target entropy and polarimetric pedestal. As these are statistical quantities, accurate statistical polarimetric models of the RCS of road surfaces could be used to validate this method further. In [17], road surface classification on measurement data from polarimetric radar is performed using a convolutional neural network. For this application, a statistical polarimetric model could be used to synthesise lots of surface scattering data on which these networks could be trained.

Statistical RCS models of surface clutter could also be used to increase the accuracy of automotive radar simulation at mm-wave frequencies. For example, in [18] and [19], methods of simulating automotive radar based on ray-tracing are proposed but road surface clutter is not considered. In [18], clutter caused by a grass surface is taken into account by placing low polygon count grass chunks randomly on a lawn and applying ray-tracing to simulate the response. Synthesis of surface clutter based on statistical RCS models could potentially provide surface clutter returns to simulation results without the need to define complex geometries for surfaces and without the need for ray-tracing, potentially decreasing the required computational resources. An approach similar to this is shown to be effective in [20], where scattering matrices from snow slabs are generated based on statistical data previously obtained by method of moments and finite element method based electromagnetic solvers. Polarimetric statistical RCS models of surfaces could also be of use outside the field of automotive radar and could, for example, be applied to simulate backscattering in synthetic aperture radar. As an example, in [21] the reflectivity is calculated using the small perturbation method and geometrical optics, but realisations of reflectivity could also be generated using statistical RCS models. Also, in ground penetrating radar, normalised RCS models of surface scattering are needed to provide estimations of surface clutter, as described in [22]. Another general class of applications where normalised RCS models are of use, is the determination of optimal polarisation of the electromagnetic sensing wave used in radar systems, a few examples of this can be found in [23] and [24].

Even though the applications for normalised RCS models of road surfaces are many, only scarce experimental results on road surface scattering at mm-wave frequencies are presented [4, 7, 25], and research on statistical models of road surface scattering at mm-wave frequencies is relatively limited. In [7], vertically polarised measurements were performed on road surfaces under various conditions. It was found that for vertically polarised waves, wet road surface decreases road surface backscattering while slushy conditions increase it, and that snow results in a bimodal distribution for backscattering. In [4], a polarimetric road surface scattering model is developed based on vector radiative transfer theory while statistical properties of road surface scattering, such as correlation of scattering parameters, are not discussed. Similarly, in [26], a theoretical model for road surface scattering in icy conditions is presented but statistical properties of such scattering are not considered. More measurements of radar backscattering at mm-wave frequencies from road surfaces are presented in [25], where it is also found that surface scattering strongly depends on the type of surface, while statistical data on road surface scattering are unavailable. Furthermore, some data on road surface measurements are presented in [27] and [28], which also show dependence on road surface conditions at frequencies above and below 77 GHz respectively, but no statistical analysis is presented.

To address this gap, a novel method to determine the statistical properties of surface scattering from radar measurement data based on the preliminary results in [29] is proposed in this chapter. The method determines a statistical model of the normalised RCS of a surface-under-test, which is corrected for the influences of the radiation pattern of the measurement antenna and the non-uniform propagation distance from the measurement antenna to different points on the surface. This method is then applied to measurements of real road surfaces under various conditions, and the results of this procedure are presented.

Subsequently, two novel applications of the derived statistical models of normalised RCS of surfaces are introduced in this work. Firstly, a new method is developed to synthesise/simulate road surface scattering based on the extracted models. The results from this simulation can then be used to generate range profiles, range-angle profiles, and range-Doppler spectra for subsequent processing. Excellent agreement between measured range profiles and simulated range profiles is demonstrated. Secondly, a novel method for determining the optimal sensing wave polarisation for single-polarised radar systems is proposed, in order to maximise or minimise backscattering from the road surface. This new method is based on a factorisation of the polarisation vector and combined with a Monte-Carlo approach to use the statistical models found for the measured road surfaces. Alternatively, this approach can also be used to, amongst others, design polarimetric filters to enhance contrast between various surface types.

The rest of the chapter is structured as follows: Section 3.2 presents the RCS model and the procedure to determine the statistical properties of the normalised RCS of a surface-under-test based on measurement data. Section 3.3 describes how to utilise the statistical RCS models to simulate surface scattering and section 3.4 details a way to find the optimal polarisation for minimising and maximising returns from surface scattering for single-polarised radar. Section 3.5 explains the used measurement setup and procedure to measure road surface conditions while in section 3.6, the methods described in the previous sections are applied to the measurement data from real road surfaces. Finally, this chapter concludes with section 3.7.

3.2. Normalised Radar Cross Section Modelling

The first step in modelling the normalised scattering parameters of a surface-under-test (SUT) is to develop a model to compute the range profile as measured by radar systems.

To this end, a surface is modelled as a grid of uncorrelated discrete scatterers. The distance, observation angles, and incidence angles relative to each scattering elements can be computed using the equations outlined in [30]. Using the radar equation in (3.1), the ratio of returned power (P_x^{rx}) and transmitted power (P_y^{tx}) can be found for an individual scattering element. In (3.1), G_x^{rx} and G_y^{tx} are the antenna gains of the transmitting and receiving antennas, respectively, λ is the wavelength, A is the surface area of the scattering element and σ_{xy}^0 is its normalised RCS. Lastly, r represents the distance from the antenna to the surface scattering element. The x and y subscripts indicate the polarisation basis. For example, in this chapter a horizontal/vertical polarisation basis is used, thus x and y can be either H or V. Furthermore, it should be noted that the gains, surface area, normalised RCS and range are dependent on the location of the scattering element.

$$\frac{P_x^{rx}}{P_y^{tx}} = \frac{G_x^{rx} G_y^{tx} \lambda^2 A \sigma_{xy}^0}{\left(4\pi\right)^3 r^4} = R_{xy} \sigma_{xy}^0 \tag{3.1}$$

Since the normalised scattering parameters are related to normalised RCS as

$$\sigma_{xy}^0 = \left|S_{xy}^0\right|^2, \tag{3.2}$$

it can be seen that in conjunction with (3.1), the normalised scattering parameters can be determined from the measured complex-valued S-parameters S_{xy} as shown in (3.3).

$$S_{xy} = \frac{E_x^{rx}}{E_y^{rx}} = \sqrt{R_{xy}} S_{xy}^0 \tag{3.3}$$

This is possible as the returned power is related to half of the square of the magnitude of the returned electric field strength.

To compute the measured total scattering parameters as function of range, i.e. a range profile, the scattering parameters of the N scattering elements within a range bin ρ are summed together, with each element indexed by i as shown in (3.4):

$$S_{xy}^{tot}\left(\rho\right) = \sum_{i=1}^{N} \sqrt{R_{xy,i}} S_{xy,i}^0. \tag{3.4}$$

Note that when the scattering from all elements is uncorrelated, i.e. S_{xy}^0 has a random phase, $\left|S_{xy}^{tot}\right|^2$ and P_x^{rx}/P_y^{tx} converge towards the same value and thus power is conserved.

Using the model of measured range profiles, the statistical properties of the random variable S_{xy}^0 can be extracted. To do this, a few assumptions are made, namely:

- The normalised scattering parameters of the surface-under-test are isotropic, i.e. do not depend on azimuth of incident and reflected radiation.
- All scattering elements of the surface-under-test within a range bin experience the same angle of incidence.

These assumptions ensure that within a range bin the equality $S_{xy,i}^0 = S_{xy}^0$ holds.

As the first step, the extraction of $\langle S^0_{xy}\rangle$ from $\langle S^{tot}_{xy}\rangle$ is considered, where the angular brackets indicate the mean value of the statistical ensemble of scatterers. As

$$\begin{aligned}\langle S^{tot}_{xy}\left(\rho\right)\rangle &= \langle\sum_{i=1}^{N}\sqrt{R_{xy,i}}S^0_{xy}\rangle\\ &= \left(\sum_{i=1}^{N}\sqrt{R_{xy,i}}\right)\langle S^0_{xy}\rangle,\end{aligned} \tag{3.5}$$

the mean value of S^0_{xy} can be found using (3.6):

$$\langle S^0_{xy}\left(\rho\right)\rangle = \frac{1}{\sum_{i=1}^{N}\sqrt{R_{xy,i}}}\langle S^{tot}_{xy}\left(\rho\right)\rangle. \tag{3.6}$$

As each surface scattering element has a co- and cross-polar normalised scattering parameters for each of the two polarimetric channels which are not necessarily uncorrelated, the covariance of the normalised scattering parameters must also be found from the four measured range profiles. The covariance of S^0_{xy} and S^0_{uv} is related to the covariance of S_{xy} and S_{uv} via (3.7). Here, u & v are also indicators of the same polarisation basis as x & y but can differ from each other, to express all possible covariance permutations. In the equations, $Cov\left(A,B\right)$ is abbreviated to $C\left(A,B\right)$.

$$\begin{aligned}C\left(S^{tot}_{xy},S^{tot}_{uv}\right) &= C\left(\sum_{i=1}^{N}\sqrt{R_{xy,i}}S^0_{xy},\sum_{j=1}^{N}\sqrt{R_{uv,j}}S^0_{uv}\right)\\ &= \left(\sum_{i,j}\sqrt{R_{uv,i}}\sqrt{R_{xy,j}}\right)C\left(S^0_{xy},S^0_{uv}\right)\end{aligned} \tag{3.7}$$

In (3.7), the sum over i and j represents all combinations of i and j. However, since the covariance of the normalised scattering parameters of scattering elements i and j is 0 since the scattering elements are uncorrelated, the covariance is found as:

$$C\left(S^{tot}_{xy},S^{tot}_{uv}\right) = \left(\sum_{i=1}^{N}\sqrt{R_{uv,i}}\sqrt{R_{xy,i}}\right)C\left(S^0_{xy},S^0_{uv}\right). \tag{3.8}$$

Therefore, the covariance of S^0_{xy} and S^0_{uv} can be found as:

$$C\left(S^0_{xy},S^0_{uv}\right) = \frac{C\left(S^{tot}_{xy},S^{tot}_{uv}\right)}{\sum_{i=1}^{N}\sqrt{R_{uv,i}}\sqrt{R_{xy,i}}}. \tag{3.9}$$

3.3. Surface Clutter Synthesis

Once models of the normalised scattering parameters of surfaces are known, they can be used to synthesize/simulate range profiles, range-angle profiles, and range-Doppler spectra of surface clutter. Similar to the previous section, the proposed synthesis method models the surface as many individual scattering elements and computes the contribution of each individual scattering element towards the signal as measured by a radar. The synthesis method comprises the following steps:

1. Model the surface as a collection of discrete surface scattering elements by generating a grid of these elements.
2. Find the incident angles, range, and observation angles for each surface scattering element.
3. For each scattering element, take a sample from a multivariate distribution with mean and covariance corresponding to the angle of incidence for said surface scattering element.
4. Calculate the received electric field strength from each scattering element.
5. Sum the received electric field strength from each scattering element to its corresponding bin.

In step 2, the range to each surface scattering element can be computed by taking the norm of the vector pointing from the antenna to said scattering element. The incident and observation angles can in turn be computed using the equations presented in [30]. Subsequently, the contribution of each scattering element can be found using:

$$E_x^{rx} = \sqrt{R_{xy} S_{xy}^0} E_y^{tx}, \tag{3.10}$$

where R_{xy} is a function of the previously computed range to and observation angles of the surface scattering element. An example of the output of this synthesis process for the co-polarised channels is displayed in a later section in Fig. 3.8.

Subsequently, this output can be further processed to compute range profiles, range-angle plots and range-Doppler spectra. This can be done by specifying the limits and resolution of the to be simulated profiles and summing the contribution of each scattering element to its corresponding range, angle, and/or Doppler bin. To compute the azimuth angle of a scattering element in the case of 3D radar (i.e., a radar that provides range, azimuth, and Doppler information), or both azimuth and elevation angles in the case of 4D radar (i.e., a radar that also provides elevation information), the theory in [30] can be used. To compute the Doppler or velocity bin, the radial velocity v_r of each scattering element with coordinates x and y can be found as:

$$v_r = \frac{v}{\sqrt{x^2 + y^2 + h_r^2}}, \tag{3.11}$$

where h_r is the antenna mounting height and v is the platform velocity which is assumed to be along the y-axis.

Finally, to create range and range-angle profiles and range-Doppler spectra, the contributions of the scattering elements to the electric field can be summed in the correct bins via:

$$F = \sum_{k=1}^{M} E_{xy,k}^{rx}. \tag{3.12}$$

Here, F is the desired output representation (e.g., range-Doppler spectrum) and k represents the index of a scattering element for the M surface scattering elements that lie within a certain range, angle, and/or Doppler bin. Thus, F can be a function of range, angle, and Doppler, or all of them or even other bin quantities by which the F could be binned. In $E^{rx}_{xy,k}$, the subscript x and y indicate the receive and transmit polarisation respectively. Note that when $E^{rx}_{xy,k}$ are zero mean random variables, performing this summing operation will not cause the received field from a range-bin to converge to zero when the number of scattering elements within such a range-bin increases. This is because the area term in $R_{xy,i}$ is inversely proportional to the number of scattering elements within one range-bin, which results in $E^{rx}_{xy,k}$ decreasing with the square root of the number of scattering elements, as can be seen from (3.12). This in turn leads to the variance of the electric field received in a range-bin remaining the same as the variance of a sum of identical independent distributed random variables is proportional to the number of variables in that sum while the variance of a random variable pre-multiplied by a constant is the same as the variance of the same random variable post-multiplied by that constant squared. An example output of range profile and range-Doppler spectra can in a later section be seen in Figs. 3.9 and 3.10 respectively.

3.4. Optimal Sensing Wave Polarisation for Single-Polarised Automotive Radar

Besides surface clutter synthesis, the polarimetric normalised RCS models can also be used to find the optimal polarisation to maximise or minimise the power that is received from a target corresponding to that model by a radar system that uses a single polarisation. Furthermore, this analysis could also be used to for example design a filter that maximises the contrast between multiple classes of targets, e.g. a puddle of water on asphalt versus dry asphalt.

Using the polarisation vector of an antenna, indicated by $\vec{p}$, which in a single-polarised radar system is the same for the transmit and receive antennas, the received power P^{rx} from a target with scattering matrix S can be computed using (3.13), in which ^{H} indicates the conjugate transpose operator. The polarisation vector is the vector that describes the polarisation state of a transmitted electromagnetic wave by an antenna and the gain of that same antenna for incoming electromagnetic waves of a certain polarisation [31]. Using the polarisation vector and the scattering matrix, the received power from a target can be calculated as [32]:

$$P^{rx} = \left|\vec{p}^H S \vec{p}\right|. \tag{3.13}$$

As can be seen from this equation, the received power can be either minimised or maximised by selecting a certain $\vec{p}$.

The polarisation vector $\vec{p}$ is defined as follows:

$$\vec{p} = \begin{bmatrix} c_x e^{j\delta_x} \\ c_y e^{j\delta_y} \end{bmatrix} \tag{3.14}$$

Here, c_x and c_y describe the gain for the x and y polarised components while δ_x and δ_y describe the phases of those components. As in this problem the goal is to find the optimum polarisation for a single-polarised radar system instead of just maximising the antenna gain or simply setting it to zero to achieve zero received power, the polarisation vector is constrained to have a norm of 1, i.e. $\vec{p}^H\vec{p} = 1$. Polarisation vectors that have this property are denoted by $\hat{p}$.

Subsequently, since $\hat{p}^H\hat{p} = 1$, $\hat{p}$ can be factorised as follows:

$$\begin{aligned}\hat{p} &= \begin{bmatrix} Ae^{j\delta_x} \\ \sqrt{1-A^2}\, e^{j\delta_y} \end{bmatrix} = e^{j\delta_x} \begin{bmatrix} A \\ \sqrt{1-A^2}\, e^{j(\delta_y-\delta_x)} \end{bmatrix} \\ &= e^{j\delta_x} \begin{bmatrix} A \\ \sqrt{1-A^2}\, e^{j\delta} \end{bmatrix}\end{aligned}. \tag{3.15}$$

The absolute phase component in the polarisation vector, $e^{j\delta_x}$, can be neglected as it does not influence the received power as it results in an extra $\left|e^{j\delta_x}\right|$ term in (3.13) which is always equal to 1. Thus, it can be seen from (3.15) that $\hat{p}$ can be factorised by two parameters, namely A and δ. Furthermore, A is bounded between 0 and 1 since $\hat{p}^H\hat{p} = 1$ and δ is bounded between -180° and +180° due to the cyclic nature of the phase. Therefore, the minima and maxima of P^{rx} for a discrete target with a well known scattering matrix can be determined by numerically computing (3.13) for an array of values of A and δ bounded by 0 and 1 and -180° and +180° respectively.

Furthermore, in the case of a statistical description of S, the minima and maxima of P^{rx} can be found by means of a Monte-Carlo procedure. Namely, a large amount of scattering matrices can be generated using the procedure outlined in section 3.3. Thereafter, for each scattering matrix, P^{rx} can be calculated as a function of A and δ. Finally, the mean of P^{rx} over the different realisations of S can be taken, from which the maxima and minima can be determined. An example of such a computation is shown in a later section in Fig. 3.16.

3.5. Measurements

The measurement setup comprised a Vector Network Analyser (VNA) connected to a dual polarised horn antenna to perform polarimetric measurements. The antenna assembly was subsequently placed on a supporting structure that allowed for controlling the angle in the vertical plane of the antenna relative to the surface. This antenna orientation angle is defined as the angle between surface normal and the antenna broadside. The VNA was set to sweep a frequency range from 75 to 85 GHz in 1001 frequency steps. More details on the measurement setup and its settings can be found in [2].

Measurements were performed to obtain data for three different road surface conditions, as well as two different types of asphalt. The two considered types of asphalt were relatively new asphalt, and old asphalt which was scheduled to be replaced shortly after the measurements. As there exist many different types of asphalt, to keep the study presented in this work as comprehensive as practically possible, these two opposing ends of the range of possible asphalt types were selected to investigate the variation of backscattering from asphalt. The considered road surface conditions were the new asphalt type when dry, wet, and covered with basalt gravel as may be encountered during road surface construction or maintenance. In this case, the gravel comprised of basalt rocks ranging in size between 2 and 8 mm. Pictures of the road surface classes are shown in Fig. 3.1. These four road surface conditions were each measured with antenna orientation angles of 60°, to achieve maximum SNR at short range, and at 90°, to simulate forward looking radar.

To find a statistical normalised RCS model of the surfaces-under-test, it is important to obtain measurements of surface areas that are uncorrelated with each other. This can be done by ensuring that the antenna beam footprint illuminates a part of the asphalt surface that is at

(a) (b)

(c) (d)

Figure 3.1: Photographs of the three road surface conditions that were measured: (a) Dry asphalt; (b) Wet asphalt; (c) Asphalt covered with basalt gravel with pebble sizes between 2 and 8 mm. Additionally, a different patch of old asphalt was also measured (d).

least a few correlation lengths away. Previous investigation has shown that the correlation length of asphalt road surface is around 2 mm [30]. Therefore, this condition can be achieved by moving the measurement setup a few centimetres between measurements.

To gather sufficient data to compute proper statistics, after calibrating the measurement setup, 50 independent measurements of each surface class were obtained. Subsequently, the measurements were post-processed to find the total scattering parameters. More details on the calibration of the measurement setup, measurement procedure, and post-processing can be found in [29] and [2].

3.6. Experimental Results and Discussion

In this section, normalised radar cross section models of the four different road surface classes are determined by applying the procedure described in section 3.2 on the data set of VNA measurements collected as shown in section 3.5. The models of the several surfaces are presented in 3.6.1 and 3.6.2 while the application of these models to simulation of road surface scattering and determination of optimal polarisation for single-polarised radar

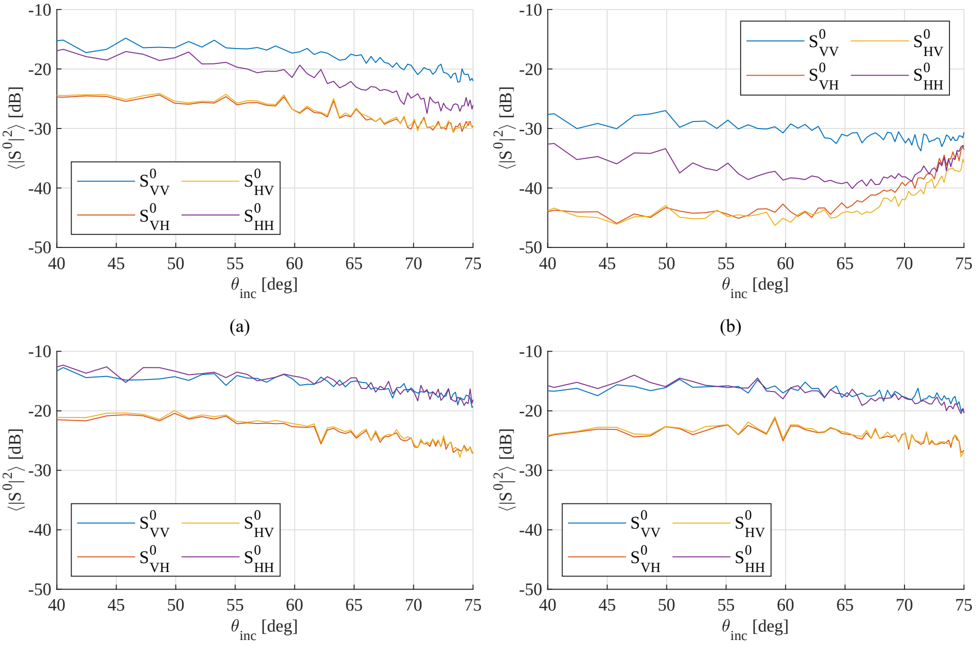

(a) (b) (c) (d)

Figure 3.2: Normalised radar cross sections of multiple different road surfaces and conditions. (a) Dry asphalt. (b) Wet asphalt. (c) Asphalt covered by basalt split ranging in size from 2 to 8 mm. (d) Old asphalt.

systems are presented in sections 3.6.3 and 3.6.4.

3.6.1. Normalised RCS of Various Isotropic Road Surface Conditions

The extracted normalised RCS models of the four measured road surface conditions are shown in Figs. 3.2a-3.2d. These respectively show the extracted normalised RCS models of dry asphalt, asphalt covered with water, asphalt covered with basalt split with sizes ranging from 2 to 8 mm, and old asphalt.

Fig. 3.2a shows that for dry asphalt, the two co-polar normalised RCSs start to differ more and more as the angle of incidence increases. At an incident angle of 40°, the horizontal and vertical normalised RCS are close to -16 dB for both co-polar channels, whereas at 75° the VV-polarised normalised RCS has decreased to -22 dB and the HH-polarised RCS to -26 dB. This scattering behaviour agrees well with known results of backscattering from natural surfaces [9]. Furthermore, it can be seen that both cross-polar normalised RCSs are of the same level due to the monostatic measurement configuration. Also, the cross-polar RCSs are significantly smaller than the co-polar ones, which indicates that a limited amount of multiple scattering events are occurring at the asphalt surface and within the asphalt medium, or that internal multiple scattering is attenuated strongly by the conductivity of the material.

The wet asphalt shows a smaller RCS for both co- and cross-polarised channels compared to dry asphalt (Fig. 3.2b). This is likely due to water - which permittivity is close to that of asphalt at 77 GHz - filling the cracks and holes in asphalt, increasing the effective flatness of the surface. This is further magnified by the relatively large imaginary part of the complex dielectric constant due to the relatively high conductivity of water. This results in higher reflection coefficients for both polarisations compared to dry asphalt, thus reducing the amount of power scattered back to the radar. It can also be seen that for the wet asphalt, the difference between the HH- and VV-polarised channels is larger than for dry and basalt-covered asphalt. This can also likely be contributed to the water layer increasing the effective surface flatness, whereas the rougher surfaces of the dry and basalt-covered asphalt depolarise the backscattered waves more significantly. Also, it can be seen that the cross-polar normalised RCSs are similar to each other, as expected for reciprocal media when measured in a mono-static configuration. Furthermore, it can also be observed that the co-polar normalised RCSs are significantly smaller than the co-polar RCSs, again indicating that the contribution from multiple scattering events is limited.

Note that for the measurements of wet asphalt, the normalised RCSs of the cross-polar channels and the HH-polarised channel start to increase from about 65° and 70° respectively. This is likely the result of the noise floor of the VNA, which is located around -110 dB when transformed to the time/range-domain. From the 65°/70° point onward, the return from the wet asphalt surface in these three channels is lower than the noise floor, and thus the measured S-parameters are dominated by noise power from the range corresponding to these incident angles onward. As the noise floor is constant, the measured S-parameters for all of the surface beyond these ranges is around -110 dB, independent of the actual range to the surface at those distances. Since the measured S-parameters are divided by the antenna footprint to compensate for differences in antenna gain and propagation losses as shown in (3.9), the normalised RCS shows an increasing trend for the surface area that is dominated by the constant noise floor. Thus, it can also be concluded that the lower limit of the measurable normalised RCS of a surface with this measurement setup as function of range can be found by compensating the noise floor value of the VNA for the antenna footprint using (3.9). As the normalised RCS of the wet surface for the cross-polar and HH-polarised channels is below this lower limit, an apparent increasing normalised RCS with incident angle results, due to the dominant contribution of noise at these ranges.

Furthermore, it can be seen in Fig. 3.2c that the normalised co-polarised RCSs of the basalt-covered asphalt are independent of polarisation. In this figure, the co-polarised RCSs follow the shape of a cosine closely, which is indicative of scattering by an electromagnetically rough surface with Lambertian behaviour. Also here, the cross-polar normalised RCSs are about 10 dB below the co-polar normalised RCSs, again indicating limited contribution from multiple scattering, and these are of about equal magnitude.

Lastly, it can be seen that the old asphalt surface type exhibits a scattering behaviour in between that of dry new asphalt and new asphalt covered by basalt gravel. It can be seen in Fig. 3.2d that the co-polar normalised RCSs are of similar magnitude compared to each other, thus indicating relatively strong depolarisation as also occurs for basalt-covered asphalt. However, it can also be seen that the magnitudes of the co-polar normalised RCSs of the old asphalt type are lower compared to those of basalt-covered asphalt. This is consistent with the geometrical roughness of the road surfaces, as the measured old asphalt is rougher than the new asphalt type while being smoother than the basalt-covered asphalt. This leads to the observation that the normalised RCSs of road surfaces are more strongly dependent on surface roughness characteristics rather than on their dielectric properties. Also, as with the other road surface classes, it can be seen that the cross-polar normalised RCSs are significantly lower, also indicating that multiple scattering contributions play a limited role for old asphalt.

3.6.2. Normalised RCS of Various Anisotropic Road Surface Conditions

As mentioned in section 3.2, two assumptions are made to extract radar cross sections. One of these assumptions requires the surface-under-test to be isotropic, so that the distribution of its normalised scattering parameters does not depend on the azimuth angle of the incident and scattered waves.

However, not all paving materials have isotropic geomet-rical properties, most notably pavements made out of bricks or stone blocks. This type of road surface is com-monly found in historic city centres and is becoming in-creasingly popular for low speed roads as it is an effective traffic calming method, thus reducing driving speed and therefore increasing safety [33].

To be able to find the normalised radar cross sections of anisotropic surfaces, the second assumption is relaxed so that also the statistical properties underlying the normalised scattering parameters of anisotropic road surfaces can be found. This can be done by substituting the first assumption in section 3.2 with the new assumption below:

- All scattering elements within a measured range bin experience the same azimuth angle of the incident and scattered waves.

This new assumption is valid in a number of situations. For example, if measurements are performed with a radar with high angular resolution, then the variation of azimuthal angle within a range-angle bin is limited, thus the second assumption holds, as long as this angle is smaller than the azimuthal variation of the scattering parameters. Alternatively, if measurements are done with an antenna with a narrow beam in the azimuthal direction, then the majority of backscattered power from a surface-under-test will be from surface area within that beam. As the beamwidth is small in this case, this means that the majority of backscattered power results from a narrow surface area which approximately shares the same azimuthal angle. Therefore, backscattering contributions from surface areas outside of the beam can be neglected, and thus the properties of the scattering process can be successfully computed.

To study the effects of anisotropy of road surfaces on their radar cross sections, measurements were performed on two types of common anisotropic road surfaces. These surfaces comprise two types of brick-paved road surfaces shown in Figs. 3.3a and 3.3b.

The first type of road was made out of a red brick laid in a 45° herringbone bond pattern, while the second type was a grey brick road laid in a running bond pattern. Both types of road surface were measured in the driving direction (indicated by the $\|$ symbol) and perpendicular to the driving direction (indicated by the $\perp$ symbol), as may be encountered at an intersection. Each surface was measured 50 times with an antenna orientation angle of 60°, as per the procedure described in detail in [29].


(a)
(b)

Figure 3.3: The measured anisotropic road surfaces. The red arrow indicates the driving direction (||), while the blue arrow indicates the perpendicular direction (⊥). (a) Red brick pavement. (b) Grey brick pavement.

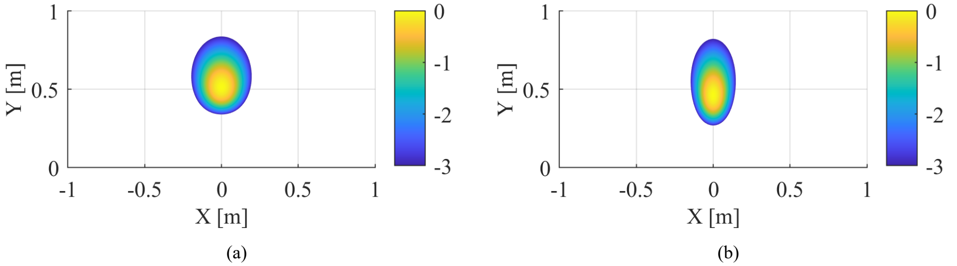

Figure 3.4: Footprint of the antenna beam in dB of the measurement setup in: (a) VV-polarised mode. (b) HH-polarised mode.

As mentioned in third paragraph of this section, radar cross sections can successfully be determined from radar measurements if the radar system has a sufficiently narrow beam. The measurement setup used in this experimental campaign comprises of a vector network analyser (VNA) with both of its channels connected to a 15 dB dual polarised horn antenna. Figs. 3.4a and 3.4b shows the simulated -3 dB footprint of this measurement setup for the vertically and horizontally co-polarised channels respectively. From these figures, it can be seen that for the VV-polarised mode, the -3 dB footprint fits in a cone of approximately ±30°, while in HH-polarised mode, the widest beamwidth is approximately ±25°. This essentially means that the widest range bin covers this angle, while other range bins cover a smaller angular range of the surface. For the considered type of surfaces, it was found that these maximum beamwidths were sufficient for this experiment as the two considered measurement azimuth angles are 90° apart.

Fig. 3.5a and Fig. 3.5b show the NRCS results for the red brick and grey brick surfaces respectively, obtained by the post-processing procedure described in [29]. It can be seen in Fig. 3.5a that for the red brick surface, there is a slight decrease in the co-polar normalised radar cross sections, with the largest decrease occurring in the horizontal polarised channel. This can likely be explained by the length and orientation of the slits between the bricks with respect to the azimuth of the incident wave. In the driving direction, all slits are oriented at 45° with respect to the incident wave. When measuring in the parallel direction, the slits

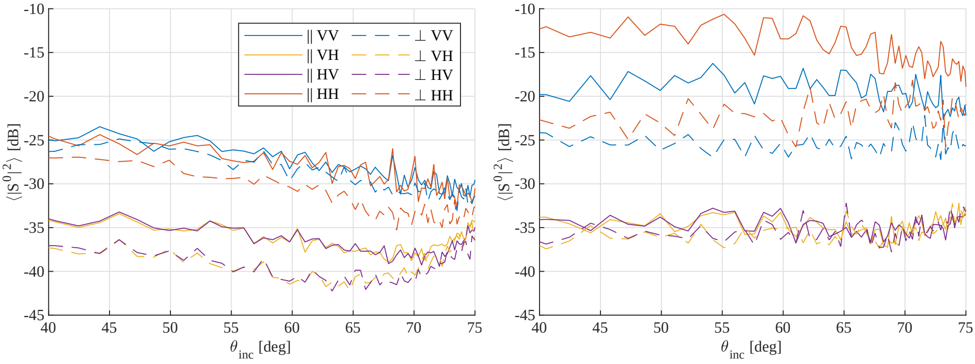

(a)

(b)

Figure 3.5: Normalised radar cross sections of anisotropic pavements, measured in the driving (||) and perpendicular directions (⊥). (a) Red brick pavement. (b) Grey brick pavement.

are still oriented at 45°, thus leading to similar NRCSs.

For the grey brick pavement, a significant difference between the HH- and VV-polarised NRCS can be seen from Fig. 3.5b when measured in the driving direction. This likely indicates that the slits in between the bricks play a significant role in its scattering behaviour, as slits on the long side of the bricks are mainly oriented along the horizontal direction and perpendicular to the radar, thus leading to more backscattered power for horizontally polarised waves compared to vertical polarisation.

Furthermore, the grey brick pavement, when measured in the perpendicular direction, shows a significant decrease of the co-polarised NRCSs compared to the measurements in the driving direction. This can be explained by the slits on the long side of the bricks now being oriented in the same direction as the incident sensing wave, leaving only the slits on the short side of the bricks oriented perpendicular to the incident wave. This effectively reduces the total length and number of slits perpendicular to the radar, thus reducing their contribution to the total backscattered power. Therefore, the total backscattered power is reduced and the difference between the VV- and HH-polarised NRCS decreases as the relative contribution of rough surface scattering increases.

It is also interesting to note that for the red brick pavement, the cross-polarised radar cross section decreases for measurements in the perpendicular direction compared to the driving direction, whereas it remains approximately similar for the grey pavement. It can also be seen that from an incident angle of about 70°, the cross-polarised RCS starts to increase. This is likely due to the sensitivity of the measurement setup, where the measurements from this angle onwards start to be dominated by noise. A more detailed discussion on this phenomenon can be found in [29].

Both pavements were also measured under wet conditions along the driving direction, similar to the approach described in [34]. The results of these measurements for the red brick pavement can be found in Fig. 3.6a, while the results for the grey brick pavement can be found in 3.6b. It can be seen that in the case of the red brick pavement, the presence of water does not change the NRCS significantly for all channels. This is likely due to the good drainage the slits in this type of brick provide, and thus puddles of standing water do

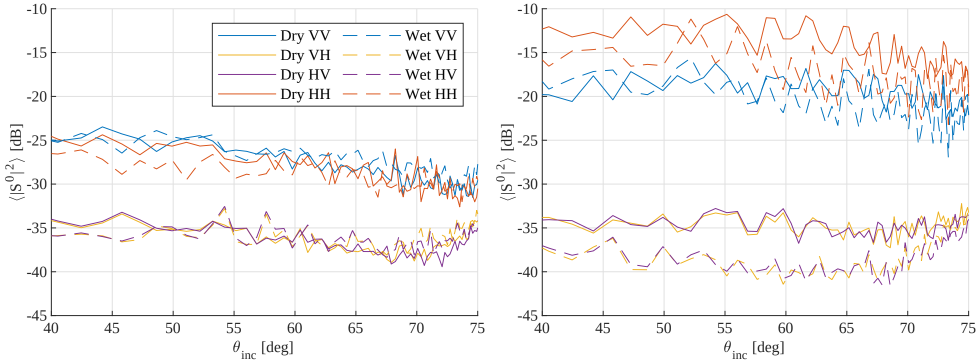

(a)

(b)

Figure 3.6: Normalised radar cross sections of anisotropic pavements in dry and wet conditions, measured in the driving (||) direction. (a) Red brick pavement. (b) Grey brick pavement.

not form.

The NRCSs of the grey brick pavement is more influenced by the water layer compared to the red pavement. It can be seen that the HH-polarised normalised RCS reduces slightly while the VV-polarised normalised RCS remains similar to that of the pavement measured in dry conditions. Thus, in this case of the wet grey brick pavement, this can likely be explained by the water layer smoothing out the slits between the bricks, which leads to a visible reduction in the HH-polarised NRCS.

Furthermore, it can be seen that for the grey brick surface the cross-polar NRCS reduces. This can potentially also be explained by the increase in effective flatness, which results in a change in scattering behaviour towards scattering from a flat dielectric interface. This same phenomenon is also observed in scattering from wet asphalt road surfaces [34].

Understanding scattering from anisotropic road surfaces is important as brick pavements are a common class of road surfaces that are usually encountered in areas where also vulnerable road users are present, or where the road is even shared with them. Therefore, it is important to have a good understanding of the behaviour of the radar cross sections of these surfaces, as increased amounts of clutter may influence radar measurement data that is to be used in safety-critical advanced driver assistance systems such as automatic braking.

Furthermore, anisotropic road surfaces also pose an interesting challenge for driver assistance systems that are concerned with the properties of the road surface. Examples of these systems are the anti-lock braking system and electronic stability control. For example, when a radar system is used for classification of road surface mate-rials, e.g., to estimate its friction coefficient, a change of pavement direction could lead to misclassification of the surface thus potentially impacting safety system performance. This may for example occur at an intersection where different brick bond patterns have to be merged and the radar system might misclassify the road surface at the intersection as covered by a puddle of water. This can cause dangerous situation where a driver suddenly has to brake, without optimal brake performance, to avoid collision with traffic that enters the intersection unexpectedly. Finally, anisotropy of road surfaces, when understood properly, can also be used to aid in classification of road surface materials. When a radar system with good angular resolution or a system with multiple radar channels at different azimuth angles is used for road surface classification purposes, the variation of the measured backscattering along azimuth can also be used to increase the classification accuracy.

3.6.3. Range Profile and Range Doppler Synthesis

As described in section 3.3, the extracted normalised RCS models can be used to synthesise surface scattering in automotive radar scenarios and simulate range profiles and range-Doppler spectra. The first step in such syntheses is to determine a suitable probability distribution that fits the measurement data well. Histograms of the measured magnitude and phase in the 59°-61° incident angle interval of S_{HH} for dry asphalt are shown and compared to a Rayleigh distribution in Figs. 3.7a and 3.7b. It can be seen that a Rayleigh distribution provides a reasonable fit for the magnitude and that the phase seems to approach a uniform distribution. This observation also holds for the other scattering parameters and also applies to those of wet and basalt-covered asphalt. Therefore, in this case the real and imaginary parts of the synthesised scattering parameters can be modelled as normally distributed random variables with covariance and mean values as determined during the normalised RCS model derivation procedure. Furthermore, it is important to note this synthesis method is not limited to normally distributed random variables and thus any multivariate distribution can be used to potentially achieve a better fit to the measurement data.

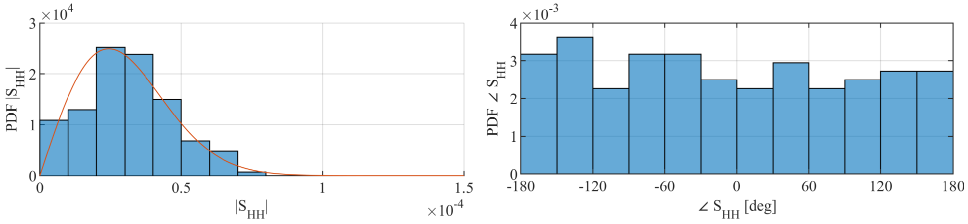

(a)

(b)

Figure 3.7: Histograms of S_{HH} of dry asphalt in the incident angle interval of 59°-61°, normalised to represent the probability density functions. (a) Magnitude, with a comparison to a Rayleigh distribution (in red) with identical variance as the measurement data. (b) Phase.

Subsequently, to represent scattering from the road surface, a grid of scattering elements over the road surface is generated. For each scattering element, a full scattering matrix is generated using a multivariate normal distribution with the extracted statistical properties corresponding to the surface type. Next, the contribution of each element to the total received power, including the effects of antenna gain, propagation losses, and surface area of the grid element, is computed following the procedure described in section 3.3. Fig. 3.8a shows the contributions to the VV-polarised channel from surface elements simulating a dry asphalt surface as seen by a dual-polarised horn antenna, placed at a height of 38 cm with an orientation angle of 60°. In this plot, the effect of the side lobe of the horn antenna manifests itself as a maximum around the origin. Even though the side lobe level of the dual polarised horn is about -14 dB, the lower gain for the scattering elements near the origin is compensated by the shorter range and corresponding lower propagation losses compared to the scattering elements that lie in the main lobe. As the antenna is placed at a height of

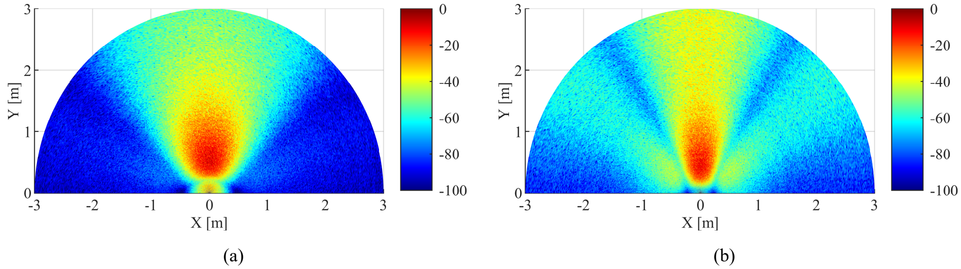

Figure 3.8: Normalised received power from surface scattering elements simulating dry asphalt, including effects of propagation losses, scattering element surface area, and the gain of a dual-polarised antenna at a height of 38 cm with an orientation angle of 60°: (a) VV-polarised channel; and (b) HH-polarised channel.

38 cm with an orientation angle of 60°, the point of maximum gain is located at a ground range of about 66 cm directly in front of the antenna. However, the surface scattering elements that provide the strongest contributions to the total backscattered response are centred around 56 cm. This is also caused by the longer range to the scattering element that sees the maximum antenna gain and thus higher propagation losses occur which reduces the total contribution of the elements located around 66 cm compared to those centred around 56 cm directly in front of the antenna.

As described in 3.3, a range profile can be found by summing the contributions of each scattering element to their corresponding range bin. The results of this procedure are shown in Fig. 3.9. In this plot, also a comparison with measurement data from a dry asphalt surface is shown. Excellent agreement can be seen between the simulated and measured range profiles up to a range of 1.5 m. From this range onward, the measurement data of the magnitude of S_{VV} is limited by noise, whereas the simulated range profile shows the expected decrease with range due to increased propagation losses and decreased antenna gain.

From Fig. 3.8, also the range-Doppler spectra can be synthesised using the procedure described in 3.3. Assuming a platform speed of 15 km/h and adding the surface scattering contributions to their corresponding range-Doppler bins results in the range-Doppler spectra shown in Fig. 3.10. It can be seen that the range-Doppler signature of the asphalt surface spreads over the Doppler domain due to scattering from surface area that is not directly in front of the moving platform.

Furthermore, it can be seen that most power is contained in the sector of the range-Doppler plot delimited by the speeds smaller than -2 m/s and ranges closer than 1.5 m to the platform due to the 60° orientation angle of the horn antenna. Also, in the VV-polarised channel, a relatively large return in the range-Doppler bins at a range of 0.45 m and at velocities between -1.5 and 0 m/s can be seen. This is due to the side lobe of the dual-polarised horn antenna, which increases the return from the surface area underneath the antenna.

In the HH-polarised channel, the part of the range-Doppler spectrum bounded by velocities of -3 and -3.5 m/s and a range larger than 1 m shows relatively less backscattered power compared to the VV-polarised channel while at ranges up to 1 m and velocities higher than -3 m/s, more scattered power is observed. This is also caused by side lobes of the dual-

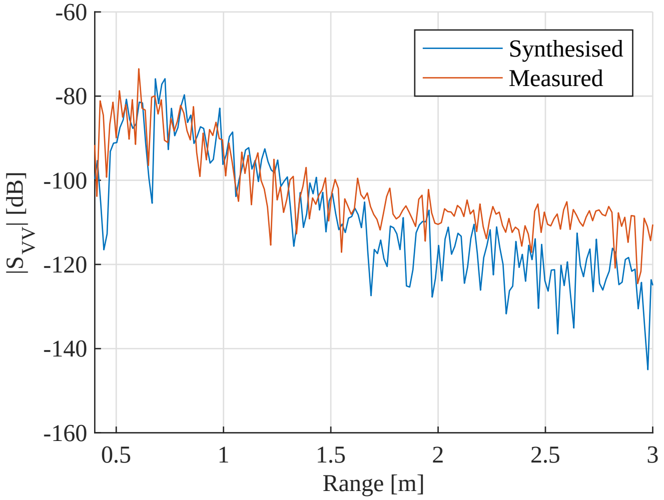

Figure 3.9: Synthesized range profile of the VV-polarised channel from a uniform dry asphalt road surface compared to measurement data performed on a dry asphalt road surface with a dual-polarised horn antenna with an antenna orientation angle of 60°.

polarised horn antenna. Namely, in the H-polarised mode of the antenna, the side lobes are now in the horizontal plane in contrast to vertical plane as is the case for the V-polarised mode. This results in an effectively wider beam at close range in the HH-polarised channel (Fig. 3.8b), resulting in a broader spread over velocity of the backscattered power at these ranges. The nulls between the side lobes and the main lobe together with the slightly narrower main lobe compared to the V-polarised mode, result in the lower amount of backscattered power in the -3.5 to -3 m/s area of the spectrum.

Instead of a dual-polarised horn antenna with an orientation angle of 60°, also antennas with other radiation patterns can be considered. Fig. 3.11 shows the contributions of the surface scattering elements to the backscattered power using a forward looking (90° orientation angle) antenna with a cosine-squared pattern in both elevation and azimuthal planes. Compared to the syntheses with the dual-polarised horn antenna, no side-lobes are present. This leads to a more uniform illumination of the surface, resulting in a more uniform range-Doppler signature as shown in Fig. 3.12. As the radiation patterns for both polarised channels are the same in these plots, the effects of the difference between polarisations of the normalised RCS models can be observed as well. Namely, the range-Doppler spectrum of the VV-polarised channel (Fig. 3.12a) shows a stronger return that is more extended in range than is visible in the HH-polarised range-Doppler spectrum (Fig. 3.12b). This is consistent with the normalised RCS model of dry asphalt (Fig. 3.2a) that shows that the HH-polarised normalised RCS decreases more with range than the VV-polarised normalised RCS.

Besides surfaces comprising completely of dry asphalt, also surfaces comprising of multiple different surface conditions can be simulated. This is done by assigning parts of the surface scattering elements different normalised RCS models. An example of such a surface is shown in Fig. 3.13, which represents a puddle of water in front and gravel to the right hand

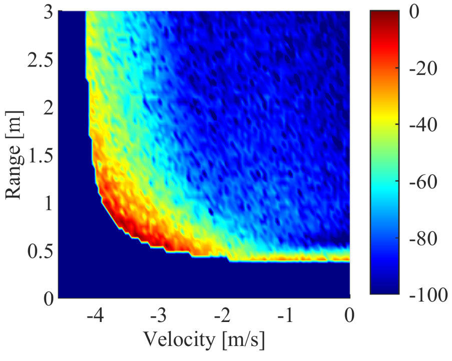

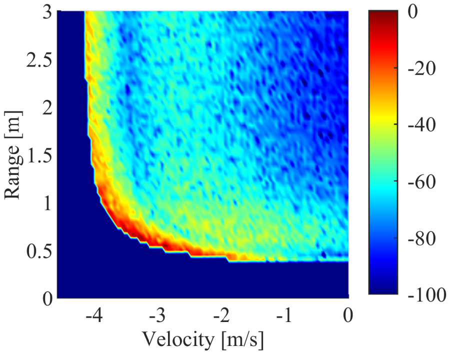

(a) (b)

Figure 3.10: Synthesized range-Doppler spectrum of a uniform dry asphalt road surface of a dual-polarised horn antenna with an antenna orientation angle of 60°, moving at a speed of 15 km/h as observed in the: (a) VV-polarised channel; and (b) HH-polarised channel.

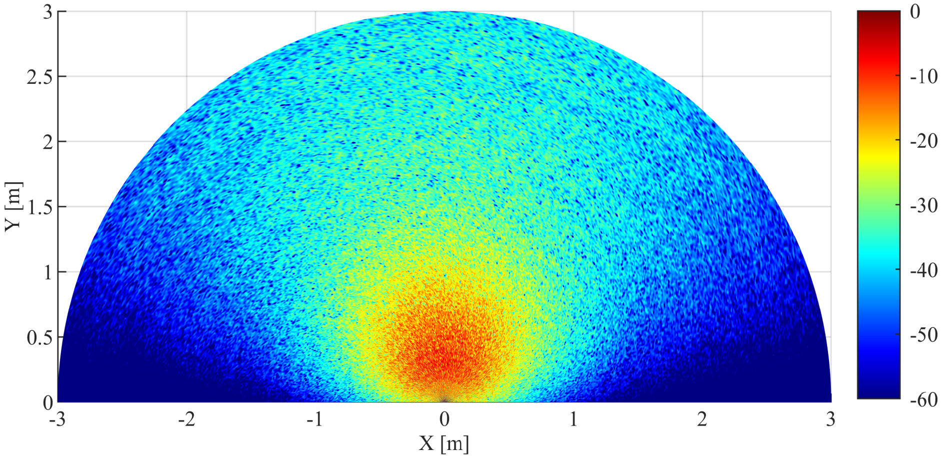

Figure 3.11: Normalised received power from surface scattering elements in the VV-polarised channel simulating dry asphalt, including effects of propagation losses, scattering element surface area, and the gain of a forward looking cosine-squared antenna at a height of 38 cm.

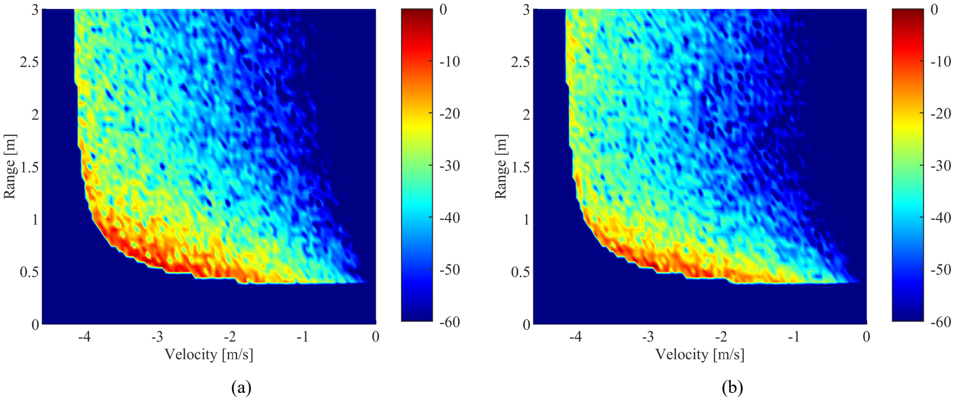

Figure 3.12: Synthesized range-Doppler spectrum of a uniform dry asphalt road surface illuminated by a forward looking antenna with cosine-squared pattern, moving at a speed of 15 km/h as observed in the: (a) VV-polarised channel; and (b) HH-polarised channel.

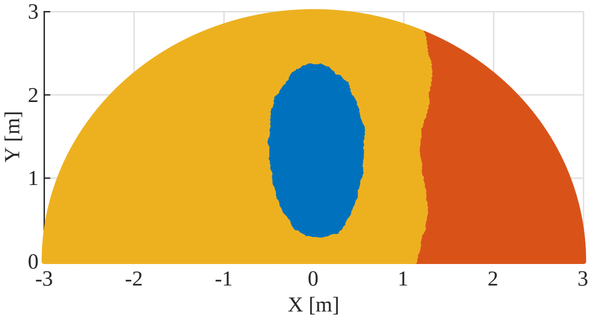

Figure 3.13: Road surface conditions definition for a synthesis comprising of multiple different surface types. Orange corresponds to dry asphalt, while blue and red correspond to wet and basalt-covered asphalt respectively.

side of the vehicle. In this scenario, also a forward looking antenna with a cosine-squared pattern is used for both polarisations.

The synthesised surface scattering contributions for the HH-polarised channel are shown in Fig. 3.14. Here, the distinction between the wet and dry asphalt is clearly visible. This is clear from the normalised RCS models, as the normalised RCS of wet asphalt (Fig. 3.2b) is much lower than that of dry asphalt (Fig. 3.2a). The difference between the dry and basalt-covered areas is also visible in Fig. 3.14. However, the distinction is less clear as the difference between the normalised RCS of basalt-covered asphalt (Fig. 3.2c) and dry asphalt is smaller than the difference with wet asphalt.

Also, range-Doppler spectra can be generated from Fig. 3.14 and its VV-polarised counterpart. This is shown in Fig. 3.15. Compared to the range-Doppler spectra of a uniform dry asphalt surface (Fig. 3.12), it can be seen that the power in the -4 to -3 m/s sector is reduced due to the decreased backscattering caused by the puddle of water. Also, in the HH-polarised channel, a diagonal line starting at a velocity of -1 m/s and a range of 1.4 m

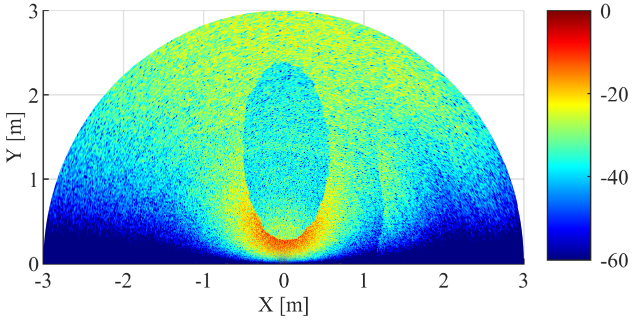

Figure 3.14: Normalised received power from surface scattering elements in the HH-polarised channel simulating the scenario from Fig. 3.13, including effects of propagation losses, scattering element surface area, and the gain of a forward looking cosine-squared antenna at a height of 38 cm.

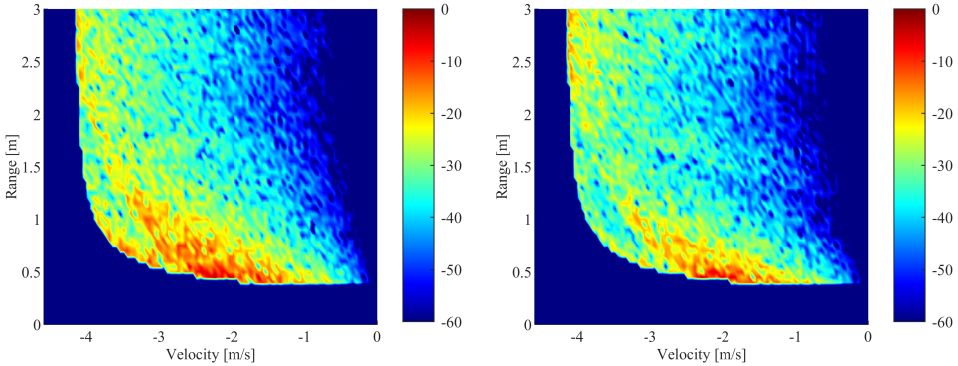

(a)

(b)

Figure 3.15: Synthesized range-Doppler spectrum of the road surface conditions as defined in Fig. 3.13 using a forward looking antenna with a cosine-squared pattern, moving at a speed of 15 km/h as observed in the: (a) VV-polarised channel; and (b) HH-polarised channel.

is visible. This line corresponds to the gravel on the side of the road which is about this distance away from the radar antenna. Note that it is easier to observe this line in the HH-polarised channel as the contrast between the gravel and dry asphalt is larger due to the larger difference in normalised RCS in this channel as can be seen from Figs. 3.2a and 3.2c.

Finally, it should be noted that in this section, the presented synthesis results were computed up to a distance of 3 metres as the normalised radar cross section is largest and shows the most variation in this area. This distance is likely still enough for e.g., automatic anti-lock braking system adjustments given the processing capabilities of modern automotive on-board computers even when the vehicle's velocity is significant. However, the proposed synthesis method can be made arbitrarily large, and is limited only by the accuracy of the statistical normalised RCS models at shallow angles of incidence that correspond to these larger ranges.

3.6.4. Optimal Polarisation Selection

The models of the normalised RCS of the road surface types can also be used to determine the optimal sensing wave polarisation for single-polarised radar and other polarimetric applications such as filters to increase or suppress scattering from road surfaces. By factorising the antenna polarisation vector in two quantities, the optimal polarisation for minimising or maximising the received power from a target of interest can be determined numerically as described in section 3.4.

As an example, this procedure is performed on the four different measured road surface types. The results for the normalised RCS models at a distance of 68 cm, the distance at which the surface scattering contributions are highest, are shown in Fig. 3.16. These figures show the normalised received power as function of sensing wave polarisation. It can be seen that in the case of dry, wet, and old asphalt, maximum received power is achieved for a value of A of 1, which corresponds to vertical polarisation. In the case of basalt-covered asphalt, horizontal polarisation ($A = 0$) would result in maximum received power. However, as can be seen from Fig. 3.16c, using vertical polarisation results for basalt-covered asphalt in a loss of less than 1 dB compared to a horizontally polarised sensing wave. This observation is backed up by the normalised RCS models as shown in Fig. 3.2c, as the normalised VV-polarised RCS is within 1 dB of the normalised HH-polarised RCS. Therefore, it can be concluded that for a single-polarised radar system, a vertically polarised sensing wave is optimal when the goal is to maximise the backscattered return from the measured road surface types.

However, the situation for suppressing returns from the road surface is less obvious as all four measured road surface classes have their minima located at different polarisations. In the case of wet asphalt, minimal return is achieved at linear polarisation that is slightly offset from horizontal polarisation ($A \approx 0.2$, $\delta \approx \pm 180^\circ$) while for the other three classes elliptical polarisations should be used. In the case of dry asphalt, a polarisation with $A \approx 0.55$ and $\delta \approx \pm 100^\circ$ would yield best results, whereas for basalt-covered asphalt a polarisation with $A \approx 0.75$ and $\delta \approx \pm 100^\circ$ would. In the case of old asphalt, a polarisation with $A \approx 0.7$ and $\delta \approx 70^\circ$ would result in minimal returned power.

Since there is no polarisation that achieves minimal received power for all road surface condition classes, a designer of a single-polarised radar system must perform a trade-off to achieve optimal performance regarding antenna polarisation. For example, the designer must consider the relative frequency with which the road surface conditions occur. Namely, if the wet and basalt-covered road surface conditions are expected to show up very rarely, it would be beneficial to select the polarisation that achieves minimal received power for dry asphalt. Another considerations that may play a role is the absolute amount of power received from a road surface type, e.g. power backscattered from wet asphalt could already be negligible compared to that from the targets-of-interest and thus the wet asphalt could be left out of the analysis.

Thus, to reach optimal performance regarding the signal to clutter ratio, in practice a designer has to formulate a score function that should for example contain weighting factors based on relative frequency of appearance of the to be suppressed clutter type, as well as the magnitude of the RCS of said clutter. Also, the score function should contain weights for the RCS models of targets-of-interest based on the same factors as previously mentioned for clutter to increase the received power from the desired targets as much as possible to

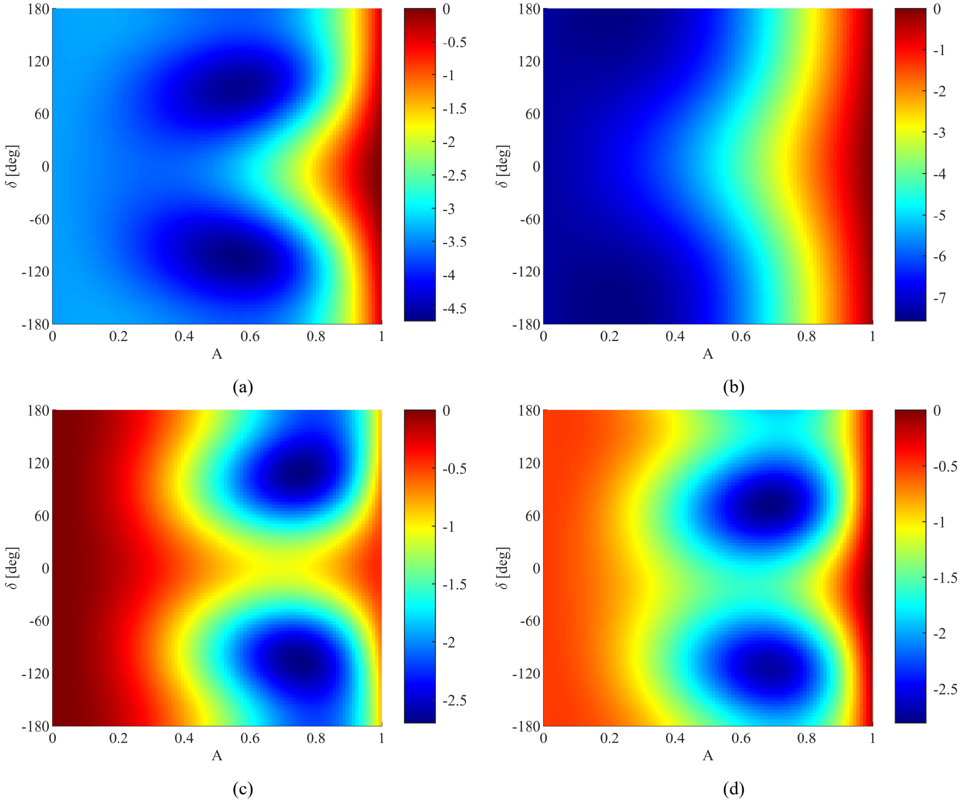

(a) (b)

(c) (d)

Figure 3.16: Normalised returned power in decibels for a single-polarised radar system for the four measured road surface classes at a distance of 68 cm from the antenna located 38 cm above the surface. (a) Dry asphalt. (b) Wet asphalt. (c) Asphalt covered by basalt split ranging in size from 2 to 8 mm. (d) Old asphalt.

eventually maximise the signal to clutter ratio.

3.7. Conclusions

A novel method of deriving the statistical properties of surface backscattering from range profile measurements is proposed. The method is based on modelling the surface as a collection of uncorrelated scattering elements, with all elements having a normalised scattering matrix that is characterised by a multivariate distribution. Assuming the surface-under-test is isotropic and that all surface scattering elements within one range bin experience the same angle of incidence, it is shown that the mean value and covariance can be computed from measured range profile data.

This method is then applied to measurement data collected with a VNA equipped with a dual-polarised horn antenna in the frequency band ranging from 75 to 85 GHz. It is shown that the statistical properties of two different types of asphalt as well as three different road surface conditions could be determined successfully, thus demonstrating the general applicability of the method. Specifically, relatively new unused and heavily used old asphalt were considered where the new asphalt type was measured in three different conditions which were dry, wet, and covered with basalt gravel. It is shown that gravel-covered asphalt and old asphalt behave as an electromagnetically rough surface as both magnitudes of co-polarised radar cross sections are on the same level, and show a decay as function of incident angle corresponding to a cosine, leading to the conclusion that these surface classes resemble Lambertian scattering behaviour. For the dry and wet asphalt surface types, the co-polarised radar cross sections show an increasing difference between the vertically and horizontally polarised RCS with an increase of the incident angle. In the case of dry asphalt, this difference increases from less than 1 dB to over 4 dB in favour of the vertically polarised RCS. In the case of wet asphalt, the radar cross section was found to be over 10 dB lower than that of dry asphalt. As with the RCS of dry asphalt, the HH-polarised RCS decreases with incident angle quicker than the VV-polarised RCS. Furthermore, it can be seen that the contribution of multiple scattering events to the total received backscattered power is relatively marginal for all four road surface classes as the cross-polarised radar cross sections are significantly lower than the co-polarised ones.

Also, measurements of two types of brick pavements were performed. The first surface class comprised a type of red brick laid in a 45° herringbone bond pattern, while the second type consists of a type of grey brick, laid in a running bond pattern. Both surfaces were measured in driving direction and perpendicular to this direction.

It is shown that for the red brick pavement, the variation in NRCS is relatively limited between driving and perpendicular directions, while for the grey brick surface, the NRCS showed significant differences. From the computed NRCSs, it was found that this behaviour can likely be explained by the orientation of slits between the bricks, which increase the HH-polarised RCS significantly when perpendicular to the radar.

Both surface types were also measured in wet conditions in the driving direction to study the impact of the water layer in terms of reduction of the scattering contributions of the slits between bricks. Here, it was found that the water layer significantly influences the NRCS of the grey brick type, while the variation of the NRCS of the red brick pavement is relatively little.

Furthermore, two applications of the derived statistical normalised radar cross section models are proposed. Firstly, a novel procedure to synthesize surface clutter in range profiles, range-angle plots and range-Doppler spectra is proposed. This procedure is subsequently applied to simulate range profiles and range-Doppler spectra of a dry asphalt surface and excellent agreement with measured range profiles is shown. The procedure is also demonstrated to be able to simulate surface scattering from a surface consisting of multiple different road surface conditions. It is shown that for example a puddle of water in front of the radar platform and gravel to the side of the platform respectively de-emphasize and emphasize corresponding areas in the range-Doppler spectrum.

Secondly, a novel method for determining the optimal sensing wave polarisation for a single-polarised radar system based on (statistical) RCS models is presented. This procedure utilises a factorisation of the antenna polarisation vector in two different parameters, namely A and δ. Since these parameters are respectively bounded by 0 and 1 and -180° and +180°, the maxima and minima of the received power can be found numerically. It is shown that the optimal sensing wave polarisation depends on the intended application of the radar system and that the proposed method can be used to find this optimum. Using the proposed procedure and the normalised RCS models of the four measured road surface types, it is determined that a V-polarised sensing wave is optimal to maximise the return from the road surface, which is beneficial when the automotive radar system is intended for e.g., road surface conditions classification. For different applications, it is demonstrated that to find the optimal polarisation for a single-polarised radar system to achieve optimal signal-to-clutter ratio, a score function that includes amongst others weighting factors for each considered target class based on the relative frequency of appearance and the magnitude of the RCS of such a target has to be defined. By subsequently using this score function in conjunction with the proposed method, the optimal polarisation for the radar application corresponding to that score function can be determined.

4

Classification of Road Surfaces using Polarimetric H/α/A Features in Automotive Scenarios

Using the results obtained from chapters 2 and 3, a classification method for identifying road surfaces in various conditions is developed. The signal processing pipeline for this purpose that is introduced in this chapter is based on the polarimetric $H\alpha A$ *decomposition, a concept which was previously used in, amongst others, synthetic aperture radar applications from space.*

Parts of this chapter have been published as:

W. Bouwmeester, F. Fioranelli, and A. Yarovoy, "Convergence of Scattering Parameters and HαA-Features of Road Surfaces", in *20th European Radar Conference (EuRAD)*, Berlin, Germany, 2023.

W. Bouwmeester, F. Fioranelli, and A. Yarovoy, "Road Surface Conditions Identification via H α A Decomposition and Its Application to mm-Wave Automotive Radar", *IEEE Transactions on Radar Systems*, 2023.

4.1. Introduction

In an effort to increase on-road safety, more and more vehicles are being equipped with advanced radar systems. These radar systems are usually employed to detect, and in many cases also classify, other road users and obstacles. Automotive radar systems for the 24 GHz band are being phased out and a transition to the new 77 GHz band has largely been completed [12, 13]. This has presented a new opportunity to use these radar systems to observe road surface conditions in front of the vehicle. Namely, the rough structure of road surfaces results in more power that is scattered back to the radar sensor in the 77 GHz band compared to the 24 GHz band due to the shorter wavelength.

On the one hand, this causes the radar to detect more clutter. However, instead of considering these returns as clutter, they can also be used in an effective way to estimate the road surface conditions in front of the vehicle, e.g. whether the road surface is dry, wet or icy, or covered with potentially slippery material. Information on the road surface condition up ahead is crucial for improving driving safety systems such as the anti-lock breaking system and electronic stability control. If these systems can be provided with an estimation of the road surface conditions up ahead, they could already be tuned closer to the right operating point to minimise braking distance and maximise vehicle stability [35]. In the case of fully-autonomous driving, dangerous road surface conditions such as a patch of ice could be automatically steered around altogether.

Road surface classification has been investigated using conventional (single polarised) radar; a few notable examples of this can be found in [7, 17, 36, 37]. In [17, 36], convolutional neural networks are used on vertically polarised radar imagery of sandpaper and rough surface types, while in [7] the statistical distribution of vertically polarised backscattering from a number of road surface conditions was studied. Also in [37], surface classification was performed by fitting a Weibull distribution to the backscattered power and studying the resulting variation of the distribution parameters.

Polarimetric radar has the distinct advantage that the full polarimetric characteristics of the targets of interest are measured. As different targets have different polarimetric characteristics, the extra information provided by this ability can be used for classification. This is for example routinely used in the context of remote sensing, target classification and weather radar [38–40]. Surfaces have distinctive polarimetric scattering behaviours depending on surface roughness (i.e., parameters such as the root mean square height and correlation function) and material properties [41]. This makes polarimetric radar a great candidate to exploit different scattering behaviours for road surface classification purposes in the automotive context.

Previous publications have considered using polarimetric features for road surface identification [6, 28, 42]. In that research, simple polarimetric features such as the co-polar and cross-polar backscattering ratios have been utilised. More specifically, [42] and [28] consider the use of polarisation ratios. These include co-polarised horizontal and vertical backscattering ratios, as well as cross-polar backscattering ratios. In [6], the mean powers in the co- and cross-polarised channels were investigated, as well as their standard deviations.

While effective, these features are relatively simple and do not necessarily exploit the whole amount of rich information that can be inferred from more complex polarimetric decompositions. In this work, the polarimetric approach is taken to the next level by introducing a novel processing pipeline specifically designed for automotive radar based on the

$H\alpha A$ decomposition for road surface identification purposes.

The $H\alpha A$ decomposition is known from the field of remote sensing and Earth observation and has been successfully applied to data from, amongst others, synthetic aperture radar [38]. This decomposition operates on the statistical properties of the polarimetric signatures of an object to extract the H, α and A features. Their importance relates to the fact that they can model and capture the physical scattering processes occurring within said object. For example, in the case of Earth observation with synthetic aperture radar, scattering that is characterised by an entropy value, denoted H, between 0.5 and 0.9 and an α value between 40° and 50° corresponds to scattering from anisotropic particles, while scattering with an entropy value between 0 and 0.5 and an α value between 0° and 42.5° corresponds to Bragg surface scattering [32].

However, the $H\alpha A$ decomposition as applied in the aforementioned applications, cannot be used directly in automotive radar. This is due to differences in observation geometry and platform movement. Therefore, to investigate the effectiveness of the proposed approach based on $H\alpha A$ features for road surface identification purposes, a novel processing pipeline is proposed to compute these features in the automotive scenario. The proposed pipeline compensates for the strongly varying distance between observed road surface returns that occurs due to the observation geometry of the automotive scenario, and proposes a new way of averaging of the scattering parameters for computing the coherency matrix.

Subsequently, measurement data of rough surface scattering in both lab conditions as well as outdoors on actual road surfaces has been collected using a vector network analyser. This data is then used to evaluate the proposed pipeline. Furthermore, using the measurement data, a polarimetric analysis is performed to investigate the performance impact on road surface identification when the cross-polar components are omitted. Notably in this case, if the cross-polar channels do not have to be measured, the ADCs (analogue to digital converters) of H and V channels do not have to be synchronised to each other thus making the hardware implementation easier. This means that such a radar could be constructed out of two separate single polarised radar systems. Also, since the backscattered power in the cross-polarised channels is usually much lower, requirements on the sensitivity of the radar system can be relaxed by leaving the cross-polar channels out. The results of the polarimetric analysis can then be used by radar designers to make a trade-off between performance and radar complexity leading to cost savings by leaving out cross-polar measurement capabilities.

In terms of contributions of this work, the obtained results show that the proposed pipeline is effective for road surface classification purposes and provides a robust alternative to a state-of-the-art classification technique based on polarimetric ratios. It has also been shown that the cross-polar components can be neglected, at the cost of reduced separation between clusters formed by the H, α and A features of the considered classes of road surfaces.

The rest of this chapter is laid out as follows: in section 4.2, an introduction to the $H\alpha A$ decomposition is provided. Section 4.3 describes the measurement setup and the measurement procedure whilst section 4.4 describes the proposed pipeline for road surface identification. In section 4.5 the experimental results are presented and the convergence of the H, α, and A features is discussed in section 4.6. The chapter concludes with section 4.7.

4.2. Theoretical Background

The $H\alpha A$ decomposition, introduced by Cloude and Pottier and originally developed for synthetic aperture radar, does not depend on knowledge of statistical distributions of targets, but assumes instead that there is a dominant average scattering mechanism and tries to find the characteristics of this scattering process [38]. The approach is based on Eigendecomposition of the so called coherency matrix T.

The computation of the H, α and A features works as follows. The first step is to compute the target vector $\vec{k}$ as shown in (4.1), where S_{XX} refers to the co-polar scattering matrix element for X polarisation, measured in a XY polarisation basis [32]. In this equation, ^{T} indicates the transpose operator.

$$\vec{k} = \frac{1}{\sqrt{2}} \begin{bmatrix} S_{XX} + S_{YY} & S_{XX} - S_{YY} & 2S_{XY} \end{bmatrix}^T \tag{4.1}$$

In this chapter, a vertical/horizontal polarisation basis is used which leads to X corresponding to V polarisation and Y to H polarisation. Subsequently, using this target vector, the coherency matrix can be computed as shown in (4.2), where † indicates the conjugate transpose operator and the angle brackets indicate averaging.

$$T = \left\langle \vec{k}\vec{k}^\dagger \right\rangle \tag{4.2}$$

In synthetic aperture radar applications, this averaging is usually done over multiple cells in space where these cells contain the same (type of) object. However, for the proposed road surface classification approach in automotive scenarios, this averaging step can also be performed in a different manner as described in section 4.4.5.

Next, an Eigendecomposition is performed on the coherency matrix, resulting in 3 eigenvalues, denoted by λ_i, in order from larger to smaller, with λ_1 being the largest and λ_3 the smallest. The eigenvector corresponding to each eigenvalue λ_i is denoted by $\vec{u}_i$.

For each of the three eigenvalues, a pseudo-probability P_i can be computed as shown in (4.3) [32].

$$P_i = \frac{\lambda_i}{\sum\limits_{k=1}^{3} \lambda_k} \tag{4.3}$$

Using the pseudo-probabilities corresponding to each eigenvalue, the entropy feature, denoted by H, can be computed as shown in (4.4) [38].

$$H = -\sum_{i=1}^{3} P_i \log_3 P_i \tag{4.4}$$

The entropy feature is a measure of how random the backscattering from a target is and whether or not there is one dominant scattering mechanism occurring, or if there are multiple dominant scattering mechanisms at play. When there is only one dominant scattering mechanism, the entropy is low and indicates deterministic scattering. When there are multiple dominant scattering mechanisms present, the observed scattering mechanism varies from observation to observation thus indicating a random scattering character which corresponds to a high entropy value.

Each eigenvector $\vec{u}_i$ can be represented in the form as shown in (4.5) [32].

$$\vec{u}_i = \begin{bmatrix} \cos\alpha_i e^{j\phi_i} \\ \sin\alpha_i \cos\beta_i e^{j(\delta_i+\phi_i)} \\ \sin\alpha_i \sin\beta_i e^{j(\gamma_i+\phi_i)} \end{bmatrix} \tag{4.5}$$

By using the identity shown in (4.5), the values of α_i, β_i, ϕ_i, δ_i and γ_i can be computed for each eigenvector. Subsequently, the feature α can be found by computing a weighted average based on the pseudo-probabilities, as shown in (4.6) [32].

The angle α indicates the nature of the average scattering mechanism. For example, an α value of 0° relates to scattering from a spherical target whereas values of 45° and 90° correspond to scattering from anisotropic particles and dihedrals, respectively [32].

$$\alpha = \sum_{i=1}^{3} P_i \alpha_i \tag{4.6}$$

Finally, the anisotropy feature A can be computed as in (4.7).

$$A = \frac{\lambda_2 - \lambda_3}{\lambda_2 + \lambda_3} \tag{4.7}$$

The anisotropy feature A indicates how much of a role the eigenvector with the smallest eigenvalue has in the scattering process compared to the second-largest. This indicates the relative importance of the second scattering mechanism compared to the third scattering mechanism in the averaged response.

These three features can subsequently be used to make a classification of targets. In the case of synthetic aperture radar for Earth observation, the H and α features are often plotted against each other, creating a $H\alpha$-plane. This plane is subdivided in a number of sectors, where for example the sector that is delimited by $H < 0.5$ and $\alpha > 47.5^\circ$ corresponds to scattering from a dihedral reflector and the sector delimited by $0.5 < H < 0.9$ and $\alpha < 40^\circ$ corresponds to scattering from a random surface [32]. This direct relation to the underlying physical scattering mechanisms give the $H\alpha A$ decomposition a distinct advantage over simpler features such as the co-polar/cross-polar ratios, or mean values and standard deviations of polarimetric channels.

The background theory presented in this section relates to the application of the $H\alpha A$ decomposition for Earth observation. Section 4.4 discusses the proposed extra steps to apply this decomposition to the automotive scenario.

4.3. Experimental Measurements

In this section the experimental setup is described, together with the measurement procedure in the laboratory, as well as the procedure for outdoor measurements.

4.3.1. Measurement Setup

Measurements were performed with a N5242A Vector Network Analyser (VNA) with two N5260-60003 frequency extenders to be able to operate in the band ranging from 75 to 85

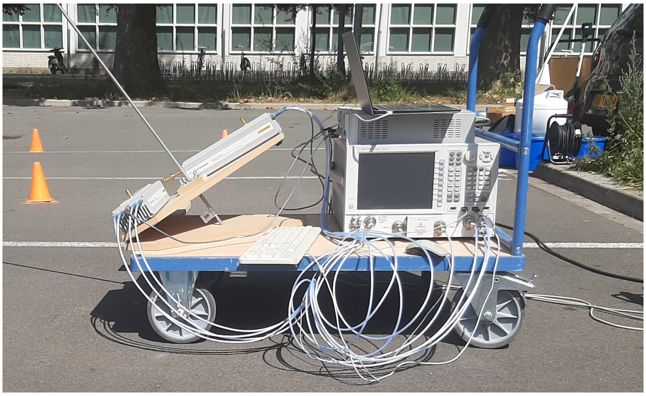

Figure 4.1: Photograph of the measurement setup as used for outdoor measurements. The setup consists of a VNA with mm-wave extenders connected to a dual-polarised horn antenna with a controllable antenna orientation angle to measure the surface-under-test under various angles of incidence.

GHz. The frequency extenders have WR-10 waveguide output sections, to which a 15 dBi gain dual-polarised horn antenna of type SAR-1532-122-S2-DP [43] was connected using the required waveguide sections. The vertically polarised port of the antenna was connected to the first port of the VNA, while the horizontal port was connected to the second.

A supporting structure was purposely built to which the frequency extenders and dual polarised horn were attached. This structure allows for controlling the orientation angle of the antenna in the vertical plane relative to the surface under test. The antenna orientation angle is defined as the angle the surface normal forms with the antenna broadside. In this way, the samples can be measured under various angles of incidence (Fig. 4.1).

4.3.2. Measurement Procedure

Measurements were performed both under lab conditions indoor, and outdoors on real road surfaces.

During the *lab measurements*, 3 types of sandpapers of different coarseness were used as surface samples, to be more specific P24, P60 and P100. Here, P24 is the coarsest type of measured sandpaper while P100 is the finest. Sandpaper was selected as a suitable sample as it provides a surface of controlled roughness which is uniform over the whole sheet. The P24 type was selected as it was the coarsest sandpaper available on the market that is supplied as large sheets. The P100 type was chosen as a relatively smooth sample while the P60 type was used as an intermediate step. According to standards of the Federation of European Producers of Abrasives, P24 grit sandpaper has an average particle size of 764 µm, while P60 and P100 types have average particle sizes of 269 µm and 162 µm respectively [44]. The root mean square (RMS) height is approximately linearly dependent on average particle size as seen from [45], leading to an estimated RMS height of 220 µm for the P24 type, while the reported RMS height for the P60 and P100 types is 84 µm and 41 µm respectively. All sandpaper sheets measured at least 1.5 metres by 2 metres so that the -10 dB footprint of the antenna beam, for an antenna orientation angle of 60°, is well contained within the sample. The -10 dB antenna beam footprint was computed by using the procedure outlined in [30],

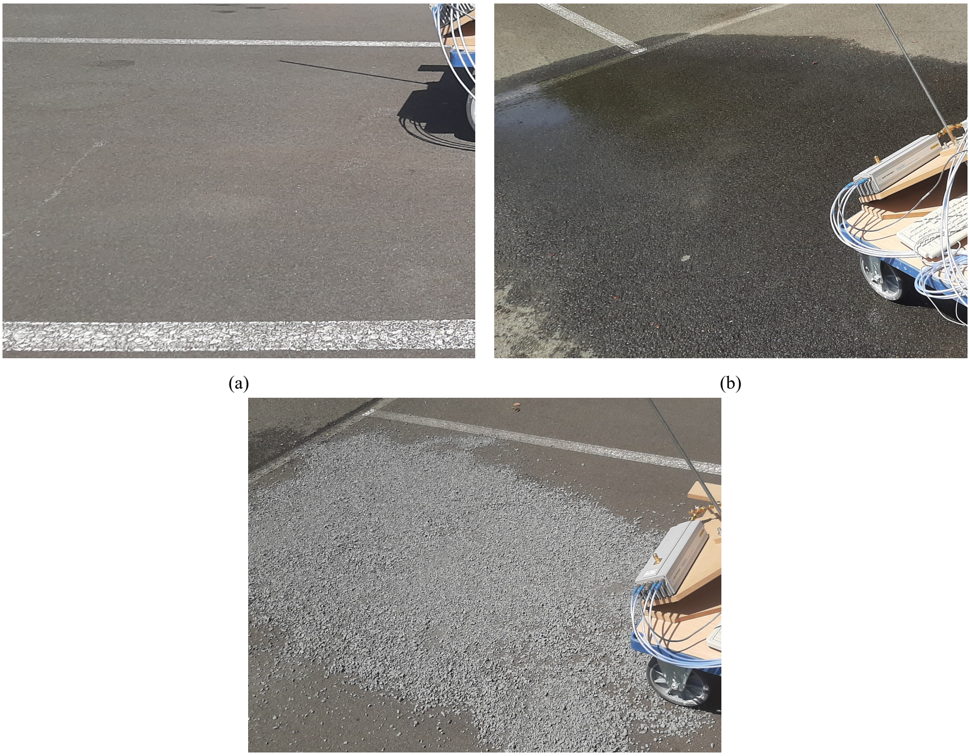

(a)

(b)

(c)

Figure 4.2: Pictures of the measured road surface conditions. (a) Dry asphalt. (b) Wet asphalt. (c) Asphalt covered with gravel, consisting of basalt split with sizes ranging from 2 to 8 mm.

and was found to be an oval of dimensions 95 cm by 44 cm.

In order to collect statistically independent samples, which are needed to compute the coherency matrix as described in section 4.2, the sandpaper sheets were moved a few centimetres in between measurements to ensure that the surface within the antenna beam footprint would be uncorrelated with the previously measured area of the sheet. This is analogues to a car driving along a surface while performing measurements over time, resulting in measurements of uncorrelated surfaces for each time point. For each sandpaper sample, this procedure was repeated 50 times. To ensure stability of the measurements, every tenth measurement an additional measurement without sample was performed and compared to the background measurement done ten measurements before. These background measurements were also used for the background subtraction procedure as described in section 4.4.1.

For the measurements that took place outdoors, the measurement setup was placed on a trolley so that it could be moved easily as seen in Fig. 4.1. Several different road surface conditions were measured, namely asphalt under dry conditions, asphalt under wet conditions, and asphalt covered with gravel as one may encounter during roadworks (Fig. 4.2). All road surface conditions were measured for two antenna orientation angles. These were

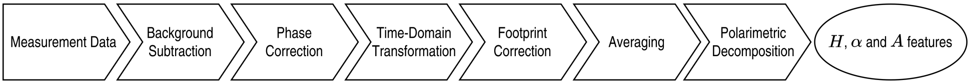

Figure 4.3: Block diagram of the proposed signal processing pipeline for road surface identification for automotive applications using the H, α and A features.

60°, to replicate lab conditions and 90°, to replicate forward looking radar systems.

The measurement procedure for the *outdoors measurements* on asphalt was mostly the same as the lab measurements, except for moving the surface under test: in this case the measurement setup was moved instead. First, measurements were performed on asphalt under dry conditions. Subsequently, to emulate asphalt under wet conditions, buckets of water were poured over the previously measured area of asphalt. Every 10 measurements, more water was poured on the asphalt to keep the water layer consistent. Lastly, gravel, in the form of basalt split ranging from 2 to 8 mm in size was spread out over a dry part of asphalt and measured. As with the lab measurements, for each road surface condition and each antenna orientation angle, the backscattering from the asphalt road surface was measured in 50 uncorrelated spots to obtain representative statistical data.

4.4. Proposed Signal Processing Pipeline

The proposed processing pipeline comprises six parts. These are background subtraction, phase correction, time-domain transformation, footprint compensation, averaging and finally the $H\alpha A$ decomposition. The block diagram in Fig. 4.3 shows this processing pipeline schematically. The following sections describe each block in more detail.

4.4.1. Background Subtraction

A vector network analyser (VNA) measures S-parameters, which in the case of propagation measurements can be considered to be a ratio of a received electrical field over a transmitted electrical field. The received field can be decomposed due to the superposition principle in a contribution to the received electrical field by the sample and a contribution from the background. Therefore, the measured S-parameters can be written as shown in (4.8).

$$S_{measured} = \frac{E_{sample} + E_{background}}{E_{transmitted}} \tag{4.8}$$

By performing a measurement without any samples in the scene, the measured field is effectively purely the result of the background, which includes the response of the antenna and other static objects that may be present in the scene. In this way, only the ratio of $E_{background}$ and $E_{transmitted}$ is measured, which can be subtracted from measurements performed with samples present. This results in a removal of background effects and thus a clean S-parameter measurement of purely the surface-under-test. In Fig. 4.4, the result of this compensation procedure is shown. This figure shows the vertically polarised co-polar measurement results of a metal sphere placed at about 51 cm from the radar. The measurement results have been transformed from frequency domain, in which the S-parameters are naturally measured, to time domain so that a radar range profile is found. For more information on the time domain transformation, see section 4.4.3.

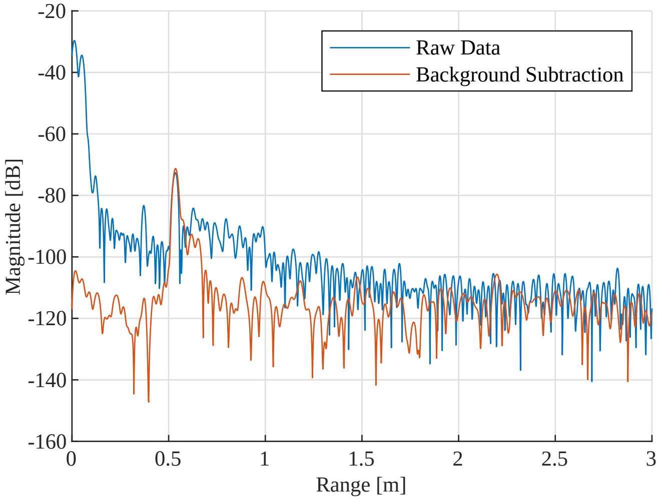

Figure 4.4: Comparison of time domain transformed measurement data before and after background subtraction. The target is in this case a metal sphere with a diameter of 3 cm and is located at a range of 0.51 m from the antenna.

During the lab measurements, the sample could be easily removed and thus the background could be measured very accurately. However, for outdoor measurements, the road surface is the actual sample which obviously could not be removed. Therefore, to still be able to compensate for the antenna influences in the measurement results, the antenna was pointed towards the sky and a background measurement was performed. By subtracting this background from the measurement result, the scattering effects induced from the antenna response are suppressed.

4.4.2. Phase Correction

For measurements to which the $H\alpha A$ decomposition is to be applied on, special attention must be paid to the phase measured in each polarimetric channel. Namely, if the horizontally and vertically polarised channels are not balanced in length, a range-dependent phase error occurs. This may lead to a target appearing to be at a different range in one polarimetric channel than in another. Also, an absolute offset in phase between the channels can be present due to e.g., the way an antenna is fed, which likewise can distort the measurement results and the resulting feature values.

Although the measurements in this chapter were performed using a symmetrical dual-polarised square horn antenna, the feeding network from the frequency extenders to the horn antenna is not exactly symmetrical and thus the phase of the measured scattering parameters needed to be corrected. Hence, a method to correct this phase difference was developed, based on measurements of a metal sphere.

A metal sphere approximates a point target and has the same radar cross section (RCS) for both horizontal and vertical co-polarised measurements due to its symmetry, while its cross-polar radar cross sections are 0 when the sphere is large compared to the wavelength. Therefore, a sphere with a diameter of 3 cm was chosen. Since the co-polar components of the sphere's RCS are equal, measurements of this reference target can be used to determine the phase offset of both horizontal and vertical channels, and can subsequently be used to compensate all four elements of the scattering matrix. These calibration measurements were performed before the start of each measurement session.

The first step in determining the phase offset is by applying time-domain gating to measurement data of the sphere [46]. This procedure filters out the contribution of scatterers other than the sphere that may be present in the scene, so that the sphere itself becomes the dominant target. As the sphere resembles a discrete target, the phase of the scattering parameters follows a linear decrease with frequency.

Subsequently, for each co-polarised channel, the phase is unwrapped and a function of form $\phi_{pp} = a_{pp} f + b_{pp}$ is fitted to the unwrapped phase where ϕ represents phase, f frequency and subscript p indicates the polarisation channel which can be H or V. Therefore, the parameter a corresponds to the phase gradient, which is dependent on the range to the target, while b corresponds to an absolute phase offset within the channel.

In order for each channel to detect the sphere at the same range, the phase gradients of both co-polar channels need to be equal. Therefore, the vertically polarised channel is chosen as the reference channel and the phase gradient of the horizontally polarised channel is corrected so that equality of phase gradients is achieved by considering the difference between the gradients. Subsequently, the b_{pp}-component of the phase compensation is selected such that for each channel, the phase is 0 degrees at 75 GHz after compensation. This compensation is shown in mathematical form in (4.9) for the horizontal co-polarised channel.

$$S_{HH,compensated} = S_{HH,measured} e^{j(a_{VV}-a_{HH})f+b_{HH}} \tag{4.9}$$

Due to the nature of the antenna setup used for these measurements, the cross-polar channels can be compensated as well. Namely, the electromagnetic radiation travels once through the V-polarised channel and once through the H-polarised channel. Therefore, the length of the cross-polar channels can be compensated using half of the compensation difference, as shown in (4.10). The VH channel can be compensated similarly by interchanging HV and VH.

$$S_{HV,compensated} = S_{HV,measured} e^{j\frac{(a_{VV}-a_{HH})}{2}f} \tag{4.10}$$

Fig. 4.5 shows the effect of the proposed phase correction procedure. It can be seen that the phase correction procedure shifts the peak resulting from the calibration target, so that in the HH-measurement this peak coincides with the peak in the VV-measurement.

4.4.3. Time-Domain Transformation

Since measurements are performed using a VNA, all S-parameter measurements are a function of frequency. To extract the range profile, they must be transformed to time domain. This can be done by means of Fourier transformation. If necessary, a window function can be used such as a Kaiser window. Furthermore, in this step the range profile can also be interpolated using zero-padding in frequency domain. In order to keep the distortion of the measured S-parameters minimal, no window function was used and no zero-padding was employed in the $H\alpha A$ decomposition procedure.

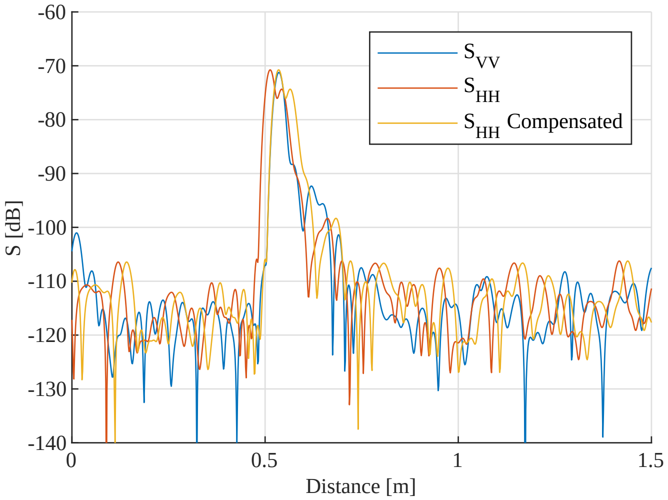

Figure 4.5: Comparison of time domain transformed measurement data before and after the proposed phase correction procedure on the HH channel. The observed target is a metal sphere with a diameter of 3 cm located at 0.51 m. Note that the double peak in the HH polarised channel is caused by a multipath reflection via the floor.

4.4.4. Footprint Compensation

The S-parameters from the time-domain transformed measurements cannot directly be used to compute the coherency matrix. Namely, unlike in airborne or spaceborne synthetic aperture radar applications, the observed cells are not located at a comparable distance from the radar. Due to the geometry of the automotive scenario, large differences in propagation distance exist between backscattered contributions originating from road surface areas close to the radar versus those from road surface further away. Therefore, the free space attenuation will cause great differences in the magnitude of the backscattered contributions, which needs to be compensated for. Moreover, in the automotive scenario, the observed cells also experience different observation angles as seen from the antenna, which leads to large differences in antenna gain for each observed range cell. This must be compensated as well. These two effects are apparent from the radar equation which is shown in (4.11):

$$P_{rx}\left(x,y\right) = \frac{G_{tx}\left(x,y\right)G_{rx}\left(x,y\right)\lambda^2 A\sigma_0\left(x,y\right)}{\left(4\pi\right)^3 R^4\left(x,y\right)} P_{tx}. \tag{4.11}$$

Here, P_{rx} is the received power from a surface cell and P_{tx} is the transmitted power. G_{tx} and G_{rx} are the gains of the transmitting and receiving antenna, respectively. R indicates the range to an observed surface patch, while A is the surface area of the observed surface patch with a normalised radar cross section σ_0. Lastly, (x, y) indicates the surface cell location dependency of the variables in the equation, and λ is the wavelength the radar operates at.

To accomplish correction of the two effects, the total power returned by each surface cell for a surface is computed using a numerical procedure described in [30]. This procedure works by discretising a flat surface in many small cells, each having a corresponding area A. Subsequently, the observation angles, ranges, and incidence angles for the centre points of these surface cells are calculated using the equations in [30]. By setting the normalised radar cross section σ_0 and the transmitted power P_{tx} to 1, the power returned from each cell can be found, thus revealing the footprint of the antenna. This leads to equation (4.12):

$$P_0\left(x,y\right)=\frac{G_{tx}\left(x,y\right)G_{rx}\left(x,y\right)\lambda^2 A}{\left(4\pi\right)^3 R^4\left(x,y\right)}. \tag{4.12}$$

Therefore, the normalised radar cross section of a surface with unknown σ_0 can be found as shown in (4.13):

$$\frac{P_{rx}\left(x,y\right)}{P_0\left(x,y\right)P_{tx}}=\sigma_0\left(x,y\right). \tag{4.13}$$

As the range profile is defined as the total power received from all targets within a specific range interval, also known as range bin, the range profile can be computed by summing the returned powers of each surface cell in the corresponding range bin. This procedure is mathematically shown in (4.14) where N is the number of range cells within a range interval l, with $P_{rx}\left(i\right)$ indicating the power returned by the i-th cell in the range interval.

$$P_{range}\left(l\right)=\sum_{i=1}^{N}P_0\left(i\right) \tag{4.14}$$

Since (4.14) is a linear operation, through its combination with (4.13), σ_0 can be found using (4.15) where P_{range} is the measured range profile by the radar, and $P_{range,0}$ is the ”normalised” range profile found by computing the range profile of (4.12).

$$\sigma_0\left(l\right)=\frac{P_{range}\left(l\right)}{P_{range,0}\left(l\right)P_{tx}} \tag{4.15}$$

Since S-parameters describe field strengths instead of power as the RCS does, the measured S-parameters can be compensated for the antenna footprint by dividing them by the square root of the ”normalised” range profile as shown in (4.16), where $S_{measured}$ are the measured S-parameters which can be found by dividing the received field by the square root of the transmitted power. Subsequently, the S-parameters can now be used to compute the coherency matrix and the $H\alpha A$ decomposition as described in section 4.2.

$$S_{compensated}\left(l\right)=\frac{S_{measured}\left(l\right)}{\sqrt{P_{range,0}\left(l\right)}} \tag{4.16}$$

4.4.5. Averaging

In synthetic aperture radar, the averaging for obtaining the coherency matrix is usually performed in the spatial domain, meaning that surrounding pixels in the obtained imagery are grouped together to compute statistics. This can be expressed as shown in (4.17):

$$\langle x\left(k,l\right)\rangle=\sum_{i=k-N}^{k+N}\sum_{j=l-M}^{l+M}\frac{x\left(i,j\right)}{\left(2N+1\right)\left(2M+1\right)}. \tag{4.17}$$

In this equation, $\langle x(k,l)\rangle$ is the average of a quantity x of the cell at location (k,l). The parameters N and M define the window size along the two dimensions of the image while $x(i,j)$ is the value of quantity x in the cell with index (i,j). In this equation, x could for example be the backscattered power from a cell, or, in the case of computing the coherency matrix, an element from the target vector multiplied by its conjugate self.

In the automotive scenario, this type of averaging is less suitable. Namely, this would mean that a range-interval of the range profile is used for the averaging, which is not necessarily valid as this will contain backscattering from road surfaces observed at different angles of incidence. This is especially true for surface backscattering located at relatively short range from the radar. As the incidence angle plays an important role in the scattering behaviour of the rough surface, the range-interval will not contain samples from the same statistical process, thus leading to invalid estimated statistical properties in the coherency matrix.

However, the automotive scenario provides an opportunity to perform the averaging differently. Instead of averaging over space, the averaging can be performed over time. Namely, modern automotive radars transmit many chirps per second, so that averaging can take place over each obtained range profile. In this way, every range bin corresponds to backscattering from road surface under the same angle of incidence. Also, since the vehicle is moving, a different part of the road surface is encompassed by the antenna beam footprint, thus leading to samples independent from each other taken from the same statistical process. Mathematically, this can be formulated as:

$$\langle x(l)\rangle = \sum_{i=1}^{N} \frac{x_i(l)}{N}. \tag{4.18}$$

In (4.18), $\langle x(l)\rangle$ indicates the average of a quantity x in range bin l and $x_i(l)$ indicates the value of the quantity x in range bin l at measurement time index i. N is the number of measurements used to perform the averaging.

4.4.6. HαA Decomposition

The last step is computing the features from the coherency matrix as shown in (4.2) in combination with the averaging explained in section 4.4.5. This can be done using (4.3) to (4.7). Subsequently, the features can be plotted in various formats and be fed to a classifier for automatic classification.

4.5. Experimental Results

This section presents the results of applying the proposed pipeline to measurements in the laboratory, as well as those from measurements that took place outdoors.

4.5.1. Lab Measurement Results

In Fig. 4.6 the mean value of the backscattered power from three different sandpaper samples in lab conditions is shown. It can be seen from this plot that there is clear distinction between the rough P24 type sandpaper and the smooth P60 and P100 sandpapers, while there does not seem to be a significant difference between the P60 and the P100 sandpaper. This is likely due to P60 type sandpaper already being too smooth to provide a significant

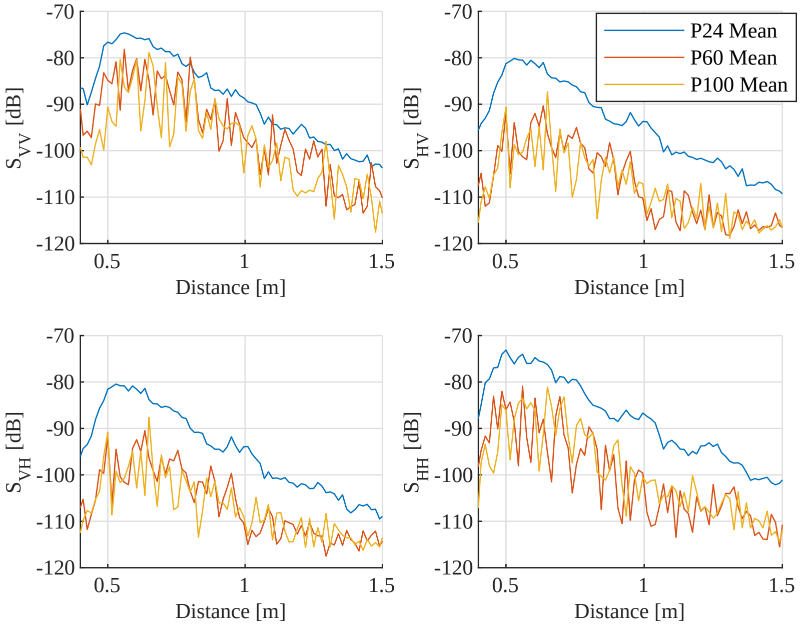

Figure 4.6: Mean of measured S-parameters for the different types of sandpaper (P24, P60, and P100 in order of decreasing roughness) measured in lab conditions.

backscattered contribution as the grain size in the sandpaper is relatively small compared to the wavelength. This is also the case for the P100 type sandpaper, leading to the observation that the backscattered radiation is caused by the sandpaper itself and/or the cavity that is formed between the backside of the sandpaper sample and the floor it was placed on.

Fig. 4.7 shows the results from the $H\alpha A$ decomposition, in particular the H and α features, graphed in the $H\alpha$-plane. In this plot, each symbol represents a range bin in the range of 0.5 to 1.5 metres. It can be seen that there is a clear difference between the P24 and the P100 type sandpapers. The P24 type shows a high entropy value whereas the P60 and P100 types show a broad spread but with centroids at lower values of entropy. The high entropy values indicate highly random scattering which is expected from a surface that differs electromagnetically from observation to observation. The lower entropy values of the smooth sandpaper types indicate less randomness in the scattering process. This can be explained by the grains of the sandpaper being too small compared to the wavelength. Therefore, from an electromagnetic point of few, a sheet of smooth sandpaper substrate material is measured, which is more or less the same from measurement to measurement. Fig. 4.6 reinforces this observation as it shows that the P60 and P100 types are indistinguishable from each other, thus also indicating that the grains on both sandpapers have become too small compared to the wavelength to contribute significantly to the backscattered power.

The unique geometry of the automotive scenario also allows for considering the H and α features as function of range. The difference in range is related to the effective angle of

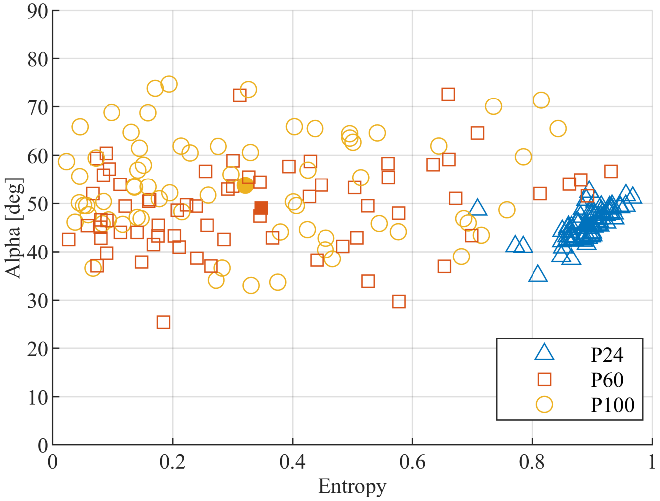

Figure 4.7: The H and α features of the sandpaper measurements performed in the lab in the range interval from 0.5 to 1.5 metres. The solid coloured symbols indicate the clusters' centroids formed by the corresponding sandpaper types.

incidence at the surface, where surface area close to the radar experiences a low angle of incidence (steep), whereas surface areas farther away experience a high angle of incidence (shallow). A plot of the variation of angle of incidence as function of range is shown in Fig 4.8.

As the angle of incidence can influence scattering properties, this can further help with distinguishing different classes of surface. Fig. 4.9 shows the entropy as function of range. It can be seen that for the P24 type sandpaper, the entropy stays relatively constant as function of range, indicating that the same scattering mechanism is at play, independent of angle of incidence. However, for the P60 and P100 type, the entropy tends to increase as range increases, moving more towards entropy values as those seen for the P24 measurements. This can be explained by more specular reflection starting to occur, leading to less backscattered power, in combination with the limited sensitivity of the VNA. Due to measured S-parameters being close to the noise floor as seen from Fig. 4.6, thermal noise takes over which results in high entropy values due to its random nature.

Finally, the anisotropy feature can be considered. The entropy versus anisotropy plot is shown in Fig. 4.10 for all ranges in the 0.5 to 1 meter interval. Here, a very clear distinction between the P24 and the other types of sandpaper can be seen, leading to the conclusion that the anisotropy is also useful for classification purposes in this case.

4.5.2. Outdoors Measurements Results

As seen from the lab measurements, rough surfaces can indeed be distinguished from smooth surfaces using the proposed pipeline. To evaluate if this method is also effective for actual road surfaces under various weather conditions, measurements on real road surfaces were performed. Fig. 4.11 shows the returned power after the averaging step, thus representing the normalised radar cross section of the surface. This measurement shows that for wet

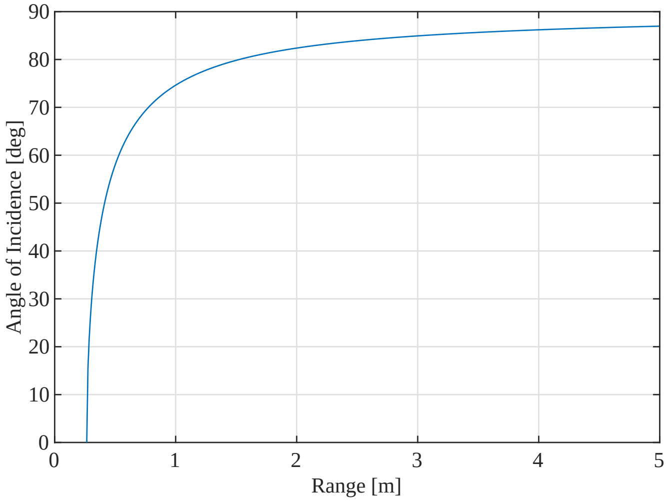

Figure 4.8: The local angle of incidence at a point on the surface at a range indicated by the x-axis for an antenna height of 26.5 cm.

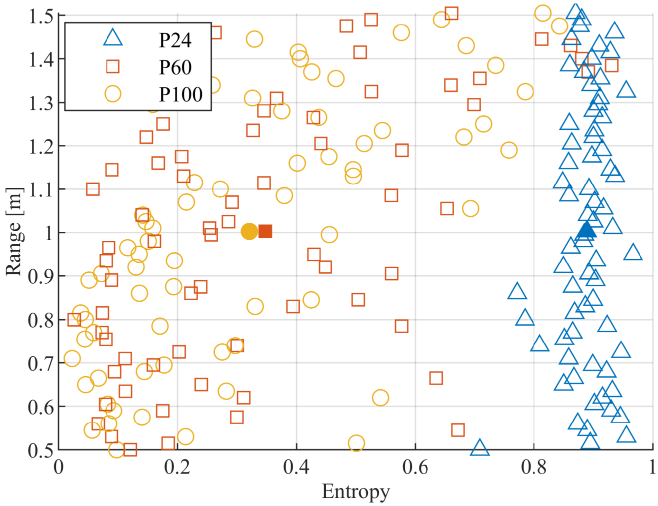

Figure 4.9: The entropy feature of the different sandpaper types versus range, extracted from the experimental measurements. The solid symbols indicate the centroids of the clusters formed by each type of sandpaper.

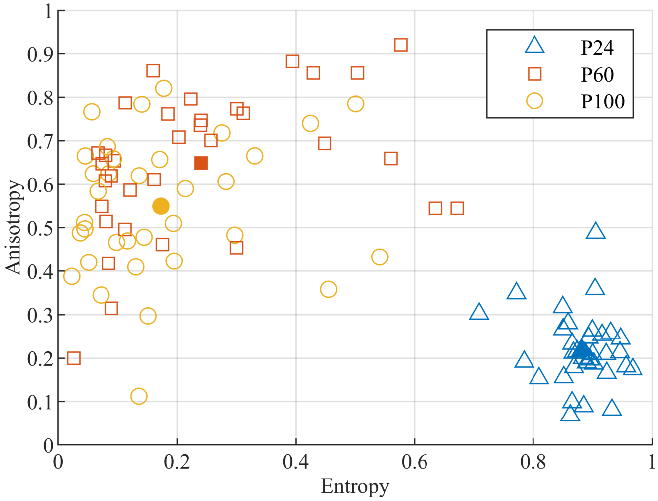

Figure 4.10: The H and A features of the different sand paper types measured in a range interval from 0.5 to 1 metre. The solid symbols indicate the centroids of the clusters formed by each type of sandpaper.

surfaces, the σ_{VV} is generally larger than σ_{HH}. However, as the roughness increases, σ_{HH} and σ_{VV} tend to become more equal, thus indicating depolarisation by a more diffusive scattering process due to the increased surface roughness as expected from theory.

Furthermore, the $H\alpha$-plane for all three road surface conditions (i.e., dry asphalt, wet asphalt, and asphalt covered in gravel) for a 60° orientation angle is shown in Fig. 4.12a. It can be seen that there is a clear difference in the H and α features when comparing wet and dry road surface conditions. There also exists a small difference between road surface covered with basalt versus the regular road surface, however it is not as pronounced as with the road surface under wet conditions.

However, when taking the anisotropy in account as shown in Fig. 4.12b, it can be seen that the separation between the basalt and the dry asphalt becomes larger, making it easier to separate these road surface conditions from each other.

Finally, the entropy, anisotropy and α, can be considered as function of range. Fig. 4.13 shows the entropy as function of range. This figure shows that there is not much variation present in the entropy of regular asphalt and asphalt covered with basalt gravel, but that a range dependency is present for wet asphalt. This could be exploited by for example considering the H-values from 1.2 metres onward, resulting in more pronounced separation of the clusters of wet and dry conditions in the $H\alpha$-plane.

To quantify the loss in separation between the clusters, the euclidean distances between the centroids of the clusters is considered. The α feature was divided by 90° to ensure all features are within the same limits of 0 and 1. Furthermore, the standard deviations of all three features were computed as an indication of the spread of the clusters in the $H\alpha A$ space. Table 4.1 lists the results of this with on the left hand side the distances between the clusters' centroids and on the right hand side the standard deviations of the three features.

Subsequently, the measurement results for an orientation angle of 90° can be considered.

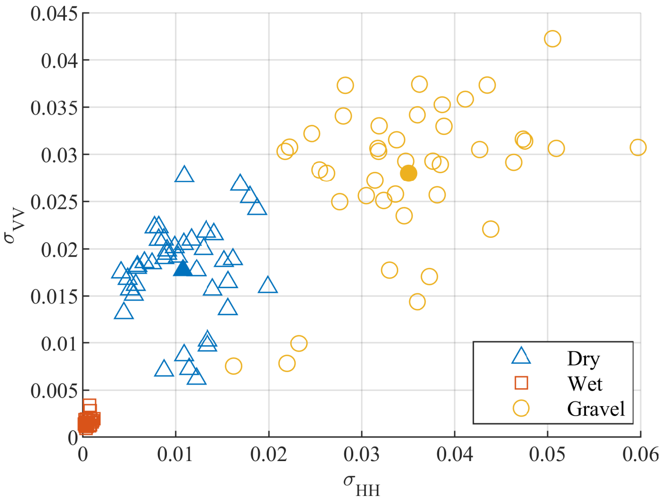

Figure 4.11: Normalised radar cross sections in linear terms of the considered road surface conditions measured with a 60° orientation angle, in the range interval from 0.5 to 1.1 m.

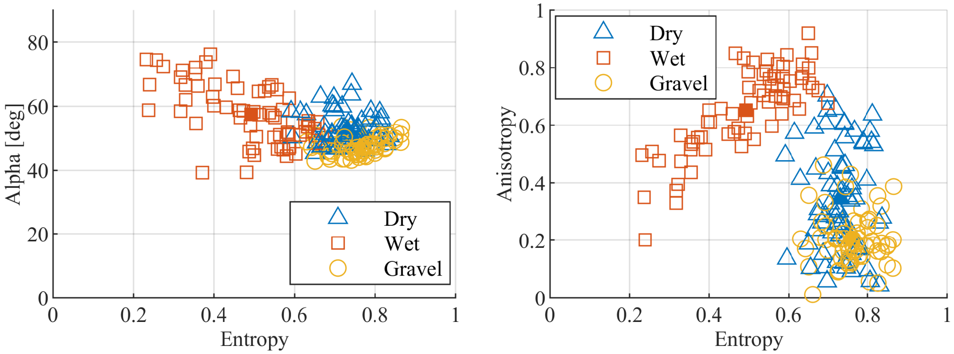

(a) (b)

Figure 4.12: The α (a) and A (b) features of the measurements performed outdoors plotted versus the H feature in the range interval from 0.5 to 1.5 metres with an orientation angle of 60°. Here, the considered three surfaces are ordinary dry asphalt, wet asphalt, and asphalt covered by basalt stone gravel. The solidly coloured symbols indicate the centroids of the clusters formed by the measurements of the corresponding road surface conditions.

Table 4.1: Euclidean distance between the centroids and standard deviations of the clusters formed by the H, α and A features of dry asphalt, wet asphalt and asphalt covered with gravel, measured in a range interval of 0.5 to 1.5 metres with an antenna orientation angle of 60°.

Dry	Wet	Gravel		$\sigma\ H$	$\sigma\ \alpha$	$\sigma\ A$
0	0.39	0.15	Dry	0.054	0.053	0.179
	0	0.53	Wet	0.123	0.102	0.145
		0	Gravel	0.058	0.030	0.089

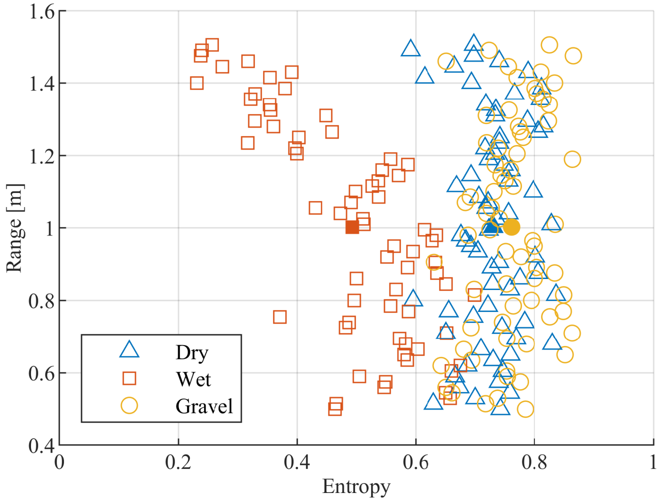

Figure 4.13: The entropy versus range for the considered road surface conditions (i.e., asphalt which is dry, wet, and covered with basalt gravel), for an orientation angle of 60°. The solidly coloured symbols indicate the centroids of the clusters formed by the measurements of the corresponding road surface conditions.

In Fig. 4.14a it can be seen that the entropy varies with range for all three different road surface conditions. When considering all range bins from 0.5 to 1.5 metres in the $H\alpha$-plane, this would result in potential overlap of the clusters of the different classes. However, when considering only measurements from 0.9 metres onward, the separation of the clusters is better. The results of this can be seen in Fig. 4.15 where only a selected spatial subset of the samples is used to form the plot with H and α features. A good separation of the clusters for the different surface conditions can be seen.

Finally, it is instructive to consider the anisotropy features obtained from the measurements as function of range. It can be seen in Fig. 4.14b that the anisotropy does vary with range, but that it is more or less similar for each class. Therefore, for the set of measurements performed with an antenna orientation angle of 90°, the anisotropy is a less valuable feature compared with the results obtained at 60°.

Table 4.2 shows the distances between the centroids of the clusters, and the standard deviations of the road surface H, α and A features performed with a measurement angle of 90°. It can be seen that compared to the results measured with an orientation angle of 60° in table 4.1, the distance between centroids has decreased, except for the distance between gravel and dry asphalt. Also, for the gravel, the spread of the cluster increased. However, for the other classes the spread remains similar except for the entropy spread of dry asphalt.

To evaluate the results from the proposed pipeline, they are compared to results obtained using co- and cross-polarisation ratios as proposed in [28]. The used features are in this case σ_{VV}/σ_{HH}, σ_{VH}/σ_{HH} and σ_{HV}/σ_{HH}. To compare the clusters formed by these features to those of the proposed pipeline, the polarisation ratios were normalised with the maximum value from all classes, so that all values are limited between 0 and 1 as would be done in a machine learning classifier. As these features are ratios of polarisation measurements, they are sensitive to noise. Namely, when σ_{HH} is small, noise may impact the ratios substantially

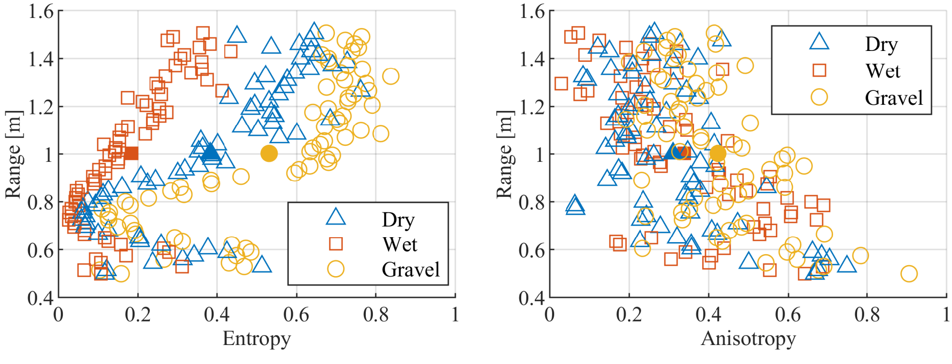

(a)

(b)

Figure 4.14: Entropy (a) and anisotropy (b) versus range of the outdoor measurements performed with an orientation angle of 90°. The solidly coloured symbols indicate the centroids of the clusters formed by the measurements of the corresponding road surface conditions.

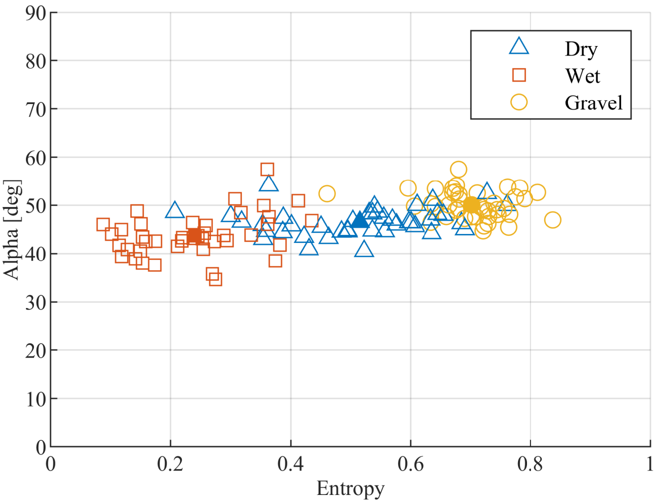

Figure 4.15: The H and α features of the outdoor measurements in the range interval from 0.9 to 1.5 metres with an antenna orientation angle of 90°. The solidly coloured symbols indicate the centroids of the clusters formed by the measurements of the corresponding road surface conditions.

Table 4.2: Euclidean distance between the centroids and standard deviations of the clusters formed by the H, α and A features of dry asphalt, wet asphalt and asphalt covered with gravel, measured in a range interval of 0.9 to 1.5 metres with an antenna orientation angle of 90°.

Dry	Wet	Gravel		$\sigma\ H$	$\sigma\ \alpha$	$\sigma\ A$
0	0.28	0.23	Dry	0.126	0.031	0.095
	0	0.49	Wet	0.095	0.049	0.114
		0	Gravel	0.067	0.032	0.114

Table 4.3: Euclidean distance between the centroids and standard deviations of the clusters formed by the co- and cross-polar ratios of dry asphalt, wet asphalt and asphalt covered with gravel, measured in a range interval of 0.9 to 1.5 metres with an antenna orientation angle of 90°.

Dry	Wet	Gravel		$\sigma\ \frac{\sigma_{VV}}{\sigma_{HH}}$	$\sigma\ \frac{\sigma_{HV}}{\sigma_{HH}}$	$\sigma\ \frac{\sigma_{VH}}{\sigma_{HH}}$
0	0.25	0.07	Dry	0.036	0.048	0.037
	0	0.32	Wet	0.197	0.187	0.200
		0	Gravel	0.008	0.027	0.021

and cause them to explode in value. To avoid this from occurring, only the range interval from 0.9 to 1.5 metres, which lies within the -10 dB antenna footprint, is considered. Subsequently, the same metrics are computed as for the H, α and A features and are listed in table 4.3. Comparing these tables with each other, it can be seen that the distances between centroids is larger in all cases when using the proposed pipeline. Furthermore, the observation can be made that the clusters are smaller when using the ratio features for the dry and gravel classes, but the opposite is true for the wet asphalt class. Even though the dry and gravel classes have smaller standard deviations, this benefit is neglected as the centroids of these clusters are very close together. This suggests that the proposed pipeline is a robust alternative to classification based on simpler polarimetric ratios, as polarimetric ratios suffer from noise sensitivity and the normalisation usually performed for machine learning classifiers, which causes the clusters to be compressed close to the origin in presence of outliers.

4.5.3. Polarisation Analysis

For the measurements previously presented, all four polarimetric channels were used. However, to reduce complexity and costs of an automotive radar system to be mass-produced, it may be advantageous to only partially measure the polarimetric response. To this extent, the results from the $H\alpha A$ decomposition are re-evaluated with the difference that the cross-polar channels are zeroed out. These channels can potentially be omitted as they contain less power than the co-polar channels as can be seen in Fig. 4.6.

The first observation that can be made on the effects of omitting the cross-polar channels is that this reduces the rank of the coherency matrix to two, as can be seen from (4.1) and (4.2). This in turn results in the coherency matrix only having two non-zero eigenvalues at maximum. Therefore, the anisotropy will be 1 as can be seen from (4.7), and thus will not contribute to separating road surface conditions.

Fig. 4.16 shows the effect of zeroing out the cross-polar channel on the positioning of surface reflections in the $H\alpha$-plane. When comparing this plot to that of Fig. 4.12a, it can be seen that the wet road surface is still separated from the dry classes, but that this separation has decreased. Similarly, with measurements performed with an antenna orientation angle of 90°, the separation between different road surface conditions also decreases. This can be seen by comparing Figs. 4.14a and 4.17.

To quantify the loss in separation between the clusters for the measurements performed with an orientation angle of 60°, again the euclidean distances between the centroids and the standard deviation of the clusters are considered. Comparing table 4.1 and table 4.4 shows that the distances have decreased significantly, ranging from 59% to 78%. A similar comparison is shown for the measurements performed with an orientation angle of 90° in tables

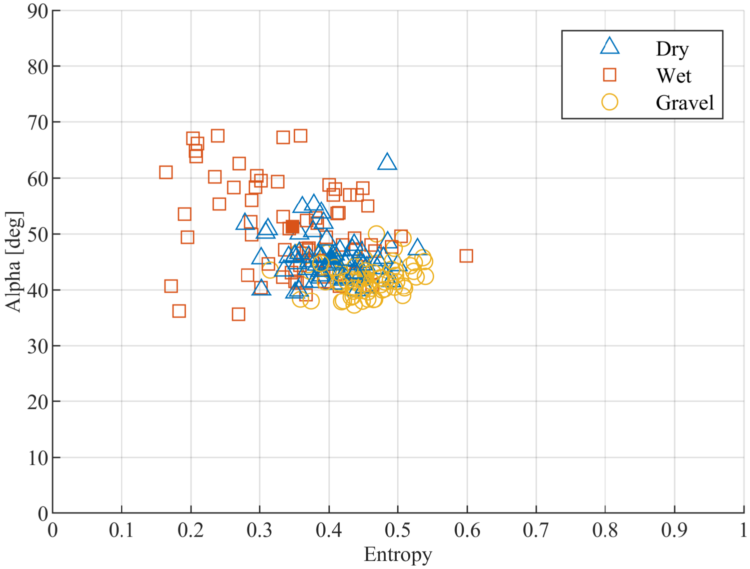

Figure 4.16: The H and α features of the measurements performed outdoors in the range interval from 0.5 to 1.5 metres with an orientation angle of 60° with cross polar components zeroed out.

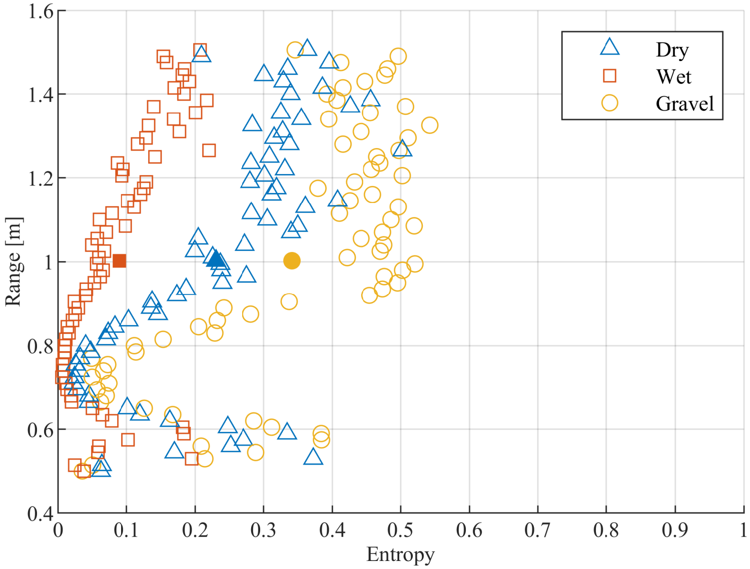

Figure 4.17: The entropy versus range of the measurements performed outdoors with an orientation angle of 90° with cross polar components zeroed out.

Table 4.4: Euclidean distance between the centroids and standard deviations of the clusters formed by the H, α and A features, computed with cross-polar components zeroed out, of dry asphalt, wet asphalt and asphalt covered with gravel, measured in a range interval of 0.5 to 1.5 metres with an antenna orientation angle of 60°.

Dry	Wet	Gravel		$\sigma\ H$	$\sigma\ \alpha$	$\sigma\ A$
0	0.08	0.06	Dry	0.052	0.045	0
	0	0.15	Wet	0.092	0.093	0
		0	Gravel	0.049	0.032	0

Table 4.5: Euclidean distance between the centroids and standard deviations of the clusters formed by the H, α and A features, computed with cross-polar components zeroed out, of dry asphalt, wet asphalt and asphalt covered with gravel, measured in a range interval of 0.9 to 1.5 metres with an antenna orientation angle of 90°.

Dry	Wet	Gravel		$\sigma\ H$	$\sigma\ \alpha$	$\sigma\ A$
0	0.19	0.15	Dry	0.076	0.033	0
	0	0.34	Wet	0.056	0.053	0
		0	Gravel	0.047	0.037	0

4.2 and 4.5. Here, reductions of 30% to 34% can be seen. Thus, from these observations, it becomes clear that a radar system could be designed in such a way that the cross-polar channels are not measured at a cost of less separation between the clusters of several classes of road surface conditions. As the separation decreases, classification accuracy may see a reduction as well which leads to a trade-off between radar system complexity/costs and performance.

4.6. Convergence of H/α/A-features

In this section, the convergence of the measured scattering parameters is considered. To do this, the difference between a statistical quantity Q, denoted by ΔQ, calculated based on N measurements, indicated by $Q\left(N\right)$, and the same statistical quantity Q based on $N-1$ measurements, denoted by $Q\left(N-1\right)$, is computed as shown in (4.19). The statistical quantity Q can for example be the mean value of the magnitude of S_{VV}, denoted by $\langle|S_{VV}|\rangle$, or the covariance of $|S_{VV}|$ and $|S_{HH}|$.

$$\Delta Q\left(N\right) = Q\left(N\right) - Q\left(N-1\right) \tag{4.19}$$

Furthermore, ΔQ can be normalised to make the comparison of multiple statistical quantities possible, e.g. $\langle|S_{11}|\rangle$ & $\langle|S_{22}|\rangle$.

Fig. 4.18 shows the trend of the convergence of the mean value of the measured scattering parameters of dry asphalt measured with an antenna orientation angle of 60°. The difference is normalised by the largest computed difference within the corresponding range bin. As expected, it can be seen that the computed mean value converges with the normalised difference going to zero as the measurements are uncorrelated. It can also be seen that including more and more measurements leads to diminishing returns due to incoherent summing and division by the number of measurements. Another important observation is that the difference does not reduce gradually, but sometimes experiences a peak within a range bin. This can be explained by a measurement that has a particularly high or low value

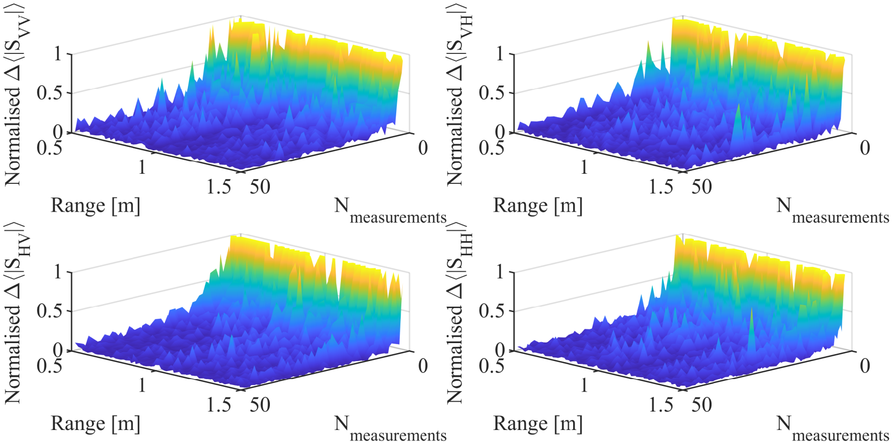

Figure 4.18: Convergence of the mean value of the measured scattering parameters of dry asphalt, measured with an antenna orientation angle of 60° as function of range and number of included surface measurements.

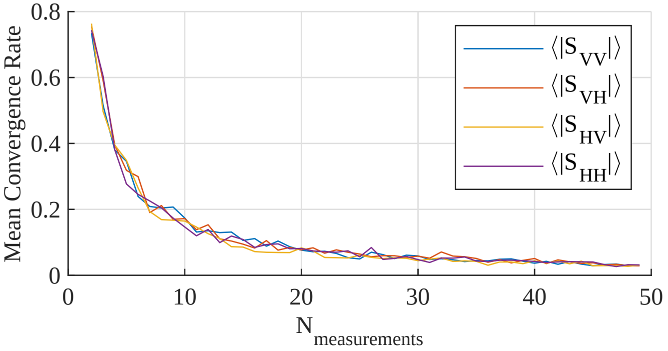

Figure 4.19: Mean convergence rate of the mean values of the measured scattering parameters of dry asphalt, measured with an antenna orientation angle of 60°.

compared to previous measurements. The mean convergence rate, C, is then computed, which is the mean value taken over the range bins for a number of included measurements N as shown in (4.20).

$$C\left(N\right)=\sum_{i=1}^{M}\frac{\overline{\Delta Q_{i}}\left(N\right)}{M} \tag{4.20}$$

Here, M indicates the number of range bins over which the mean is computed and $\overline{\Delta Q_{i}}\left(N\right)$ is the normalised difference of the statistical quantity ΔQ in the range bin i, computed from N measurements.

Fig. 4.19 shows the mean convergence rate for the mean values of the measured scattering parameters of dry asphalt, measured with an antenna orientation angle of 60°. All scattering parameters converge on average at the same rate. Furthermore, this figure can be used to determine the number of measurements that must be taken to achieve a difference in the computed $\langle|S|\rangle$ that is on average less than a specified threshold. For example, to

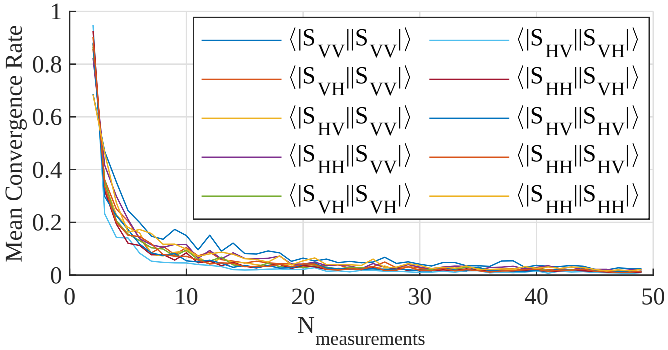

Figure 4.20: Mean convergence rate of the covariances of the measured scattering parameters of dry asphalt, measured with an orientation angle of 60°.

achieve a mean difference of less than 10% compared to the previous N measurements, at least 19 measurements need to be performed.

A similar analysis can be performed for the covariance of the 4 scattering parameters in Fig. 4.20. Compared to the mean values, these values converge faster. To achieve a mean difference of less than 10%, 15 measurements are required.

Next, the convergence of the H, α and A features is considered, introduced for road surface classification in [2]. Figs. 4.21 to 4.23 show the mean convergence rates of these features for dry asphalt, wet asphalt and asphalt covered with gravel, all measured with an antenna orientation angle of 60°. From these figures, it can be seen that overall, the anisotropy feature is the slowest to converge. This can be caused by the coherency matrix having a low eigenvalue which is sensitive to noise and thus more measurements are required to average out its effect. Also, for wet asphalt, the mean convergence rate shows sharper deviations from the general decreasing behaviour. This can be explained by the measured scattering parameters of this class being closer to the noise floor of the VNA, and thus being more influenced by noise.

It can be seen that about 36 measurements are required to achieve mean convergence rates below 0.1 for the wet asphalt condition. When an occasional mean convergence rate slightly above 0.1 is acceptable, 25 measurements may suffice.

Similarly, for the case of the measurements that were performed with a 90° orientation angle, the mean convergence rate of the H, α and A features can be considered. Figs. 4.21 to 4.23 show that these converge at a similar rate as the feature values measured with an orientation angle of 60°. Thus, in general, a similar number of measurements as with the 60° orientation angle is required to achieve a specified mean convergence rate.

4.6.1. Discussion on the relevance of convergence

The analysis of the convergence is important as it is related to the number of measurements of road surface scattering needed for an accurate classification. This has two implications. First, the measurement time with the resulting distance that is covered by a vehicle. If e.g., the measurement time of the radar system is 50 µs and 50 measurements are required to achieve the required level of convergence, then the total time to classify a surface condition

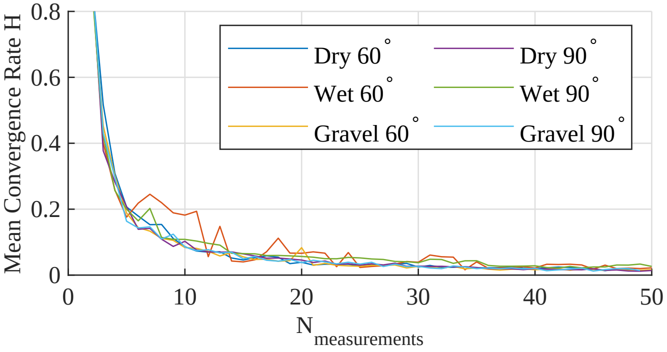

Figure 4.21: Mean convergence rate of the entropy H feature of dry asphalt, measured with antenna orientation angles of 60° and 90°.

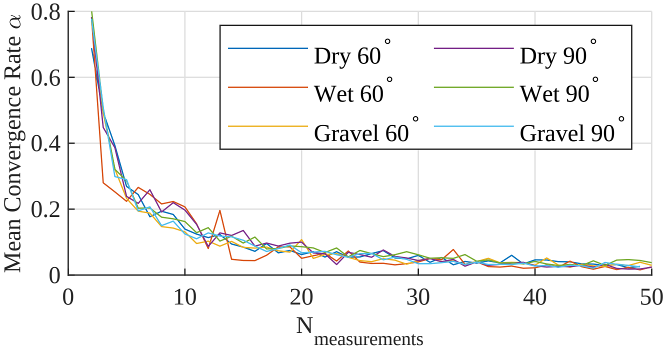

Figure 4.22: Mean convergence rate of the α feature of dry asphalt, measured with antenna orientation angles of 60° and 90°.

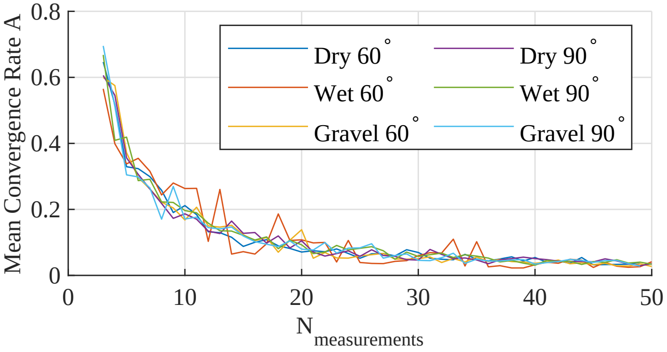

Figure 4.23: Mean convergence rate of the anisotropy A feature of dry asphalt, measured with antenna orientation angles of 60° and 90°.

is 2.5 ms. If a car is moving at 100 km/h (27.8 m/s), the distance travelled during the measurement time is about 6.9 cm. Depending on the measurement time and the amount of required measurements, the distance travelled by the car during the measurement period may become significant enough to reduce the effectiveness of the road condition estimation.

The second implication is related to the requirement that each road surface measurement should be uncorrelated with the previous one. This means that each surface measurement should be spaced one or more correlation lengths from the previous sample. For example, when the longest correlation length of a road surface condition is 5 mm, then the total distance that needs to be covered is 25 cm in the case of 50 required measurements. This means that a puddle of water or a patch of ice or other road surface condition needs to be at least 25 cm in length.

These two cases show that it is important to analyse the convergence of the H, α and A features, as it determines the distance a car travels during a road surface classification measurement and the length of surface that needs to be covered to achieve accurate results. Namely, by reducing the number of required measurements as much as possible, the refresh rate of the surface classification system can be increased, while the distance travelled by the vehicle and the required road surface condition size can be minimised.

4.7. Conclusion

In this chapter, a novel processing pipeline incorporating the $H\alpha A$ decomposition for road surface condition identification in automotive scenarios has been proposed. An introduction to the $H\alpha A$ decomposition was presented to define the three features. Afterwards, the proposed pipeline was introduced, outlining a number of necessary steps to apply the decomposition in the context of automotive radar, such as the antenna footprint correction and the temporal averaging for the computation of the $H\alpha A$ polarimetric features.

Experimental measurements have been performed both in lab conditions on three different types of sandpaper (P24, P60 and P100) as well as outdoors on real road surfaces under various conditions. From the lab measurement results it could be seen that it is possible to distinguish rough and smooth sandpaper using the H, α and A features. The rough sandpaper resulted in a dense cluster in the $H\alpha$-plane with a high entropy value while the smooth sandpapers showed on average a lower entropy value. Also, the smooth and rough sandpaper measurements were found to differ significantly in anisotropy: the rough sandpaper presented a low anisotropy while the smooth sandpapers showed a medium-high anisotropy.

The outdoor measurements were performed on three different road surface conditions, namely regular dry asphalt, wet asphalt and asphalt covered by basalt gravel. All three road surface conditions were measured using antenna orientation angles of 60° and 90°. For both orientation angles, a clear difference exists between the wet and dry asphalt classes when considering the H and α features. To further differentiate the dry asphalt from the asphalt covered with gravel in the 60° case, the anisotropy feature can be used. For the 90° orientation angle, the three road surface conditions can be distinguished in the $H\alpha$-plane. However, the anisotropy shows the same behaviour for all three classes.

The results of the proposed signal processing pipeline have been compared to classification based on features proposed in the literature, such as simple polarimetric ratios. This comparison shows that a larger separation of the clusters of samples from different road conditions could be achieved using the proposed pipeline.

Also, a polarimetric analysis was performed in which the importance of taking the cross-polar channels into consideration was evaluated by assessing the results when the cross-polar channel is zeroed out. Firstly, it was shown that the anisotropy feature can no longer be used in this case. Secondly, even if some separation between clusters was still observable, the cost of neglecting the cross-polar channels was found to be less separation of the different classes in the H, α and A features. Namely, a reduction in cluster centroid separation of up to 78% for the measurements performed with an antenna orientation angle of 60° was observed, while a reduction of up to 34% was found for the 90° measurements. This likely leads to a decrease in classification accuracy. However, by not considering the cross-polar components, the radar systems can be reduced in complexity and costs.

Furthermore, the convergence of the polarimetric decomposition for radar-based road surface measurements was investigated. It is crucial to investigate the convergence of the measured statistical quantities as it places bounds on the accuracy of the computed statistics as the required level of convergence determines also the number of measurements that need to be practically acquired. This in turn influences the refresh rate of a road surface classification system and determines the amount of surface area that must be covered by the platform in the process.

To provide insights in the convergence of S-parameters and polarimetric H, α and A features, mean convergence rates of the mean and covariance of the S-parameters were computed, as well as the mean convergence rates of the H, α and A features. It was found that the covariances of the S-parameters converge faster than their mean values, and out of the three considered features, the entropy feature is the fastest to converge.

Finally, it was shown that the features of the three road surface classes converge at the same rate, independent of the antenna orientation angle they were measured with, or the road surface condition they were calculated for.

5

Vulnerable Road User Recognition using MIMO Polarimetric Radar

Besides estimating road surface conditions, polarimetric automotive radar can be used to enhance classification accuracy of other targets as well. A particular important group of targets are the so-called Vulnerable Road Users (VRUs). This group represents road users such as pedestrians and cyclists. In this chapter, polarimetric properties of VRUs are investigated using a custom-made innovative polarimetric MIMO automotive radar system developed in collaboration with Huber+Suhner, with a corresponding newly developed signal processing pipeline to accomplish this task. The processed data are subsequently used to analyse the polarimetric properties of the measured targets and two classification methods for VRUs are proposed. From the results achieved by these classifiers, it is shown that polarimetric radar is able to increase classification performance.

Parts of this chapter have been published as:

W. Bouwmeester, F. Fioranelli, and A. Yarovoy, "Classification of Dynamic Vulnerable Road Users Using a Polarimetric mm-Wave MIMO Radar", under review for *IEEE Transactions on Radar Systems*, 2024.

5.1. Introduction

In recent years, increasingly more vehicles are equipped with 77 GHz automotive radar to enable advanced driving assistance systems such as adaptive cruise control, but also to enhance road safety. The increased integration of these radar systems in vehicles has the potential to also benefit other road users besides the driver of the vehicle itself. Specifically, this is true for vulnerable road users (VRUs), which typically include pedestrians and cyclists. They are particularly vulnerable when involved in accidents as they do not have any protective structures or devices that help dissipating the force of impact, which cars, in contrast, are equipped with. Because of their vulnerability in combination with, amongst others, the ever increasing safety requirements on cars, in the Netherlands most fatal traffic victims are currently cyclists, having overtaken car occupants in recent years [47].

Because of this vulnerability of cyclists, pedestrians, and other VRUs, many research efforts concerned with using automotive radar to detect and classify vulnerable road users have been undertaken in recent years. For example, in [48–50] deep learning methods are employed. In [48] and [49] time-frequency, i.e., micro-Doppler signatures, are used for this, while [50] uses a single range-Doppler frame. Using a convolutional network, a classification accuracy of 84.2% was achieved on unseen data in [50], while the convolutional neural network presented in [49] achieved classification accuracy values greater than 92.4%. In [51], classification of vulnerable road users is performed using autocorrelation features in the time-frequency domain. It is found that the features of correlation length & time show high potential for classification of pedestrians and cyclists. In [52], pedestrian classification is performed using image features which are extracted from range-Doppler maps. Combining this with tracking algorithms, resulted in a success rate of 88%, using a sensing signal bandwidth of 1.6 GHz.

Similar to the automotive radar systems that are currently available, the radar used in the aforementioned research employed single-polarised sensing waves. These systems are unable to measure the polarisation state of the waves backscattered from the environment and targets, which may contain useful information for classification purposes. For example, the spokes of a bicycle wheel could be sensitive to one type of polarisation, while relatively insensitive to another due to their inherent vertical structure. Thus, to exploit the information available in the polarisation state, polarimetric radar systems are required. However, currently, there are no commercially available automotive radar systems on the market, and only recently fully polarimetric automotive radar prototypes and proof-of-concepts have been developed for research purposes [53–58]. In [53] and [54] two antenna concepts for polarimetric automotive radar are presented, while [55–57] propose three fully integrated radar systems. In [58], an instrumentation radar is presented to study scattering behaviour from VRUs at frequencies within the automotive radar band.

Even though the use of polarimetry in automotive radar is quite novel and literature on the topic is relatively limited, a few studies have already been undertaken to study the polarimetric response of VRUs at 77 GHz. In [59] and [60], several polarimetric representations of targets have been investigated for the purpose of VRU classification using a modified version of the approach presented in [61]. Using different polarimetric features in point cloud format, it is found that a significant improvement in VRU classification can be achieved over exclusively using non-polarimetric features. This is extended further in [62], where detection of road users is performed on pre-detector data, showing further improvements in classification performance. In both works, classification is performed predominantly in the angular domain and only the strongest Doppler measurements corresponding to targets are kept. The radar system used in these works was also employed to investigate the benefits of polarimetric information for localisation purposes [63]. In [64], static polarimetric measurements of four different types of bicycles were carried out at various azimuth angles. Here, it is also concluded from the results that polarimetric information could potentially help improve vehicle classification. In [65], static measurements of a number of vehicles as well as a motorcycle, bicycle, and pedestrian were performed and it is found that significant differences in polarimetric returns can occur depending on target orientation. In [66], a classifier based on a Convolutional Neural Network is used to classify static canonical targets (dihedrals and boxes) in various orientations, and classification accuracy over 90% is obtained. In [58], partially polarimetric measurements of moving VRUs such as pedestrians, a bicycle, and a dog are presented. It was found that the range-Doppler signatures presented a number of unique velocity-dependent features that potentially could be used for classification.

However, to the best of the authors' knowledge, in none of the aforementioned research the impact of the dynamic behaviour of VRUs (e.g., moving arms/legs with related Doppler signature) on their polarimetric response and its use for classification purposes is extensively considered. In this chapter, this gap is addressed by further studying the polarisation of the returns from cyclists, pedestrians, motorcyclists, and a vehicle while they are moving. To achieve this, a custom-designed novel polarimetric MIMO automotive radar system was developed in collaboration with Huber+Suhner AG (H+S) to collect measurement data from these classes of targets while they were moving in various direction with respect to the radar. The collected measurement data is subsequently processed and analysed using a new polarimetric automotive radar signal processing pipeline. From these data, it is found that polarimetric signatures of VRUs differ significantly from each other and that the polarimetric composition of their returns changes over time. Moreover, the polarimetric ratios of the considered classes of targets form clusters, indicating that the polarisation state of their returns may contain useful information for classification. It is also shown that the range-velocity signatures of pedestrians & cyclists contain some polarimetric structure, which could potentially be exploited by machine learning algorithms to improve classification.

The rest of this chapter is organised as follows: section 5.2 introduces the signal processing required to process data from time division multiplexing (TDM) MIMO polarimetric radar systems. Section 5.3 introduces the polarimetric radar system including a new calibration method based on a radar target simulator, as well as the measurement procedure. Section 5.4 describes the post-processing procedures applied to the experimental measurement data while section 5.5 details the obtained results. The chapter closes with conclusions presented in section 5.6.

5.2. Polarimetric MIMO Radar Signal Processing

In this section, the processing of the received waveforms of a polarimetric MIMO frequency modulated continuous wave (FMCW) radar with TDM is considered. Firstly, the processing of the individual polarimetric channels is discussed, and subsequently coherent processing of all virtual channels is considered to enhance the angular resolution.

5.2.1. Single Polarimetric Channel Processing

In contrast to single-polarised radar, polarimetric radar systems also aim to estimate the scattering parameters of a target. The scattering matrix describes the relation between the polarisation and amplitude of the electric fields, indicated by E, of an incident sensing wave impinging on a target and the wave scattered back by that target, as shown in equation (5.1):

$$\begin{bmatrix} E_x^s \\ E_y^s \end{bmatrix} = \begin{bmatrix} S_{xx} & S_{xy} \\ S_{yx} & S_{yy} \end{bmatrix} \begin{bmatrix} E_x^{inc} \\ E_y^{inc} \end{bmatrix}. \tag{5.1}$$

Here, the superscript s indicates the scattered components of the wave while the superscript inc indicates the incident wave. The subscripts x & y indicate the polarisation basis, for example a horizontal/vertical or left/right-hand circular basis.

Subsequently, the relationship between the incident sensing wave and the scattered wave can be used to formulate the signal model of the data collected by a polarimetric FMCW radar system. The waveform transmitted corresponding to the i-th virtual channel as a function of time t by a FMCW radar is shown in (5.2), as:

$$\begin{aligned} s_i^{tx}\left(t\right) &= e^{j2\pi \int \left(f_{start} + f_{slope} t\right)\, dt} \\ &= e^{2\pi j \left(f_{start} + \frac{1}{2} f_{slope} t\right) t} \end{aligned}. \tag{5.2}$$

where f_{start} is the frequency at which the chirp signal starts and f_{slope} the frequency slope of the chirp ramp.

This transmitted waveform reaches the target after some propagation delay and incurring free space losses, and is then scattered back towards the radar, eventually reaching the receiving antennas with an additional propagation delay and more free space losses. Thus the received waveform s_i^{rx} at the i-th virtual xy-polarised channel, i.e. a virtual channel with an x-polarised receiving channel and a y-polarised transmitting antenna, can be modelled as shown in (5.3), as:

$$s_i^{rx}\left(t, \Delta t_i\right) = L S_{xy} e^{2\pi j \left(f_{start} + \frac{1}{2} f_{slope}\left(t - \Delta t_i\right)\right)\left(t - \Delta t_i\right)}. \tag{5.3}$$

Here, L denotes the total propagation losses and Δt_i indicates the total propagation delay to and back from a target. The total propagation delay for a measured channel is a function of the start range r_0 of a target from the origin of the virtual array formed by the radar system, its radial velocity with respect to the radar v_t, elevation θ_t, and azimuth ϕ_t, as shown in (5.4), as:

$$\Delta t_i\left(r_0, v_t, \theta_t, \phi_t\right) = 2\frac{r_0 + v_t T_i\left(n\right)}{c} + \frac{\hat{r}\left(\theta_t, \phi_t\right) \vec{p}_i}{c}. \tag{5.4}$$

As can be seen in (5.4), Δt_i is also dependent on the location of the i-th virtual channel $\vec{p}_i$ in the virtual array which is the sum of $\overrightarrow{p^{tx}}$ and $\overrightarrow{p^{rx}}$, which respectively are the positions of the transmitting antenna $\overrightarrow{p^{tx}}$ and the receiving antenna $\overrightarrow{p^{rx}}$ corresponding to that virtual channel. Furthermore, c indicates the propagation velocity of electromagnetic waves and $T_i\left(n\right)$ represents the time elapsed since the first chirp of the sequence, in order to account for the range migration of a target due to its radial velocity with respect to the radar. Note that T_i itself depends on the chirp number n, the inter-chirp duration T_{chirp} as well as a time offset ΔT_i as shown in (5.5):

$$T_i\left(n\right) = n T_{chirp} + \Delta T_i. \tag{5.5}$$

This time offset results from the TDM operation of the radar. Namely, when the transmitters of the radar operate in an interleaved fashion, the chirps corresponding to the virtual channels using the second transmitter lag behind one inter-chirp duration. This results in turn the virtual channels corresponding to the third transmitter to have an offset of two inter-chirp durations, and so forth for all the other available transmitters.

Furthermore, $\hat{r}$ is the unit vector that indicates the angle of arrival of the wave and is dependent on the elevation and azimuth of a target as shown in (5.6):

$$\hat{r}\left(\theta_t, \phi_t\right) = \begin{bmatrix} \cos\theta_t \sin\phi_t \\ \cos\theta_t \cos\phi_t \\ \sin\theta_t \end{bmatrix}. \tag{5.6}$$

In an FMCW radar system, the received signal is subsequently de-chirped by means of complex mixing it with the transmitted signal. This results in the final signal model of the i-th virtual channel s_i as sampled by the ADCs corresponding to that channel. This can be mathematically written as shown in (5.7) as follows:

$$\begin{aligned} s_i\left(t, \Delta t_i\right) &= s_i^{rx}\left(t, \Delta t_i\right)^* s_i^{tx}\left(t\right) \\ &= LS_{xy} e^{2\pi j\left(f_{start}\Delta t_i - \frac{1}{2} f_{slope}\Delta t_i^2\right)} e^{2\pi j f_{slope} t \Delta t_i}. \end{aligned} \tag{5.7}$$

In (5.7), superscript * indicates the complex conjugate operator.

Using this signal model, the signal processing pipeline to estimate the range, radial velocity, elevation, azimuth, and scattering parameters of a target for a single polarimetric channel can be developed. First, the signal model can be simplified by using the assumption that $f_{start}\Delta t_i \gg \frac{1}{2} f_{slope}\Delta t_i^2$. This assumption is typically valid for mm-wave automotive radar, as the sampled bandwidth of the chirp is much smaller than the start frequency; for example, the maximum available bandwidth in this band is 4 GHz, while the minimum start frequency is 76 GHz. Furthermore, the full 4 GHz bandwidth is not usually sampled in its entirety, as this would require high performance ADCs, whereas lower performing but cheaper ADCs can generally provide the required sample rates necessary to achieve, amongst others, adequate unambiguous range. Applying the aforementioned assumption results in (5.8):

$$s_i\left(t, \Delta t_i\right) = LS_{xy} e^{2\pi j f_{start}\Delta t_i} e^{2\pi j f_{slope} t \Delta t_i}. \tag{5.8}$$

Combining (5.4) and (5.8) and performing a Fourier transform over t, the r_0 of the target can be recovered given that $2\frac{r_0}{c} \gg 2\frac{v_t T_i}{c} + \frac{\hat{r}\vec{p}_i}{c}$, which is valid as r_0 is the dominant term of the propagation delay. This results in (5.9), as follows:

$$s_i^r = LS_{xy} e^{2\pi j f_{start}\left(2\frac{r_0 + v_t T_i}{c}\right) + j\vec{k}\vec{p}_i} \delta\left(r - r_0\right). \tag{5.9}$$

Here, $\vec{k}$ represents the wave vector and is defined as $\frac{2\pi}{\lambda}\hat{r}$, where λ is the wavelength at the start frequency of the chirp.

Subsequently, the target's radial velocity can be determined by performing a Fourier transform over n, which corresponds to a transform over the sequence of chirps belonging to the considered virtual channel. This results in (5.10), as:

$$s_i = LS_{xy} e^{2\pi j f_{start}\left(2\frac{r_0 + v_t \Delta T_i}{c}\right) + j\vec{k}\vec{p}_i} \delta\left(v - v_t\right) \delta\left(r - r_0\right). \tag{5.10}$$

Note that the channel time offset term in (5.10) introduces an additional velocity dependent phase shift between channels. This phase shift appears due to range migration of a moving target in between the starts of multiple different chirp sequences belonging to virtual channels because of the TDM used by the radar system to preserve waveform orthogonality. If left uncompensated, this additional phase shift leads to an additional error in the estimation of the phase of the scattering parameter measured by the corresponding virtual channel.

As the aforementioned phase shift is solely dependent on the target's radial velocity and the channel time offset, which are known quantities after the estimation step in (5.10), it can be compensated by multiplying each range/velocity bin by a factor of $e^{-4\pi j f_{start} \frac{v}{c} \Delta T_i}$, similar to the approach presented in [67]. This leads to (5.11):

$$s_i = L S_{xy} e^{4\pi j f_{start} \frac{r_0}{c} + j\vec{k}\vec{p}_i} \delta\left(v - v_t\right) \delta\left(r - r_0\right). \tag{5.11}$$

Subsequently, the azimuth and elevation of the target can be estimated. This can be done by means of Fourier transformation over virtual channels belonging to the same polarimetric channel when they are uniformly spaced, so that the backscattered wave front of a target is uniformly sampled in space. This is similar to estimation of target range and velocity where the aforementioned wave front is sampled uniformly in time rather than in space. When the virtual channels are not spaced uniformly, the target azimuth and elevation can be estimated using digital beam forming instead. This procedure is mathematically shown in (5.12), as follows:

$$s = \frac{L S_{xy} \delta\left(v - v_t\right) \delta\left(r - r_0\right)}{N} \sum_{i=1}^{N} e^{4\pi j f_{start} \frac{r_0}{c} + j\vec{k}\vec{p}_i} e^{j\vec{\beta}_i}. \tag{5.12}$$

In this equation, N is the total number of virtual channels belonging to a specific polarimetric channel and $\vec{\beta}_i$ represents the steering vector which is defined as shown in (5.13):

$$\vec{\beta}\left(\theta, \phi\right) = -\frac{2\pi}{\lambda} \begin{bmatrix} \cos\theta \sin\phi \\ \cos\theta \cos\phi \\ \sin\theta \end{bmatrix} \vec{p}_i. \tag{5.13}$$

When the steering vector aligns with the wave vector, the magnitude of the summation in (5.12) will be maximum, and thus the azimuth and elevation of a target are found.

Now that the target's range, velocity, elevation, and azimuth have been estimated, the amplitude and phase of s are the product of the propagation losses L, the scattering parameters S_{xy}, and a residual phase term $e^{4\pi j f_{start} \frac{r_0}{c}}$. As for determining the scattering matrix, only the relative phase of the scattering parameters is of importance, the residual phase term can be eliminated by subtracting the phase of the first scattering parameter from all four elements of the scattering matrix, since r_0 is independent of the polarimetric channel. Furthermore, the propagation losses are dominated by r_0 and thus are also independent of polarisation. Therefore, this term can be compensated for by using the radar equation [2].

Thus, after the compensation of the residual phase term and the propagation losses, the amplitude and phase values for each range-angle-velocity bin remain, and they represent the scattering parameter corresponding to the polarimetric channel. The final scattering matrix for each range-angle-velocity bin is then subsequently found by combining the scattering parameters of all polarimetric channels.

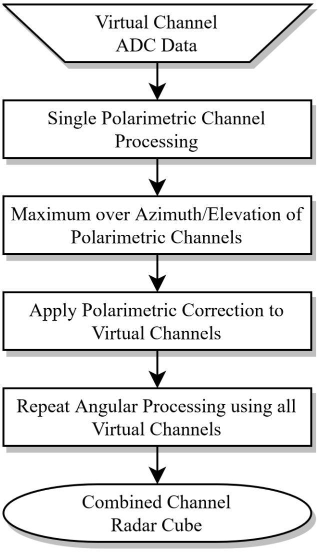

Figure 5.1: Block diagram of the proposed combined polarimetric channel processing method to achieve comparable resolution as a single-polarised radar with the same array configuration.

5.2.2. Combined Polarimetric Channel Processing

As the total aperture of a polarimetric MIMO radar system is subdivided into multiple polarimetric channels, the angular resolution of each polarimetric channel is limited by the aperture corresponding to that specific polarimetric channel. The coupling between the scattering parameters and angle that is present when processing all channels together, as if it were a single polarimetric radar system, leads to errors in the estimation of target azimuth and elevation. This usually results in coarser angular resolution for a polarimetric radar when compared to a single-polarised radar system with the same amount of total virtual channels.

However, the signals received by the individual polarimetric channels can be combined to increase the resulting angular resolution compared to the resolution in a single polarimetric channel. A method to accomplish this, based on the assumption that only one dominant target is present per range-velocity bin, is shown schematically in Fig. 5.1.

As shown in Fig. 5.1, first the single polarimetric channel processing described in section 5.2.1 is performed to find the scattering parameters corresponding to the four polarimetric channels. Subsequently, a new maximum radar cube $s_{combined}$ is constructed from the maximum of the amplitudes of the radar cubes corresponding to all four polarimetric channels, denoted from s_{xx} to s_{yy}, as shown in (5.14):

$$s_{combined} = \max\left(|s_{xx}|, |s_{xy}|, |s_{yx}|, |s_{yy}|\right). \tag{5.14}$$

This combined radar cube is then subsequently used to find the azimuth and elevation at which the return with the highest intensity is obtained for each range-velocity bin by taking the maximum over the elevation and azimuth. By combining all polarimetric channels, the correct angles corresponding to a target can still be found if no return is present in one

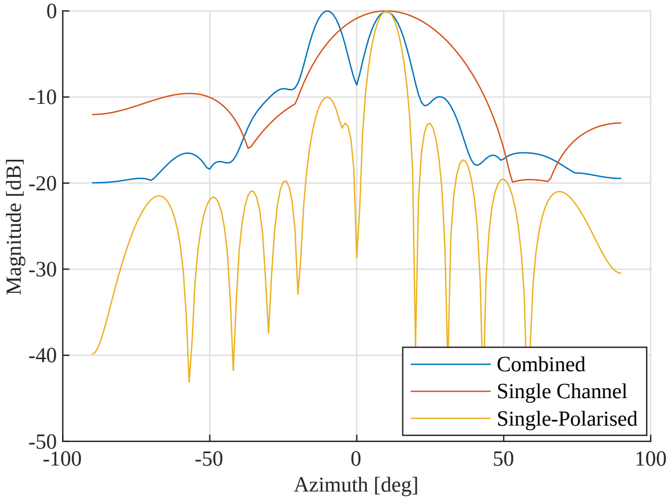

Figure 5.2: Simulated azimuth cut of two targets located at -10° and +10°, as measured by a single polarimetric channel (red), all polarimetric channels combined using the proposed method (blue), and a single-polarised array of the same dimensions (yellow).

of the channels. Subsequently, for each polarimetric channel, the phase of the scattering parameters is found for each range-velocity bin using the azimuth and elevation of the target found in the last step. The range-velocity spectra of each virtual channel are then corrected for polarimetric effects on the measured phase by subtracting the previously found phase from each corresponding range-velocity bin as shown in (5.15):

$$s_{i,corrected} = s_i e^{-j\angle S_{xy,max}}. \tag{5.15}$$

Here, $s_{i,corrected}$ indicates the corrected virtual channel radar cube and $S_{xy,max}$ represents the scattering parameter corresponding to the i-th virtual channel, found in the range-velocity bin at the azimuth/elevation angle at which maximum return was found in $s_{combined}$.

Thereafter, digital beam forming can be applied using all corrected virtual channels to obtain a combined channel radar cube without polarimetric information, but with higher angular resolution compared to single polarimetric channel processing.

The limitation of the proposed combined channel processing method lies in the assumption that only one dominant target is present per range-velocity bin. When this is not satisfied, only the polarimetric phase-shift of the strongest target within the range-velocity bin is compensated properly, introducing errors in the estimation of the other targets that are present in that same bin, but at different azimuth and elevation angles.

Fig. 5.2 shows the azimuth cut of a simulated scene with two targets at a range of 15 m. The first and second targets are located at -10° and +10° azimuth, respectively, with velocities of -3 m/s and +3 m/s. For simulation purposes, the scattering parameters used for the first and second target were a value of 1 and $\sqrt{10}e^{j\frac{\pi}{6}}$ for S_{xx} respectively, 4 and $10e^{j\frac{\pi}{3}}$ for S_{xy}, $\sqrt{10}e^{j\frac{\pi}{3}}$ and $4e^{j\frac{\pi}{5}}$ for S_{yx}, and $10e^{j\frac{\pi}{4}}$ and $e^{j\frac{\pi}{2}}$ for S_{yy}. The antenna array used in this simulation is a uniform linear array with 12 virtual channels with half-λ spacing, subdivided equally between the four polarimetric channels. The return as function of azimuth obtained with this array is compared in Fig. 5.2 with the same array but with all virtual channels belonging to the same polarimetric channel in order to simulate a conventional single-polarised MIMO radar system. This figure also shows the estimated azimuth using a single polarimetric channel. It can be seen that the proposed combined channel processing method provides a similar level of azimuthal resolution compared to single-polarised radar, while also being able to provide coarser-resolution polarimetric information that can be used for classification purposes as demonstrated in Section 5.5. Furthermore, the received power in all polarimetric channels is summed coherently, thus providing better signal to noise ratios with respect to a comparable single-polarised antenna measuring a polarimetric channel that only provides weak returns.

5.3. Experimental Measurements

This section describes the experimental measurements. In 5.3.1, the polarimetric radar system is introduced while 5.3.2 describes the calibration procedure. The data collection procedure is detailed in 5.3.3.

5.3.1. Polarimetric MIMO Radar System

To perform polarimetric automotive radar measurements, a novel polarimetric MIMO radar system was developed in collaboration with Huber+Suhner (H+S). This radar system is based on Texas Instruments' AWR2243BOOST radar evaluation module, which is equipped with a AWR2243 automotive FMCW radar chip. To enable MIMO radar functionality, the AWR2243 has 3 transmit channels and 4 receive channels. Furthermore, the AWR2243BOOST evaluation module is stacked on a Texas Instruments DCA1000 processing board to efficiently transfer the raw data gathered by the AWR2243's ADCs to a computer for further processing. The radar assembly is subsequently mounted on a tripod, resulting in it being placed at a height of about 65 cm above ground level.

The radar system was programmed to use a high-resolution short range waveform so that the polarimetric structure of the target-under-test could be investigated. To this end, the AWR2243 chip was set to use a bandwidth of 3.58 GHz, resulting in a range resolution of 4.2 cm. To achieve a maximum unambiguous velocity of 7 m/s in combination with a maximum unambiguous range of 31 m, the AWR2243's maximum sample rate of 22 Msps, collecting 750 samples per chirp, in combination with a frequency slope of 101 MHz/µs were utilised. Furthermore, each transmitter was set to transmit 64 chirps in an interleaved fashion to obtain a velocity resolution of 0.22 m/s while keeping the phase change between channels for moving targets caused by TDM (as mentioned in section 5.2) and target geometry changes as small as possible. A full list of waveform parameters can be found in Table 5.1.

Unlike the regular AWR2243BOOST evaluation module, the polarimetric MIMO radar used for this work features a custom antenna array manufactured using 3D printing technology by Hubert+Suhner AG [68–70] instead of series-fed patch arrays with which the standard evaluation module is equipped. The custom antenna array designed by H+S comprises of seven sub-arrays consisting of 8 open-ended waveguide radiators positioned vertically with respect to each other to achieve a narrow beam in the elevation direction. Three of the sub-arrays function as transmitters, while the other four function as receivers.

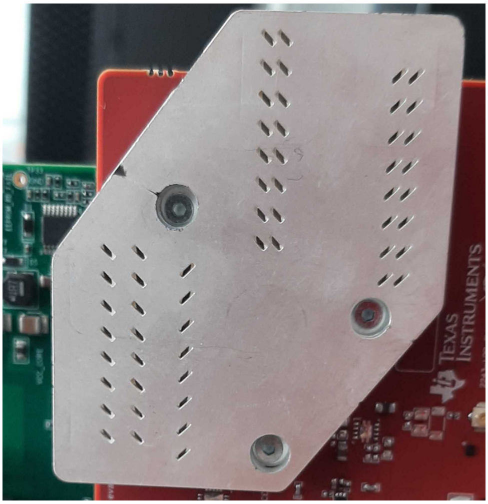

Figure 5.3: Picture of the custom polarimetric antenna mounted on a modified AWR2243BOOST evaluation module.

Table 5.1: Waveform settings for the radar module used in this work.

Start Frequency	77 GHz
Frequency Slope	101.388 MHz/µs
ADC Sample Start Time	5.12 µs
ADC Idle Time	7 µs
ADC Sample Rate	22000 ksps
ADC Samples	750
Chirps per Frame	64
Frame Repetition Time	10 ms

To implement polarimetric capabilities, instead of using horizontally oriented open-ended waveguide radiators within a sub-array, the radiators are either rotated 45° counter-clockwise with respect to the vertical plane of the transmitters, indicated as positive diagonal (PD), or 45° in the opposite direction, indicated as negative diagonal (ND). In this way an orthogonal polarisation basis is created. An advantage provided by this diagonal polarisation basis is that the radiation patterns of the ND and PD polarised sub-arrays are theoretically equal to each other, which can be exploited for calibration purposes. Also, as the ND- and PD-polarised sub-arrays are mirrored versions of each other, the implementation of both sub-arrays is simplified. In this chapter, the measured return obtained by transmitting with a YD-polarised sub-array and receiving with an XD-polarised polarised sub-array is indicated as an XY polarised channel. Here, X and Y can be either N for negative diagonal or P for positive diagonal.

A picture of the fully assembled radar system including the custom-designed 3D printed antenna can be found in Fig. 5.3. The three sub-arrays in the lower left corner of the antenna are connected to the transmitting channels of the AWR2243 chip, while the four in the

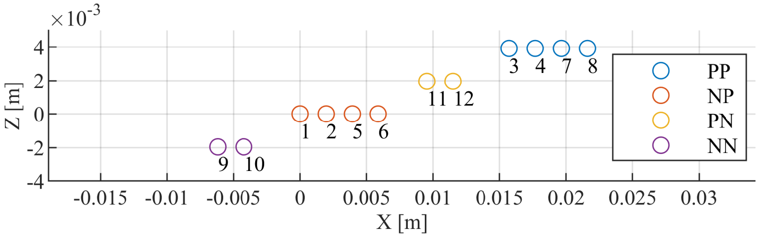

Figure 5.4: The virtual array formed by the custom polarimetric antenna as seen in the direction of transmission. The numbers indicate the corresponding virtual channel numbers.

upper right corner correspond to the receiving channels. It can be seen that two of the transmitting channels are PD-polarised, while the remaining one is ND-polarised, and that the four receiving channels are equally split between PD- and ND-polarisation. All four differently polarised channels are offset slightly in height to enable estimation of elevation when all polarimetric channels are processed together.

The virtual array formed by the antenna is shown in Fig. 5.4. It can be seen that the number of virtual channels dedicated to each of the four polarimetric channels is unbalanced due to the uneven number of transmitting channels on the AWR2243 chip. Furthermore, all virtual channels corresponding to a polarimetric channel form dense linear arrays, thus ensuring that each polarimetric channel can be processed individually without creating grating lobes in the visible region.

5.3.2. Calibration

To eliminate the effects on phase and amplitude variations due to the different feed-line lengths in the antenna sub-arrays, the radar system must be calibrated. Unfortunately, simple measurements of a corner reflector do not suffice for this purpose, as this target does not change the polarisation of the backscattered sensing wave, thus allowing only for calibration of the two co-polarised channels. To solve this issue, multiple different calibration targets with different polarimetric properties need to be used [71, 72].

Alternatively, instead of using passive calibration targets, the radar system can be calibrated with a radar target simulator equipped with a vertically polarised horn antenna. This approach has a few advantages, the first of which is that for a diagonal polarisation basis, all polarimetric channels should measure the same scattering parameters, thus removing the need for using multiple different calibration targets. In this way, the potential errors introduced by misalignments between calibration targets are avoided. Furthermore, the definition of an arbitrary phase relation between co- and cross-polarised channels is no longer required. Secondly, the radar target simulator allows for simulating a target with a given velocity, which increases the measured signal-to-noise ratio of the simulated target, as this is better separated from the static clutter present in the scene.

Because of these advantages, calibration of the radar system was performed in this work using a AREG800A radar target simulator equipped with a AREG8-81S horn antenna frontend manufactured by Rohde&Schwarz. The radar target simulator was configured to simulate two targets at a distance of 24 and 28 m, with velocities of 3 m/s and -3 m/s, respectively. The first target serves as a calibration target, while the latter target could be used as a verification target. Subsequently, 1000 frames of the simulated targets were captured using the polarimetric radar system described in the previous section and processed. For each of the 12 virtual channels, the mean measured phase and amplitude over the 1000 captured frames were computed. The reciprocal of the mean phase and amplitude could subsequently be used as calibration coefficients for the virtual channels. Afterwards, the found calibration coefficients were applied to each of the virtual channels and another set of 1000 calibration frames was processed. It was found that for the calibration target, the standard deviation for the worst performing channel was 0.78 dB in amplitude while the standard deviation of the phase was 5.5°. The mean values for the amplitude and phase were found to be below 0.03 dB and 0.38° respectively. For the verification target, the worst-case standard deviations of the amplitude and phase were 0.79 dB and 5.3°, respectively, while the mean values were below 1.26 dB in amplitude and 1.9° in phase. From these results it can be concluded that the calibration procedure was successful, and that systematic errors introduced by differences between channels such as differing feed-line lengths were appropriately compensated.

5.3.3. Data collection

To evaluate the effectiveness of polarimetry for classification of vulnerable road users, multiple classes of VRUs and a car were measured. The measurements were performed in *two different campaigns*. The first was focused on pedestrians and bicyclists, while the second measurement campaign also included measurements of another class of VRU (motorcyclist) as well as a non-VRU (car). Furthermore, the first measurement campaign took place on a grass field in winter time, while the second measurement campaign took place on an asphalt parking lot during spring time.

In the first measurement campaign, 5 different bicyclists and pedestrians were measured. In the second measurement campaign, 3 different bicyclists and pedestrians were measured, where 2 of the 3 pedestrians and bicyclists also took part in the first data collection in order to compare measurement results between both campaigns. Besides this, during the second measurement campaign, also a motorcyclist was measured as an additional class of VRU (see Fig. 5.5), as well as a car representing an example of a non-VRU target.

In both measurement campaigns, each target was measured while moving along four different directions with respect to the radar, namely: towards the radar, away from the radar, diagonally towards the radar, and diagonally away from the radar. The diagonal directions are also denoted by the addition of 45° in the naming convention of the directions. A schematic drawing of the measurement geometry is shown in Fig. 5.6. Furthermore, each test object was measured three times moving along each direction to obtain statistical information. The measurement procedure can be summarised as follows:

1. Connect the radar system to a power supply and laptop, configure the radar system with the correct waveform parameters mentioned in Table 5.1, and mark the measurement course.

2. Let the test object approach the start marker for one of the four measurement directions, so that the target is at constant speed during the radar measurements.

3. Start the radar measurements when the test object reaches the start marker.

Figure 5.5: Motorcyclist riding along the measurement area away from the radar.

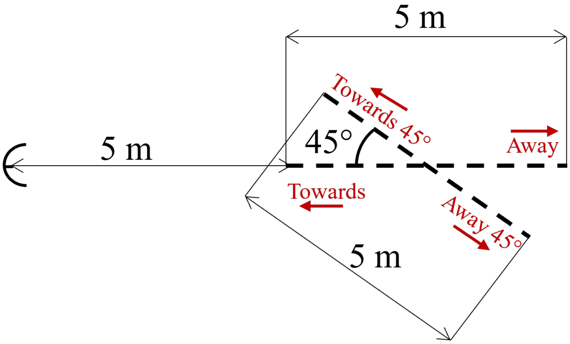

Figure 5.6: Schematic representation of the geometry used for polarimetric radar measurements of moving VRUs. The direction identifiers are indicated in red.

4. Stop the radar measurements when the test object reaches the end marker.

5. Repeat measurements for the measured target moving along the same direction, for 3 times from step 3.

6. Repeat measurements for the measured target moving along the remaining three directions from step 3.

7. Repeat measurements for different targets from step 3.

All measurement data were stored locally on a laptop, which could later be transferred to a workstation computer for further processing after the measurements had been completed. Furthermore, the data collected for this work have been made publicly available and can be found in[73].

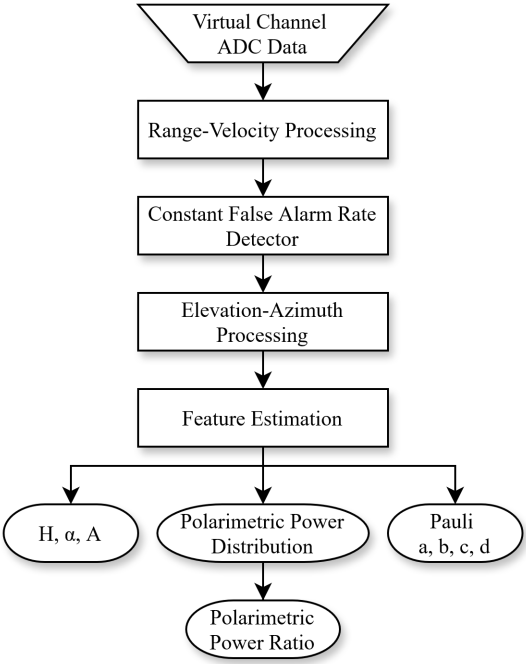

Figure 5.7: Block diagram of the post-processing steps to estimate polarimetric features from the radar measurement data.

5.4. Measurement Data Post-Processing

To use the data collected during the measurement campaigns for classification purposes, post-processing must be applied first. A block diagram of this procedure is shown in Fig. 5.7.

The measurement data is processed similarly to the single polarimetric channel processing procedure in section 5.2.1. The first step in this procedure is to apply range-velocity processing to the raw ADC data. As shown in section 5.2.1, this can be done by means of Fast Fourier Transform (FFT) over fast time and slow time dimensions for each virtual channel; for both FFTs, here a Kaiser window with a beta value of 6 is used. After transforming the ADC-data to the range-velocity domain, a velocity-dependent phase correction is applied to compensate for the phase shift that occurs for moving targets due to TDM, as mentioned in section 5.2.1.

Unlike for the single channel polarimetric radar data processing procedure in section 5.2.1, a detector is applied here to the data before performing elevation-azimuth processing. By performing detection on the range-velocity spectra of the individual virtual channels before elevation-azimuth processing, this step needs to be applied only to the range-velocity bins that contain a detection. This greatly reduces requirements on memory and computational resources. The detector used for this purpose first estimates the noise probability density function using samples from an area in the range-velocity plane in which no targets were present during the measurements. The bins in the range-velocity spectrum used for this are those corresponding to velocities in the -7 m/s to -1 m/s and 1 m/s to 7 m/s intervals, and have a range between 15 m and 20 m. Subsequently, from this estimate, the detection threshold is determined such that the probability of false alarm is 10^{-15}, resulting in a detector with the constant-false alarm rate property. This probability of false alarm was empirically found to provide a good balance between missed detections and false alarms. Furthermore, the bins with velocities between -0.3 m/s and 0.3 m/s are not considered to prevent detections of static clutter. Also, it should be noted that a detection is declared when a value above the aforementioned threshold is found in at least one of the twelve virtual channels, as due to the polarimetric properties of a target, a target may provide a stronger return in some virtual channels, while a weaker return is measured by the virtual channels that correspond to a different polarimetric channel.

After the detection procedure, elevation-azimuth processing is applied on the bins at which a detection was declared. As the apertures of each sub-array corresponding to the polarimetric channels are uniform linear arrays, no elevation information can be obtained from single polarimetric channel processing. Therefore, the angular processing is done using steering vectors generated with azimuth values ranging from -90° to 90° in 1° increments, in combination with an elevation angle of 0°. After angular processing, the angle for which the sum of the squared absolute values of the scattering matrix is maximum is computed. The scattering matrix corresponding to this range-velocity-azimuth bin is then subsequently used to compute several polarimetric features, namely the polarimetric power distribution and corresponding polarimetric power ratios. Furthermore, also the a, b, c, and d values resulting from the Pauli decomposition and the H, α, and A features from the $H\alpha A$-decomposition are considered [32].

The target *polarimetric power distribution* P_{xy} for the xy-polarised channel is defined as the total backscattered power measured by each polarimetric channel, computed over all N detections corresponding to a target within a single frame. This can be mathematically formulated as:

$$P_{xy} = \sum_{i=1}^{N} \left|S_{xy}^{i}\right|^{2}. \tag{5.16}$$

N represents the total number of detections corresponding to the observed target within a frame, while S_{xy}^{i} indicates the scattering parameter corresponding to the i-th detection.

From the target polarimetric power distribution, the target *polarimetric power ratio* Q_{xy} can be found. This is defined as the target polarimetric power distribution normalised by the total power scattered back by the target over the N detections. This can be mathematically expressed as shown in (5.17), as:

$$Q_{xy} = \frac{P_{xy}}{\sum_{i=1}^{N}\left(\left|S_{xx}^{i}\right|^{2} + \left|S_{xy}^{i}\right|^{2} + \left|S_{yx}^{i}\right|^{2} + \left|S_{yy}^{i}\right|^{2}\right)}. \tag{5.17}$$

This feature is independent of the total amount of returned power and thus represents the polarimetric composition of a target. This allows to compare the polarimetric composition of weak targets such as pedestrians, with those of stronger targets like vehicles.

Furthermore, the scattering matrices belonging to the individual detections within a frame can be decomposed to analyse the underlying scattering mechanisms corresponding to a detected target. One of these decompositions is the Pauli-decomposition, which decomposes the scattering matrix in four individual scattering mechanisms [32]. As the polarimetric radar system used in this work measures the scattering parameters in a diagonal polarisation basis, the first of the *Pauli-features*, a, represents the contribution of odd-bounce scattering such as that occurring with scattering from a sphere or plane. The second feature, b, represents scattering from a dihedral with an orientation of 45° with respect to the horizon, while c represents scattering from a dihedral with an orientation of 0° or 90°. Lastly, d corresponds to the asymmetric components of the scattering matrix. The a, b, c, and d features can be computed as shown in (5.18), as follows:

$$\begin{aligned} a &= \frac{S_{PP} + S_{NN}}{\sqrt{2}} \\ b &= \frac{S_{PP} - S_{NN}}{\sqrt{2}} \\ c &= \frac{S_{PN} + S_{NP}}{\sqrt{2}} \\ d &= j\frac{S_{PN} - S_{NP}}{\sqrt{2}} \end{aligned} . \tag{5.18}$$

Another polarimetric decomposition that can be applied to data from the measurements is the so called *$H\alpha A$-decomposition*. This decomposition operates on the coherency matrix found from a set of scattering matrices and computes the scattering entropy H, scattering angle α, and scattering anisotropy A. These features are found by performing an eigenvalue decomposition on the coherency matrix from which three eigenvalues λ_1, λ_2, λ_3 and their corresponding eigenvectors are obtained. Here, subscript 1 corresponds to the largest eigenvalue, while 3 corresponds to the smallest eigenvalue. These eigenvalues are then used to compute three pseudo-probabilities, which are defined as the eigenvalue divided by the sum of the three eigenvalues. More information on the computation of the coherency matrix and pseudo-probabilities can be found in [2] and [32]. The entropy can then subsequently be found as shown in (5.19), as:

$$H = -\sum_{k=1}^{3} P_k \log_3 \left(P_k\right). \tag{5.19}$$

The entropy represents the randomness of the polarimetric response from a target. If all scatterers corresponding to a target are equal, then the coherency matrix will have only one strong eigenvalue leading to an entropy of 0. Conversely, a target comprising of many different polarimetric scatterers will have a high polarimetric entropy.

To compute α, first for each eigenvector a scattering angle α_k is found. This is done by taking the arccosine of the modulus of the first value of the eigenvector. Using the pseudo-probabilities in combination with these three scattering angles, α can be found using (5.20) as:

$$\alpha = \sum_{k=1}^{3} P_k \alpha_k. \tag{5.20}$$

When considering a coherency matrix obtained from scatterers corresponding to the same statistically underlying scattering mechanism, the angle α can be used to identify the nature of this scattering mechanism. In the case of performing the $H\alpha A$-decomposition on all detections within a frame, this is no longer necessarily true, as some parts of the measured target may act like a dipole while others act as a flat plate. However, in this scenario α may still contain useful information on the average scattering mechanism of the observed target.

Lastly, the polarimetric anisotropy indicates the relative importance of the second and third largest eigenvalue and can be computed via (5.21), as:

$$A = \frac{\lambda_2 - \lambda_3}{\lambda_2 + \lambda_3}. \tag{5.21}$$

The polarimetric anisotropy can help to distinguish targets when for example the first eigenvalue is relatively large, thus leading to low entropy, while the second and third eigenvalues are the same or differ significantly from each other.

5.5. Results

In this section the measurement results are analysed. First, an analysis of the polarimetric features is presented in 5.5.1. To quantify the information content provided by the polarimetric channels, two classification methods are applied and presented in 5.5.2 and 5.5.3. Specifically, in 5.5.2, classification is performed on the polarimetric power feature, while 5.5.3 considers classification based on the range-velocity signature using a Convolutional Neural Network (CNN).

5.5.1. Polarimetric Features Analysis

Firstly, the evolution of the target polarimetric ratios, as defined in (5.17), is considered as a function of time as this is an indicator of the stability of the measurement results and the influence of noise. Namely, the target pose/shape with respect to the radar is assumed to remain relatively similar from frame to frame, as the frame repetition time used in these measurements is 10 ms as shown in Table 5.1. Fig. 5.8 shows the change of the target polarimetric ratios of a bicyclist cycling towards the radar during the last 50 frames measured by the radar. From this figure, it can be seen that the target polarimetric ratios in most cases remain relatively stable from frame to frame, whereas over a longer time span more significant differences are observed. The latter is likely the result of changes in the target pose as the movement progresses during the data recording.

Subsequently, the distribution of the polarimetric ratios in the range-velocity spectrum can also be considered. This can be done by analysing the polarimetric ratios of the individual detections. They are computed as the ratio of the squared magnitude of the considered scattering parameter divided by the squared magnitude of all four scattering parameters for just a single detection, in contrast to the target polarimetric ratio which is computed using all detections corresponding to a target within a frame. Fig. 5.9 shows the distribution of the polarimetric ratios of each detection in the range-velocity plane. Specifically, in this RGB-image, the red channel corresponds to the PP-polarised ratio, the green channel corresponds to the sum of the polarised ratios of the cross-polarised channels, and the blue channel represents the NN-polarised ratio. The picture on the left hand side represents a cyclist cycling on a regular bicycle, while the picture on the right hand side shows a person cycling on a folding bicycle. Even though the bicycles differ from each other, it can be seen that they

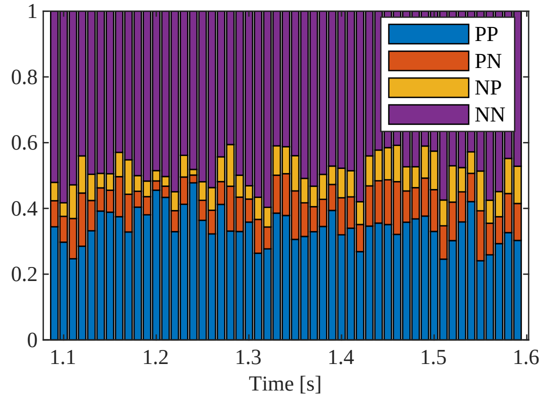

Figure 5.8: Target polarimetric ratios as a function of time for a bicyclist cycling towards the radar; the recorded time corresponds to 50 frames.

share a similar polarimetric structure. It can be seen for instance that the rear part of the front wheel of the bicycle provides relatively strong cross-polarised backscattering, while the front part tends to provide a stronger return in the co-polarised channels. Furthermore, it can also be observed that the frame of the bicycle and the cyclist itself also lean toward higher co-polarised backscattering.

A similar comparison between two pedestrians is shown in Fig. 5.10. Here it can be seen that the forward swinging limbs exhibit relatively high co-polarised ratios as well as the body itself. The detections corresponding to the backward swinging limbs (i.e., the area with low velocity as well as furthest range) exhibit slightly increased cross-polarised polarimetric ratios with respect to the main body.

Another way of analysing the involved scattering mechanisms is by considering the Pauli features. The normalised Pauli-features for a cyclist riding towards the radar are shown in Fig. 5.11. From this figure, it can be seen that the a and b features are strongest for the cyclist and bicycle frame, while c is highest for the rear part of the bicycle front wheel. This indicates that the bicycle frame and the cyclist mostly provide odd-bounce scattering in combination with scattering mechanisms corresponding to 45°-oriented dihedrals. For the bicycle wheel and spokes, the main scattering mechanism corresponds with scattering from 0°/90°-oriented dihedrals.

Furthermore, it should be noted that the Pauli features are relatively sensitive to noise in the phase measurements of the scattering parameters. The Pauli feature d shows specifically the impact of this characteristic, as for monostatic radar this feature should show no returns. Due to the phase sensitivity of this feature, a phase error of 30° between the measured cross-polar scattering parameters, corresponding to a distance of about 0.3 mm in free space at 77 GHz, already limits the lower bound of the d-feature at about 11 dB below the c-feature. At mm-wave frequencies, this type of measurement error could for example be caused even by thermal expansion effects of the radar board, or small changes between the tightness of the mechanical fasteners after adjustments to account for vibrations when transporting the radar to the measurement campaign location.

Subsequently, the clusters formed by the target polarimeric ratios, computed using all

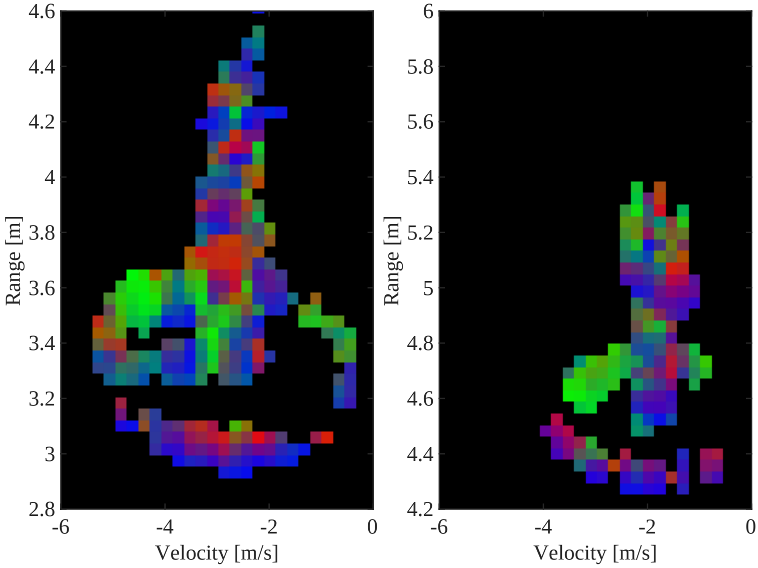

Figure 5.9: Distribution of polarimetric ratios of individual detections in the range-velocity plane for cyclists cycling towards the radar on a regular bicycle (left) and a folding bicycle (right). The red, green, and blue channel represent respectively the PP-polarised ratio, the sum of PN- and NP-polarised ratios, and the NN-polarised ratio.

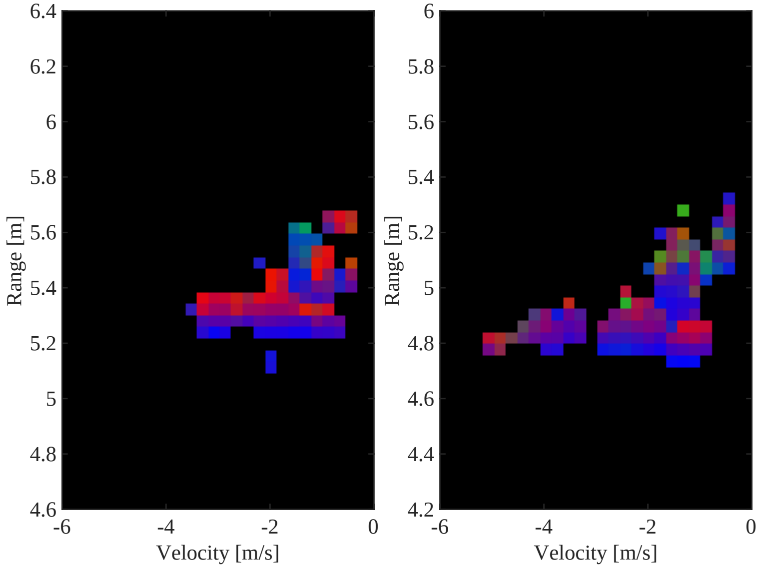

Figure 5.10: Distribution of polarimetric ratios of individual detections in the range-velocity plane for two different pedestrians walking towards the radar. The red, green, and blue channel represent respectively the PP-polarised ratio, sum of PN- and NP-polarised ratios, and the NN-polarised ratio.

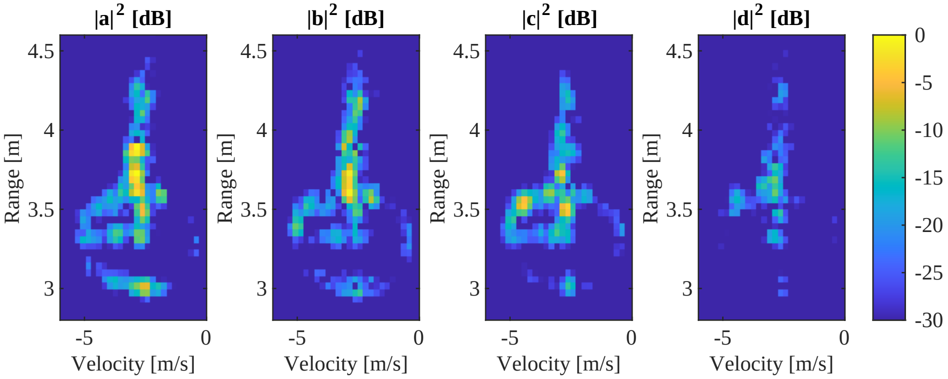

Figure 5.11: Normalised Pauli features for a cyclist riding towards the radar in dB scale, normalised with respect to the largest value of the four Pauli features.

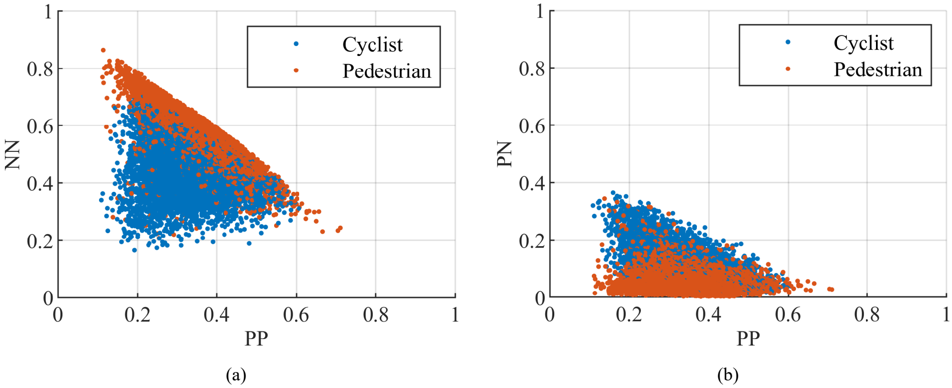

(a)

(b)

Figure 5.12: Clusters formed corresponding cyclists and pedestrians moving towards and away from the radar during the first measurement campaign by the polarimetric ratios for the: (a) PP- and NN-polarised channels; and (b) PP- and PN-polarised channels.

detections within a frame as defined in (5.17), are considered. Figs. 5.12a and 5.12b show the clusters formed by the polarimetric ratios of cyclists and pedestrians as obtained during the first measurement campaign. From these two figures, it can be seen that a cyclist results generally in more cross-polarised backscattering compared to the pedestrian. This can be potentially explained by the vertical and horizontal metal structures of the bicycle frame and wheels, which convert part of the diagonal polarised waves of the radar used in this work to horizontally and vertically polarised waves.

As different classes of targets, besides having different polarimetric ratios, can also return different amounts of power, it is useful to consider this aspect in deriving polarimetric features and then cluster the results. This can be done by looking at clusters formed by the total backscattered power of each channel as defined in equation (5.16). Figs. 5.13a and 5.13b show this for all target classes moving towards and away from the radar as measured during the second measurement campaign. It can be seen that when also considering the

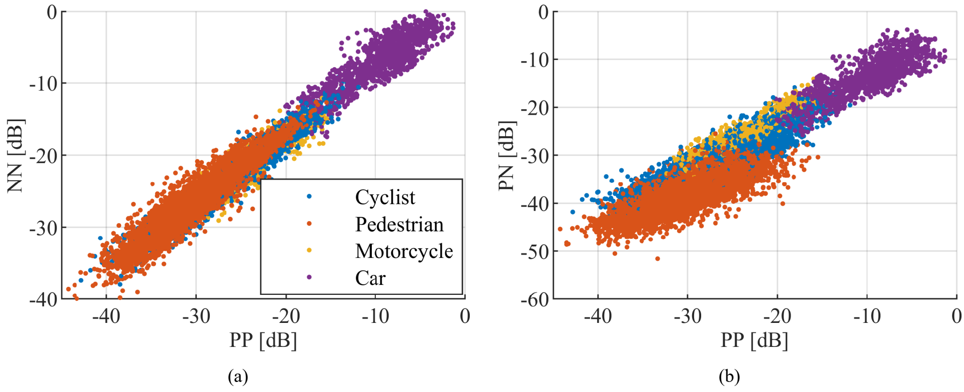

Figure 5.13: Clusters formed by the polarimetric power received of a car, a motorcycle, cyclists, and pedestrians moving towards and away from the radar during the second measurement campaign by: (a) the PP and NN channels; (b) the PP and PN channels.

magnitude of the backscattered power, the cluster formed by the car is relatively well separated from the VRU classes. These figures also show that the measured backscattering from the motorcycle behaves similar to that of bicycles, but usually with a stronger return and less variation in cross-polarised scattering.

Comparing Figs. 5.13a and 5.13b, it can be observed that when also considering the cross-polarised component of the scattering matrix, the separation of the clusters increases and thus that the cross-polarised channels are potentially able to provide useful information for classification purposes. For example, when considering Fig. 5.13a, it is difficult to distinguish the motorcycle and bicycle from each other, but when taking the cross polarised channel also into consideration it can be seen that the motorcycle becomes more easily separable.

For a comparison, the clusters formed by the H, α, and A features, shown in Figs. 5.14a and 5.14b, show less separation between clusters compared to the polarimetric power. Although each cluster class occupies a specific section in the feature space formed by H, α, and A-features, classification based exclusively on these features may be difficult due to the significant overlap between clusters. It can be seen that pedestrians generally have lower entropy than the other classes, as well as a high anisotropy. This indicates that the detections corresponding to the pedestrian within a frame generally have the same polarimetric properties. In contrast, the motorcyclist and cyclist classes have the highest entropy values, indicating that these classes comprise of mixtures of different scattering mechanisms. When considering the anisotropy of the bicycle and motorcycle class, it can be seen that the anisotropy values generally range from 0.1 to 0.8, which indicates that scattering matrices corresponding to detections within a frame of these classes show relatively random scattering characteristics.

5.5.2. Classification using Polarimetric Power

To investigate the effectiveness of polarimetry for classification purposes, first a Bayesian classifier based on the polarimetric power feature in dB as shown in Figs. 5.13a and 5.13b

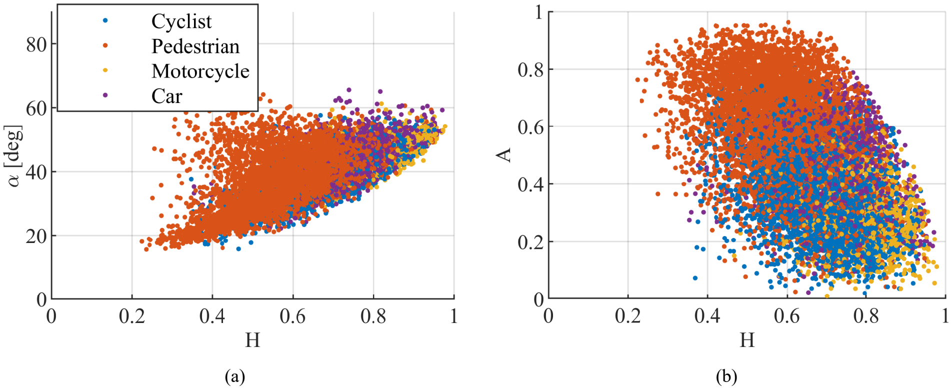

Figure 5.14: Clusters formed by the H and α features (a), and H and A features (b), of a car, a motorcycle, cyclists, and pedestrians moving towards and away from the radar during the second measurement campaign.

is employed. This classifier uses Bayes' theorem to compute the probability an observation belongs to a certain class as shown in (5.22).

$$P\left(C_k|\vec{x}\right) = \frac{P\left(C_k\right)P\left(\vec{x}|C_k\right)}{P\left(\vec{x}\right)} \tag{5.22}$$

In this equation, $\vec{x}$ represents the observed data while C_k indicates the k-th class. Furthermore, $P\left(C_k\right)$ is the prior belief of the probability of to which class the observed data belong to, $P\left(\vec{x}|C_k\right)$ the likelihood of the observed data belonging to class C_k, and $P\left(\vec{x}\right)$ the probability of observing the observed data. This is then used to compute the posterior belief of the probability to which class the observed data belongs, indicated by $P\left(C_k|\vec{x}\right)$. The posteriors for each class are calculated and the predicted class is then chosen to be the class for which the posterior is the highest. This classifier can be used iteratively over multiple frames, by updating the priors with the posteriors found for the previous frame. To compute the likelihood $P\left(\vec{x}|C_k\right)$, first the mean vector and covariance values for each cluster formed by the polarimetric power feature in dB are computed. These are then used to assign a multivariate normal distribution to each class. The likelihood can then be determined by evaluating the PDF for the observed data. The probability of observing $\vec{x}$ can then subsequently be determined by multiplying the likelihoods for all classes with their respective priors and summing over them.

In this instance, the priors were selected to be equal for each class. Furthermore, a single frame was used to determine single-frame classification performance. Fig. 5.15a shows the confusion matrix for this classification approach. From this figure, it can be seen that 1264 frames corresponding to cars out of the 1345 total frames containing a car are correctly identified as such, with a corresponding F1-score of 94.7%. Similarly, for pedestrians, the F1-score is 87.3%. For cyclists and motorcyclists, this percentage is significantly lower at 64.2% and 63.2% respectively. This is likely due to the fact that the cluster formed by the data points corresponding to the cyclists class is spread over a wider area, leading to lower values for the probability density function, which then results in lower probability of classification compared to the motorcyclist class.

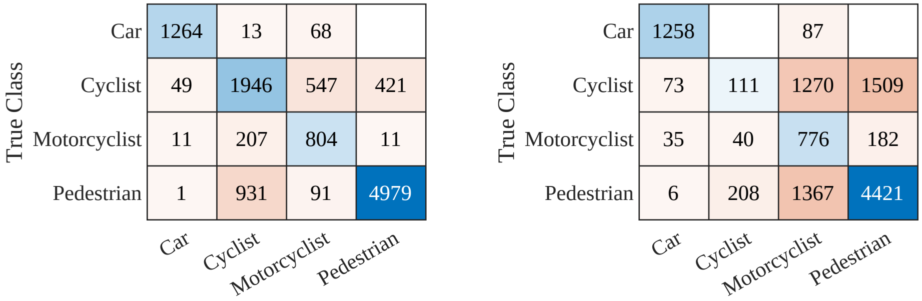

(a)

True Class \ Predicted Class	Car	Cyclist	Motorcyclist	Pedestrian
Car	1264	13	68	
Cyclist	49	1946	547	421
Motorcyclist	11	207	804	11
Pedestrian	1	931	91	4979

(b)

True Class \ Predicted Class	Car	Cyclist	Motorcyclist	Pedestrian
Car	1258		87	
Cyclist	73	111	1270	1509
Motorcyclist	35	40	776	182
Pedestrian	6	208	1367	4421

Figure 5.15: Confusion matrix for classification based on the normalised polarimetric power in dB using: (a) All polarimetric channels; (b) Only the PP-polarised channel, i.e., single polarised approach.

To compare classification performance of a polarimetric radar system to a single-polarised counterpart, the same classification procedure was applied to the polarimetric power feature using only the PP-polarised channel. The resulting confusion matrix is shown in Fig. 5.15b. It can be seen that a similar F1-score of 92.6% for cars is achieved compared to the fully polarimetric case, but that F1-scores of the VRU classes have dropped significantly. These values are 73.0%, 34.2%, and 6.7% for the pedestrian, motorcyclist, and cyclist respectively, resulting in a decrease of respectively 14.3, 29.0, and 57.5 percentage points. Thus, especially the cyclist class suffers significantly from not considering the polarimetric features.

From these results, it can be concluded that polarimetric features are able to aid in the classification process of VRUs. It should be noted that the classification performed in this section is based solely on polarimetric features. Using these features in combination with other (non)-polarimetric features and more sophisticated classification procedures could increase classification performance even further.

5.5.3. Classification using Range-Velocity Signatures

Instead of computing a single feature from all detections within a frame as done in the previous sub-section, classification can also be performed directly on the range-velocity signatures within a frame itself. This approach allows to exploit the (polarimetric) structure of the range-velocity signature, which also can contain useful information for classification.

To investigate the information content provided by the polarimetric structure/patterns formed by the range-velocity signatures, a classifier based on a simple CNN is used. The CNN can be modelled by 5 layers, namely in order: input layer, convolutional layer, full-connected layer, soft-max layer, and classification output layer. The input to the network is a three-dimensional tensor, where the first and second dimensions correspond to range and velocity, while the third represents each polarimetric channel. Also, an equivalent CNN for single-polarised radar data was set-up which uses only one of the four polarimetric channel.

The input data to the networks was normalised in two ways, in decibel scale and polarimetric ratios. For the decibel normalisation, the frames are first transformed to decibel, and subsequently scaled so that the strongest detection in the strongest polarimetric channel within the frame corresponds to a value of 1, while the weakest return in the weakest

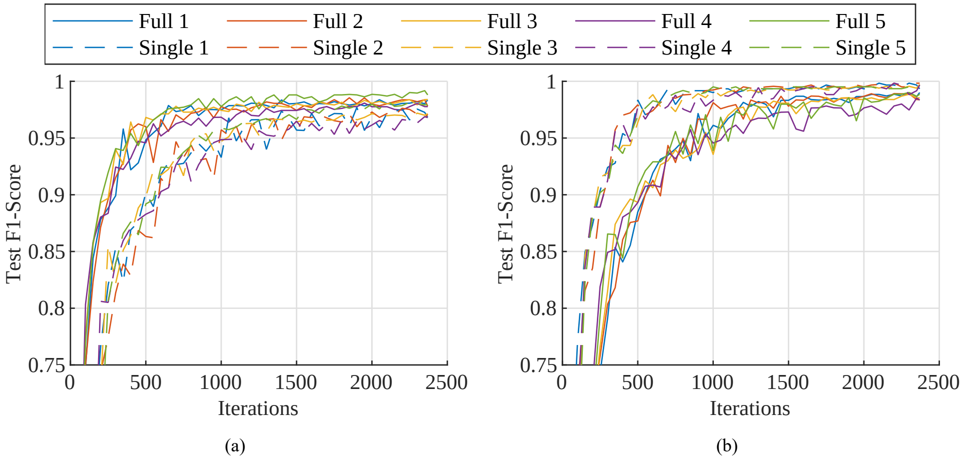

Figure 5.16: F1-score of the test set after the indicated number of completed training iterations for both fully- and single-polarised classifiers for: (a) decibel-scale input normalisation; (b) polarimetric ratio input normalisation.

polarimetric channel of that same frame corresponds to 0. For the single-polarimetric reference, the PP-polarised layer of the normalised data was used. The second normalisation method uses the polarimetric ratios of each detection. As the polarimetric ratios for each detection sum to 1, no further normalisation is required. For the single-polarised variant of the network, all detections were given a value of 1. This means that in this case both single-polarised and fully-polarised classification networks have the same shape information, obtained using all polarimetric channels, whereas the fully-polarised network also has access to the polarimetric ratios of the detections. For both normalisation methods, the data was split in 5 different test and training sets on which both the fully- and single-polarised classifiers were trained, resulting in 10 trained networks. Each of the splits was chosen such that for each class, 90% of the frames corresponding to that class were used for training, while the remaining 10% was used for testing. This allows for evaluating the spread in classification performance due to the difference in training and test datasets, where one training dataset may result in a slightly better test accuracy than another. Furthermore, each network was trained for 30 epochs at which no large improvements in test accuracy were observed anymore, and hence the training process was stopped.

Fig. 5.16a shows the F1-scores for the test sets as a function of the number of training iterations performed for decibel-scale normalisation. It can be seen that both single- and fully-polarised classifiers achieve a similar mean F1-score, of respectively 97.2% and 98.2%. Thus, the fully-polarised classifier achieves a slightly better result. It can also be noticed that the fully-polarised network is able to achieve higher F1-score earlier than the single-polarised one, thus indicating that useful information is present in the polarimetric channels for classification purposes.

Fig. 5.16b shows that for the polarimetric ratios, also similar performance between the fully- and single-polarised classifiers is achieved of respectively 98.6% and 99.7%. In contrast to decibel-normalised data, the single-polarised network performs better for the ratio-normalised data compared to the fully-polarimetric network. Also, the single-polarised

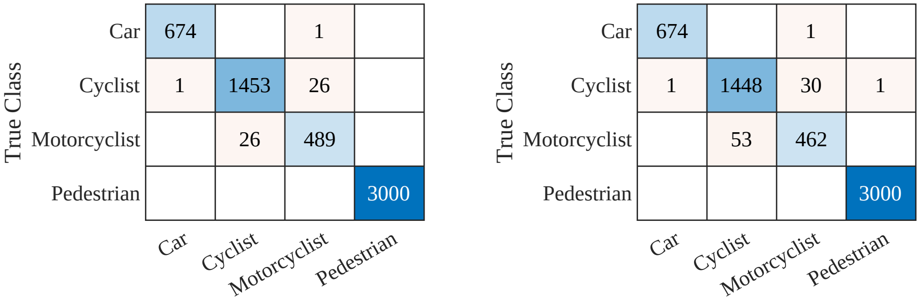

True Class \ Predicted Class	Car	Cyclist	Motorcyclist	Pedestrian
Car	674		1	
Cyclist	1	1453	26	
Motorcyclist		26	489	
Pedestrian				3000

(a)

True Class \ Predicted Class	Car	Cyclist	Motorcyclist	Pedestrian
Car	674		1	
Cyclist	1	1448	30	1
Motorcyclist		53	462	
Pedestrian				3000

(b)

Figure 5.17: Confusion matrix for classification using the decibel normalised input data format with: (a) All polarimetric channels; (b) Only a single polarimetric channel.

network achieves higher test set F1-score with fewer iterations than the fully-polarimetric classifier.

From this, it can be concluded that the shape of the range-velocity signature is most likely the most significant factor in achieving good classification performance, and that in this case the ratio-information ’distracted’ the fully-polarimetric network. This is further supported by the results obtained from the decibel-scaled data, since other polarimetric channels may contain strong returns that are weak in the channel used by the single-polarised classifier, thus enhancing the contrast of the range-velocity signature. Thus, this shows that polarimetric radar does result in better classification performance using a simple CNN-based classifier as the diversity in polarimetric channels results in more detections, and therefore a higher-contrast range-velocity signature, which may be missed when using only a single-polarised radar system. The lagging classification performance of the fully-polarimetric network for the ratio normalised data shows that in order to properly exploit the polarimetric information, more complex polarimetric features and/or networks are likely needed.

Figs. 5.17a and 5.17b show the confusion matrices for the decibel normalised input networks generated by summing the classification results of all 5 classifiers of their corresponding test sets. Fig. 5.17a shows the results for the fully-polarised classifier, while Fig. 5.17b shows the results for the single-polarised classifier. It can be seen that for both classifiers most misclassifications occur between cyclists and motorcyclists. This is expected as the shapes of the range-velocity signatures of cyclists and motorcyclists are similar to each other. Similar behaviour is observed for the ratio based fully- and single-polarised classifiers shown in Figs. 5.18a and 5.18b, respectively.

To summarize, Table 5.2 shows the F1-scores achieved by the networks. It can be seen that the F1-scores of all classes are relatively similar, with the F1-scores for the motorcyclist being the lowest. This can be explained by this class having the least available frames for training and testing out of all classes, while having a similar signature as the cyclist. Furthermore, it can be seen that the F1-scores are highest for the single-polarised ratio normalised input classifier, thus further reaffirming the explanation provided in the previous paragraphs.

Finally, the importance of the cross-polar polarimetric channels for classification is con-

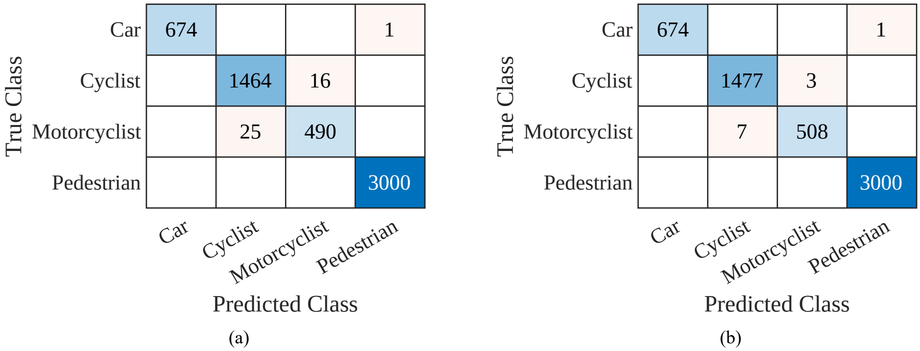

Figure 5.18: Confusion matrix for classification using the ratio normalised input data format with: (a) All polarimetric channels; (b) Only a single polarimetric channel.

Table 5.2: F1-scores achieved by fully- and single-polarised classifiers using decibel and ratio normalised input data.

	dB Scaled		**Ratio Scaled**	
	Full	**Single**	**Full**	**Single**
Car	0.999	0.999	0.999	0.999
Cyclist	0.982	0.971	0.986	0.997
Motorcyclist	0.949	0.917	0.960	0.990
Pedestrian	1.000	1.000	1.000	1.000

sidered. To this end, instead of training the single-polarised decibel-normalised network with only the PP-polarised polarimetric channel, this network was modified by adding and extra input layer for the NN-polarised channel. This resulted in F1-scores of 99.9%, 97.7%, 93.7%, and 100% for the car, cyclist, motorcyclist, and pedestrian class, respectively. From this, it can be concluded that there is indeed to a certain extent information present in the depolarisation caused by a target, as the F1-scores are slightly lower than those obtained with its fully polarised counterpart and slightly higher than its single-polarised version.

5.6. Conclusions

In this chapter, a novel method for classifying vulnerable road users using polarimetric MIMO radar is proposed. To this end, a signal processing pipeline was proposed using virtual channels that correspond to the same polarimetric channel. The method comprises of range-velocity processing using fast Fourier transforms and angular processing using digital beam forming, including a velocity dependent phase correction to account for phase changes of moving targets that occur due to time division multiplexing used in automotive radar. To reduce loss of angular resolution that occurs when using a polarimetric radar, a combined polarimetric channel processing method is also introduced. This method allows to successfully enhance the angular resolution compared to single polarimetric channel processing. It is also shown that when a radar system provides good polarimetric diversity, it is possible to outperform single-polarised radar systems for targets that have low returns in the polarimetric channel of the single-polarised system while providing a strong return in others.

This processing pipeline has been applied to the data coming from a polarimetric MIMO automotive radar, which was developed in collaboration with Huber+Suhner AG based on the AWR2243BOOST module by Texas Instruments. The developed radar uses a diagonal polarisation basis and is calibrated using a new active calibration method, allowing to calibrate all virtual channels at once, independent of polarisation. Using this radar system, multiple different moving target classes were measured, namely: pedestrian, cyclist, motorcyclist, and car. From their measurements, multiple different polarimetric features were extracted and analysed. It is found that the polarisation ratios of pedestrians are relatively high, while other classes comparatively provide more cross-polar backscattering.

Using exclusively the proposed feature of target polarimetric power, it is shown that a Bayesian classifier was able to achieve an F1-score of 94.7%, 87.3%, 63.2%, and 64.2% for cars, pedestrians, motorcyclists, and cyclists, respectively. It is found that by not including the polarimetric properties, the F1-scores of the VRU classes dropped significantly, especially in the case of cyclists, which decreased from 64.2% to 6.7%. The F1-scores for pedestrians and motorcyclists dropped from 87.3% to 73.0% and from 63.2% to 34.2% respectively. From this, it can be concluded that polarimetric information provides beneficial information for VRU classification and that it can be used to boost classification performance compared to single-polarised radar systems. Additionally, a CNN-based classifier was also used to classify the measured targets, exploiting the ’spatial’ distribution of polarimetric features in their range-velocity spectra. Here, it was found that polarimetric radar is beneficial as it is able to provide clearer range-velocity signatures due to polarisation diversity. To fully exploit polarimetric information available in range-velocity signatures, more complex polarimetric features and/or a more complex network architecture are likely required.

6

Conclusions

6.1. Major Results and Novel Contributions

The major results and contributions of this PhD research are discussed in the paragraphs below.

- **For the first time, statistical full-wave numerical results of scattering from road surfaces in automotive scenarios in the W-band are presented. (Chapter 2)**

  Based on computer tomography scans, the surface properties of an asphalt road surface sample were determined. From these scans, a root-mean-square height of approximately 2 mm and a correlation length of about 2 mm were found, thus leading to a root-mean-square slope of approximately 1. This high value of the RMS slope makes it impossible to analyse scattering from asphalt using well-known approximations (SPM, KA, etc.) and only full-wave simulations could be used. Furthermore, it was found that the surface height profile can follow non-Gaussian distributions and that asphalt material is a lossy dielectric, possessing a relative permittivity ranging from 3 to 5 with a conductivity of approximately 0.5 to 0.7 S/m in the 77 GHz automotive radar band.

  These geometrical properties present significant surface roughness at frequencies of 77 GHz used in automotive radar applications, rendering well-known approximate analytical methods such as the small perturbation method and born approximation invalid, which are widely used to evaluate the backscattering behaviour of electromagnetic rough surfaces.

  Thus, to overcome this problem and to provide data on backscattering from road surfaces, which is essential for the development of, amongst others, road surface clutter analysis in automotive radar, a Monte-Carlo based full-wave simulation procedure using a novel algorithm for generating rough surface realisations was introduced. Using this procedure, for the first time statistical data on bi-static surface scattering from road surfaces were obtained and presented.

- **A novel road surface scattering modelling method for mm-wave automotive radar systems based on a dense grid of uncorrelated scattering elements has been introduced. (Chapter 2)**

  As simulation of radar returns in automotive scenarios becomes increasingly important for increasingly complex applications, so does the need for fast and accurate models of road surface scattering. Nowadays, most automotive radar simulators neglect road surface scattering or evaluate its effect using computationally-intensive methods such as ray-tracing. To address this issue, a novel method for simulating road surface scattering based on uncorrelated scattering elements is proposed. This method is able to generate radar data from road surface scattering in different formats which are crucial for subsequent processing such as range-Doppler spectra and range-angle plots. It is found that the proposed method shows excellent agreement with measurement results from real-world automotive radar recordings, thus demonstrating the effectiveness of the proposed method.

- **A new measurement procedure has been proposed for measuring normalised radar cross sections of rough surfaces, showing that road surfaces have dis-**

tinct polarimetric normalised radar cross sections depending on their condition. (Chapters 3 and 4)

Currently, no statistical models of polarimetric normalised radar cross sections of road surfaces based on measurement data in the 77 GHz automotive radar are presented in the literature.

To address this gap, a novel measurement procedure is proposed that is able to determine the polarimetric normalised radar cross sections of rough surfaces including its statistical properties. The measurement procedure involves measurements with a vector network analyser connected to a dual-polarised horn antenna and subsequently compensates the raw measurement data for the effects of the antenna radiation patterns and the strongly increasing propagation distance over the surface-under-test.

The proposed measurement procedure is applied to road surfaces in various conditions and it is shown that their normalised radar cross sections show a strong dependency on said road surface conditions. It is found that, depending on the road surface condition, surface backscattering behaviour can vary from Lamberian scattering behaviour, corresponding to very rough surfaces, to significant differences of 10 dB between horizontally and vertically polarised co-polar normalised radar cross sections, as found in the case of wet asphalt. Furthermore, it is shown that the cross-polar normalised radar cross sections are significantly lower than the co-polar normalised radar cross sections, ranging from 5 dB to over 10 dB depending on polarisation and incident angle, indicating that multiple scattering events play a limited role in the total backscattering response. Also, based on the found statistical models of normalised radar cross sections of surfaces, a method to maximise or suppress surface scattering by varying the sensing wave polarisation in a single-polarised radar system is proposed.

- **A novel road surface condition classification method based on an adapted polarimetric $H\alpha A$-decomposition has been introduced that exploits the differences in the statistical properties of polarimetric scattering of various road surface conditions. (Chapter 4)**

  Due to the short wavelength and resulting significant electromagnetic roughness of road surfaces, surface backscattering can be detected by 77 GHz radar systems. As the backscattered signal from the surface to the radar depends on the road surface condition, this information can be used to classify the road surface condition ahead of the vehicle which subsequently can be used to enhance road user safety. As the backscattering response from road surfaces has distinct polarimetric properties depending on the road surface condition, the extra information provided by a polarimetric radar system can be used to increase accuracy and reliability of classifications. The polarimetric features proposed so far in literature only utilise the available full breath of polarimetric information to a limited extent.

  Thus, to better exploit the rich statistical polarimetric information present in backscattering from road surfaces, a new method to extract three polarimetric features, namely entropy H, angle α, and anisotropy A, in automotive scenarios and corresponding shallow incident angles is proposed. It is shown that the proposed features result in potentially more reliable and robust classifications as the difference between cluster centroids in the $H\alpha A$ space is increased by at least 16% for measurements performed at 90° compared to clusters formed by polarimetric ratios, while not sacrificing cluster standard deviations significantly.

- **For the first time, it has been shown that the dynamic polarimetric signatures of cyclists and pedestrians are structured and differ significantly from each other (Chapters 5)**

  Using a novel automotive polarimetric MIMO radar developed in collaboration with Huber+Suhner AG, measurements of multiple pedestrians and cyclists, moving in various directions, have been performed. These measurements showed that the mean polarimetric ratio, which is computed based on all polarimetric ratios of the individual detections within a frame that correspond to the VRU-under-test, significantly differs between pedestrians and cyclists. It was also shown that the polarimetric ratios of the individual detections belonging to a measured target within a range-Doppler frame are structured to a certain degree, thus indicating that several parts of the observed target have different polarimetric responses.

  This implies that polarimetric radar can enhance classification performance of vulnerable road users by considering the polarimetric features of the observed targets in addition to using the features available to single-polarised radar. This is demonstrated by improvements in class F1-scores from 73.0% to 87.3%, 34.2% to 63.2%, and from 6.7% to 64.2% for respectively pedestrians, motorcyclists, and cyclists, achieved by using polarimetric features based on all four polarimetric channels compared to using the same feature, but computed from only a single polarimetric channel using a Bayesian classifier.

  Furthermore, a convolutional neural network classifier was used to evaluate the effectiveness of the structure of the dynamic polarimetric signatures belonging to VRUs for classification purposes. Here, it was also found that polarimetric radar is beneficial as improvements in F1-scores from 97.1% to 98.2% and 91.7% to 94.9% for respectively cyclists and motorcyclists were achieved with respect to the single-polarised version of the convolutional neural network. These improvements are likely caused by not only the information provided by the polarisation of the backscattered waves from a target but also the polarimetric diversity provided by a fully polarimetric radar. Namely, polarimetric radar is able to detect reflections in other polarimetric channels which may be too weak to be detected in the single polarimetric channel that a single-polarised radar uses. This leads to higher quality range-velocity signatures, which in turn enhance the classification performance. The information provided by polarisation can likely further be exploited by using more complex polarimetric features and/or more complex network architectures.

6.2. Recommendations for Future Research

Several research topics of interest in continuation of the research presented in this dissertation are listed below.

- **Study on statistical road surface scattering from road surfaces covered by another dielectric medium using full-wave methods.**

The rough surface types evaluated in this dissertation with the proposed full-wave simulation procedure comprise of PEC or dielectric rough surfaces, representing road surfaces under normal conditions. It is of interest to also investigate the polarimetric radar cross sections of surfaces in non-dry conditions, such as wet or icy, by placing a second dielectric on top of the original investigated surfaces. The results from this study could be further used for investigations on the benefits of polarimetry in automotive radar.

- **Collection of a polarimetric automotive radar dataset of city/highway driving.**

  To take the proposed methods of surface conditions feature extraction and road surface characterisation to the next technology readiness level, it is imperative that they are tested in real world scenarios. This could be done by mounting the H+S radar on a car with corresponding reference sensors and capture data while driving through the city or on a highway. At the moment, to the author's best knowledge, there are no publicly available automotive polarimetric radar datasets available and when such a dataset would be collected it could, besides road surface classification, also be used to investigate the classification of vulnerable road users.

- **More detailed study on performance of H, α, and A features for scattering from vulnerable road users.**

  In this dissertation, mainly polarimetric scattering from road surfaces has been considered. However, vulnerable road users pose interesting targets as well and can also have distinctive polarimetric properties that can be used for classification as shown in chapter 5. In this chapter, H, α, and A features are computed using all detections within a frame which correspond to different scattering processes. A more intricate signal processing pipeline to perform the $H\alpha A$-decomposition over multiple frames but same areas of the observed target, with the same scattering properties, may result in an improved quality of the H, α, and A features which could increase classification performance of VRUs further.

- **Evaluation of performance of various machine learning algorithms for road surface classification using polarimetric features.**

  In this dissertation, the H, α, and A and polarimetric ratio features were studied on cluster levels to keep the results of the analysis as general applicable as possible. The next step in this investigation would be to use these polarimetric features, possibly in combination with others such as the Krogager decomposition, normalised amplitude A, and phase difference δ, in various machine learning algorithms, which may be able to pick up on more intricate relations beyond distances between cluster centroids and cluster standard deviations, to evaluate and enhance classification accuracy.

- **Implementation of an automotive polarimetric radar system with increased aperture size and an increased amount of polarimetric channels.**

  Implementation of a high angular-resolution automotive polarimetric radar system would be interesting as it potentially can allow to separate scattering points of a target-of-interest more compared to a low-resolution radar sensor. This would also allow classification based on the geometric relationships between certain types of scattering points. For example, the arms and the torso of a pedestrian could have distinct polarimetric scattering behaviour, and the geometrical relationship between these body parts could be exploited to increase accuracy of a classifying algorithm.

Bibliography

[1] *Global Status Report on Road Safety 2023*. Geneva: World Health Organization, 2023.

[2] W. Bouwmeester, F. Fioranelli, and A. Yarovoy, "Road Surface Conditions Identification via HαA Decomposition and Its Application to mm-Wave Automotive Radar," *IEEE Transactions on Radar Systems*, pp. 132–145, 2023.

[3] J. Hasch, E. Topak, R. Schnabel, T. Zwick, R. Weigel, and C. Waldschmidt, "Millimeter-Wave Technology for Automotive Radar Sensors in the 77 GHz Frequency Band," *IEEE Transactions on Microwave Theory and Techniques*, vol. 60, no. 3, pp. 845–860, Mar. 2012.

[4] K. Sarabandi, E. Li, and A. Nashashibi, "Modeling and measurements of scattering from road surfaces at millimeter-wave frequencies," *IEEE Transactions on Antennas and Propagation*, vol. 45, no. 11, pp. 1679–1688, Nov. 1997.

[5] E. Li and K. Sarabandi, "Low grazing incidence millimeter-wave scattering models and measurements for various road surfaces," *IEEE Transactions on Antennas and Propagation*, vol. 47, no. 5, pp. 851–861, May 1999.

[6] A. Bystrov, E. Hoare, T.-Y. Tran, N. Clarke, M. Gashinova, and M. Cherniakov, "Automotive System for Remote Surface Classification," *Sensors*, vol. 17, no. 4, p. 745, Apr. 2017.

[7] P. Asuzu and C. Thompson, "Road condition identification from millimeter-wave radar backscatter measurements," in *2018 IEEE Radar Conference (RadarConf18)*, Apr. 2018, pp. 0012–0016.

[8] W. Peake, "Theory of radar return from terrain," in *1958 IRE International Convention Record*, vol. 7, Mar. 1959, pp. 27–41.

[9] G. P. G. P. Kulemin, *Millimeter-Wave Radar Targets and Clutter*, ser. Artech House Radar Library. Boston: Artech House, 2003.

[10] R. Schneider, "MILLIMETER-WAVE IMAGES OF TRAFFIC SCENES AND THEIR AUTOMATIC INTERPRETATION," *M+RF97 Microwave and Communications Technologies Conference (1997 : London, England). Proceedings of Microwave and Communication Technology*, 1997.

[11] J. A. Ogilvy, *Theory of wave scattering from random rough surfaces*. Bristol, England ;: A. Hilger, 1991.

[12] P. Hindle, “Comprehensive Survey of 77, 79 GHz Automotive Radar Companies – Sensors and ICs,” *Microwave Journal*, Mar. 2020.

[13] G. Hakobyan and B. Yang, “High-Performance Automotive Radar: A Review of Signal Processing Algorithms and Modulation Schemes,” *IEEE Signal Processing Magazine*, vol. 36, no. 5, pp. 32–44, Sep. 2019.

[14] S. Trummer, G. F. Hamberger, R. Koerber, U. Siart, and T. F. Eibert, “Performance analysis of 79 GHz polarimetric radar sensors for autonomous driving,” in *2017 European Radar Conference (EURAD)*, Oct. 2017, pp. 41–44.

[15] H. Iqbal, F. Bögelsack, and C. Waldschmidt, “Polarimetric RCS analysis of traffic objects,” in *2017 European Radar Conference (EURAD)*, Oct. 2017, pp. 49–52.

[16] V. Vassilev, “Road Surface Recognition at mm-Wavelengths Using a Polarimetric Radar,” *IEEE Transactions on Intelligent Transportation Systems*, vol. 23, no. 7, pp. 6985–6990, Jul. 2022.

[17] S. M. Sabery, A. Bystrov, P. Gardner, A. Stroescu, and M. Gashinova, “Road Surface Classification Based on Radar Imaging Using Convolutional Neural Network,” *IEEE Sensors Journal*, vol. 21, no. 17, pp. 18 725–18 732, Sep. 2021.

[18] C. Schüßler, M. Hoffmann, J. Bräunig, I. Ullmann, R. Ebelt, and M. Vossiek, “A Realistic Radar Ray Tracing Simulator for Large MIMO-Arrays in Automotive Environments,” *IEEE Journal of Microwaves*, vol. 1, no. 4, pp. 962–974, Oct. 2021.

[19] D. He, K. Guan, B. Ai, Z. Zhong, J. Kim, H. Chung, and A. Hrovat, “Channel Measurement and Ray-Tracing Simulation for 77 GHz Automotive Radar,” *IEEE Transactions on Intelligent Transportation Systems*, vol. 24, no. 7, pp. 7746–7756, Jul. 2023.

[20] M. M. Zaky and K. Sarabandi, “Fully Coherent Electromagnetic Scattering Computation for Snowpacks Based on Statistical S-Matrix Approach,” *IEEE Transactions on Geoscience and Remote Sensing*, vol. 59, no. 8, pp. 6336–6345, Aug. 2021.

[21] G. Di Martino, A. Iodice, D. Poreh, and D. Riccio, “Pol-SARAS: A Fully Polarimetric SAR Raw Signal Simulator for Extended Soil Surfaces,” *IEEE Transactions on Geoscience and Remote Sensing*, vol. 56, no. 4, pp. 2233–2247, Apr. 2018.

[22] M. M. Tajdini, B. Gonzalez-Valdes, J. A. Martinez-Lorenzo, A. W. Morgenthaler, and C. M. Rappaport, “Real-Time Modeling of Forward-Looking Synthetic Aperture Ground Penetrating Radar Scattering From Rough Terrain,” *IEEE Transactions on Geoscience and Remote Sensing*, vol. 57, no. 5, pp. 2754–2765, May 2019.

[23] V. Volosyuk, V. Pavlikov, M. Nechyporuk, S. Zhyla, N. Ruzhentsev, and V. Kosharskyi, “Optimal Algorithms Synthesis for Polarization Selection of Useful Signals on the Background of Passive Interference in Synthetic Aperture Radars,” in *2020 IEEE International Conference on Problems of Infocommunications. Science and Technology (PIC S&T)*, Oct. 2020, pp. 452–456.

[24] L. Iannini, D. Comite, N. Pierdicca, and P. Lopez-Dekker, “Rough-Surface Polarimetry in Companion SAR Missions,” *IEEE Transactions on Geoscience and Remote Sensing*, vol. 60, pp. 1–15, 2022.

[25] M. Giallorenzo, X. Cai, A. Nashashibi, and K. Sarabandi, “Radar Backscatter Measurements of Road Surfaces at 77 GHz,” in *2018 IEEE International Symposium on Antennas and Propagation & USNC/URSI National Radio Science Meeting*, Jul. 2018, pp. 2421–2422.

[26] X. Meng, P. Li, Y. Hu, F. Song, and J. Ma, “Theoretical Study on Recognition of Icy Road Surface Condition by Low-Terahertz Frequencies,” *IEEE Transactions on Geoscience and Remote Sensing*, vol. 60, pp. 1–9, 2022.

[27] T. J. Douglas, A. Y. Nashashibi, M. Kashanianfard, and K. Sarabandi, “Polarimetric Backscatter Measurements of Road Surfaces at J-Band Frequencies for Standoff Road Condition Assessment,” in *2021 IEEE USNC-URSI Radio Science Meeting (Joint with AP-S Symposium)*, Dec. 2021, pp. 35–36.

[28] V. V. Viikari, T. Varpula, and M. Kantanen, “Road-Condition Recognition Using 24-GHz Automotive Radar,” *IEEE Transactions on Intelligent Transportation Systems*, vol. 10, no. 4, pp. 639–648, Dec. 2009.

[29] W. Bouwmeester, F. Fioranelli, and A. Yarovoy, “Statistical Polarimetric RCS Model of an Asphalt Road Surface for mm-Wave Automotive Radar,” in *2023 20th European Radar Conference (EuRAD)*, Sep. 2023, pp. 18–21.

[30] ——, “Dynamic Road Surface Signatures in Automotive Scenarios,” in *2021 18th European Radar Conference (EuRAD)*, Apr. 2022, pp. 285–288.

[31] C. A. Balanis, *Antenna Theory: Analysis and Design*, 4th ed. Hoboken, New Jersey: Wiley, 2016.

[32] J.-S. Lee and E. Pottier, *Polarimetric Radar Imaging: From Basics to Applications*. Boca Raton: CRC Press, Jan. 2017.

[33] X. R. Nogueira and J. Mennis, “The Effect of Brick and Granite Block Paving Materials on Traffic Speed,” *International Journal of Environmental Research and Public Health*, vol. 16, no. 19, p. 3704, Oct. 2019.

[34] W. Bouwmeester, F. Fioranelli, and A. G. Yarovoy, “Statistical Modeling of Polarimetric RCS of Road Surfaces for Scattering Simulation and Optimal Antenna Polarization Determination,” *IEEE Journal of Selected Topics in Applied Earth Observations and Remote Sensing*, vol. 17, pp. 3078–3090, 2024.

[35] E. Šabanovič, V. Žuraulis, O. Prentkovskis, and V. Skrickij, “Identification of Road-Surface Type Using Deep Neural Networks for Friction Coefficient Estimation,” *Sensors*, vol. 20, no. 3, p. 612, Jan. 2020.

[36] S. M. Sabery, A. Bystrov, P. Gardner, and M. Gashinova, “Surface Classification Based on Low Terahertz Radar Imaging and Deep Neural Network,” in *2020 21st International Radar Symposium (IRS)*, Oct. 2020, pp. 24–27.

[37] Y. Xiao, S. Cassidy, L. Daniel, S. Pooni, M. Cherniakov, and M. Gashinova, “Universal Image Segmentation Framework on High Resolution Automotive Radar Map,” in *IET Radar Conference*, Oct. 2022.

[38] S. Cloude and E. Pottier, “An entropy based classification scheme for land applications of polarimetric SAR,” *IEEE Transactions on Geoscience and Remote Sensing*, vol. 35, no. 1, pp. 68–78, Jan. 1997.

[39] M. Martorella, E. Giusti, L. Demi, Z. Zhou, A. Cacciamano, F. Berizzi, and B. Bates, “Target Recognition by Means of Polarimetric ISAR Images,” *IEEE Transactions on Aerospace and Electronic Systems*, vol. 47, no. 1, pp. 225–239, Jan. 2011.

[40] G. Zhang, V. N. Mahale, B. J. Putnam, Y. Qi, Q. Cao, A. D. Byrd, P. Bukovcic, D. S. Zrnic, J. Gao, M. Xue, Y. Jung, H. D. Reeves, P. L. Heinselman, A. Ryzhkov, R. D. Palmer, P. Zhang, M. Weber, G. M. Mcfarquhar, B. Moore, Y. Zhang, J. Zhang, J. Vivekanandan, Y. Al-Rashid, R. L. Ice, D. S. Berkowitz, C.-c. Tong, C. Fulton, and R. J. Doviak, “Current Status and Future Challenges of Weather Radar Polarimetry: Bridging the Gap between Radar Meteorology/Hydrology/Engineering and Numerical Weather Prediction,” *Advances in Atmospheric Sciences*, vol. 36, no. 6, pp. 571–588, Jun. 2019.

[41] Petr. Beckmann and André. Spizzichino, *The scattering of electromagnetic waves from rough surfaces*, ser. International series of monographs on electromagnetic waves ; v. 4. Goford: Pergamon Press; [distributed in the Western Hemisphere by Macmillan, New York], 1963.

[42] J. Häkli, J. Säily, P. Koivisto, I. Huhtinen, T. Dufva, A. Rautiainen, H. Toivanen, and K. Nummila, “Road surface condition detection using 24 GHz automotive radar technology,” in *2013 14th International Radar Symposium (IRS)*, vol. 2, Jun. 2013, pp. 702–707.

[43] “WR-12 Waveguide Dual-Polarized Horn Antenna,” https://www.eravant.com/15-dbi-gain-60-to-90-ghz-45-db-isolation-wr-12-waveguide-e-band-dual-polarized-horn.

[44] “Conversion Chart Abrasives - Grit Sizes | FINE TOOLS,” https://www.fine-tools.com/G10019.html, Nov. 2022.

[45] P. Leroux, “Sandpaper Roughness Measurement Using 3D Profilometry,” Tech. Rep., Jan. 2014.

[46] J. Dunsmore, “Gating effects in time domain transforms,” in *2008 72nd ARFTG Microwave Measurement Symposium*, Dec. 2008, pp. 1–8.

[47] M. v. I. en Waterstaat, "Actuele verkeersongevallencijfers," http://www.rijkswaterstaat.nl/wegen/wegbeheer/onderzoek/verkeersveiligheid-en-ongevallencijfers/actuele-verkeersongevallencijfers.

[48] M. Dimitrievski, I. Shopovska, D. V. Hamme, P. Veelaert, and W. Philips, "Weakly Supervised Deep Learning Method for Vulnerable Road User Detection in FMCW Radar," in *2020 IEEE 23rd International Conference on Intelligent Transportation Systems (ITSC)*, Sep. 2020, pp. 1–8.

[49] D. Wachtel, J. Edler, S. Schröder, S. Queiroz, and W. Huber, "Convolutional Neural Network Classification of Vulnerable Road Users based on Micro-Doppler Signatures using an Automotive Radar," in *2022 IEEE 25th International Conference on Intelligent Transportation Systems (ITSC)*, Oct. 2022, pp. 866–872.

[50] R. Pérez, F. Schubert, R. Rasshofer, and E. Biebl, "Single-Frame Vulnerable Road Users Classification with a 77 GHz FMCW Radar Sensor and a Convolutional Neural Network," in *2018 19th International Radar Symposium (IRS)*, Jun. 2018, pp. 1–10.

[51] P. Rippl, J. Iberle, and T. Walter, "Classification of Vulnerable Road Users Based on Spectrogram Autocorrelation Features," in *2021 18th European Radar Conference (EuRAD)*, Apr. 2022, pp. 293–296.

[52] R. Prophet, M. Hoffmann, A. Ossowska, W. Malik, C. Sturm, and M. Vossiek, "Image-Based Pedestrian Classification for 79 GHz Automotive Radar," in *2018 15th European Radar Conference (EuRAD)*, Sep. 2018, pp. 75–78.

[53] G. F. Hamberger, S. Späth, U. Siart, and T. F. Eibert, "A Mixed Circular/Linear Dual-Polarized Phased Array Concept for Automotive Radar—Planar Antenna Designs and System Evaluation at 78 GHz," *IEEE Transactions on Antennas and Propagation*, vol. 67, no. 3, pp. 1562–1572, Mar. 2019.

[54] A. Tinti, S. T. Alfageme, S. D. Biarge, and N. Pohl, "Full Polarimetric Antenna System for Automotive Radar," in *2023 IEEE Topical Conference on Wireless Sensors and Sensor Networks*, Jan. 2023, pp. 39–42.

[55] S. Trummer, G. F. Hamberger, U. Siart, and T. F. Eibert, "A polarimetric 76–79 GHz radar-frontend for target classification in automotive use," in *2016 European Radar Conference (EuRAD)*, Oct. 2016, pp. 346–349.

[56] Z. Zang, Q. Ren, A. Uz Zaman, and J. Yang, "77 GHz Fully Polarimetric Antenna System With Compact Circularly Polarized Slots in Gap Waveguide for Automotive Radar," *IEEE Transactions on Antennas and Propagation*, vol. 72, no. 7, pp. 5578–5588, Jul. 2024.

[57] A. Tinti, S. Tejero Alfageme, S. Duque Biarge, J. Balcells-Ventura, and N. Pohl, "Fully Polarimetric Automotive Radar: Proof of Concept," *IEEE Transactions on Radar Systems*, vol. 2, pp. 645–660, 2024.

[58] A. Y. Nashashibi, T. J. Douglas, M. Kashanianfard, S. W. Decker, and K. Sarabandi, "High-Resolution Polarimetric Radar for Autonomous Vehicle Research at W-Band Frequencies," *IEEE Transactions on Radar Systems*, vol. 2, pp. 632–644, 2024.

[59] J. F. Tilly, O. Schumann, F. Weishaupt, J. Dickmann, and G. Waniliek, "Polarimetric Information Representation for Radar based Road User Detection with Deep Learning," in *2021 IEEE 24th International Conference on Information Fusion (FUSION)*, Nov. 2021, pp. 1–6.

[60] J. F. Tilly, F. Weishaupt, O. Schumann, J. Dickmann, and G. Wanielik, "Road User Classification with Polarimetric Radars," in *2020 17th European Radar Conference (EuRAD)*, Jan. 2021, pp. 112–115.

[61] O. Schumann, J. Lombacher, M. Hahn, C. Wöhler, and J. Dickmann, "Scene Understanding With Automotive Radar," *IEEE Transactions on Intelligent Vehicles*, vol. 5, no. 2, pp. 188–203, Jun. 2020.

[62] J. F. Tilly, F. Weishaupt, O. Schumann, J. Dickmann, and G. Wanielik, "Road User Detection on Polarimetric Pre-CFAR Radar Data Level," *IEEE Robotics and Automation Letters*, vol. 8, no. 6, pp. 3558–3565, Jun. 2023.

[63] F. Weishaupt, J. F. Tilly, N. Appenrodt, P. Fischer, J. Dickmann, and D. Heberling, "Landmark-Based Vehicle Self-Localization Using Automotive Polarimetric Radars," *IEEE Transactions on Intelligent Transportation Systems*, pp. 1–18, 2024.

[64] T. Visentin, J. Hasch, and T. Zwick, "Polarimetric RCS Measurements of Selected Two-Wheeled Vehicles for Automotive Radar," in *2017 European Radar Conference (EURAD)*, Oct. 2017, pp. 53–56.

[65] K. Geary, J. S. Colburn, A. Bekaryan, S. Zeng, B. Litkouhi, and M. Murad, "Automotive radar target characterization from 22 to 29 GHz and 76 to 81 GHz," in *2013 IEEE Radar Conference (RadarCon13)*, Apr. 2013, pp. 1–6.

[66] T. Visentin, A. Sagainov, J. Hasch, and T. Zwick, "Classification of objects in polarimetric radar images using CNNs at 77 GHz," in *2017 IEEE Asia Pacific Microwave Conference (APMC)*, Nov. 2017, pp. 356–359.

[67] J. Bechter, F. Roos, and C. Waldschmidt, "Compensation of Motion-Induced Phase Errors in TDM MIMO Radars," *IEEE Microwave and Wireless Components Letters*, vol. 27, no. 12, pp. 1164–1166, Dec. 2017.

[68] U. Huegel, A. Garcia-Tejero, R. Glogowski, E. Willmann, M. Pieper, and F. Merli, "3D Waveguide Metallized Plastic Antennas Aim to Revolutionize Automotive Radar," *Microwave Journal*, Aug. 2022.

[69] A. Garcia-Tejero, F. R. Varela, R. Torres-Sánchez, M. Burgos-Garcia, and F. Merli, "Wideband Untilted Narrow Wall Slotted Partially Staggered Waveguide Array Based on Metallized Molded Plastic at E-Band," *IEEE Antennas and Wireless Propagation Letters*, vol. 23, no. 3, pp. 915–919, Mar. 2024.

[70] A. Garcia-Tejero, M. Burgos-Garcia, and F. Merli, “Broadband Metalized Plastic Waveguide Antenna with Robust Isolation Interface at 77 GHz,” *IEEE Antennas and Wireless Propagation Letters*, pp. 1–5, 2024.

[71] C. Zhao, A. Garcia-Tejero, W. Bouwmeester, Y. Aslan, O. Krasnov, and A. Yarovoy, “Calibration of Polarimetric Automotive Radar with Asymmetric MIMO Topology and Off-Broadside Beamforming,” in *Accepted for EuRAD 2024*, Paris, 2024.

[72] F. Weishaupt, J. F. Tilly, N. Appenrodt, J. Dickmann, and D. Heberling, “Calibration and Signal Processing of Polarimetric Radar Data in Automotive Applications,” in *2022 Microwave Mediterranean Symposium (MMS)*, May 2022, pp. 1–6.

[73] W. Bouwmeester, F. Fioranelli, and A. Yarovoy, “Dataset of Moving Vulnerable Road Users and Vehicle Using a Fully Polarimetric mm-Wave MIMO Radar.”

Acknowledgements

First of all I would like to thank my promoter and committee chair, Prof. DSc. Olexander Yarovyi. He has not only guided me through my PhD programme, but has also taught many courses I took part in during my Master's degree as well as supervised me during my Master graduation project. Therefore, I can safely consider him as my scientific farther and I am very thankful for all his guidance that he has given me, the things he has taught me, and all the interesting discussions we have had over the years.

Another person that has been invaluable for me during this PhD programme is my second promoter and daily supervisor, dr. Francesco Fioranelli. I am very grateful for his guidance and advice that he has provided. He has taught me many important skills, such as how to deal with reviews, has helped me hone my scientific writing skills, and how to navigate through many other academic processes. I would like to thank him for his high degree of availability, I could always drop by his office for questions and discussions and I never had to wait long to receive a response on e-mail. I have enjoyed working with him very much and I could not have wished for a better daily supervisor.

I would also like to thank my doctoral committee members Prof. dr. ir. Geert Leus, Prof. dr. ir. Herman Russchenberg, dr. ir. Rob Remis, Prof. dr. Cicero Vaucher, and Prof. dr. Laurent Ferro-Famil, for taking the time to read my dissertation and attending my defence. Also, the effort and time invested by the members, especially those from abroad to be present in Delft, has not gone unnoticed.

I would like to extend my thanks to the academic and supporting staff of the Microwave Sensing, Signals, and Systems (MS3) group. Without them, it would have been impossible to conduct my research. Special thanks goes to Esther de Klerk and Minke van der Put for their handling of all administrative matters and ing. Fred van der Zwan, ir. Peter Swart, ir. Pascal Aubry, and dr. Oleg Krasnov for their help with the measurements that have been instrumental to my work over the last few years.

I am also grateful to ing. Antoon Frehe, Frans Broos, and drs. Frank Everdij for their help with the IT infrastructure and getting the EM software suite I used during this PhD project running on the DelftBlue supercomputer.

Special thanks goes to Alejandro Garcia-Tejero from Huber+Suhner AG for his efforts and help in realising a fully polarimetric automotive radar system. This specific radar system has been pivotal in my own research and I suspect that many more interesting measurements will be performed with it. A special commendation goes to Changxu Zhao for developing a calibration method which has led to a joint publication.

I would like to extend my gratitude to dr. Katerina Varveri for sharing her expertise and resources regarding asphalt pavement. The samples as well as the CT-scans provided by her have been essential to my research on electromagnetic scattering from road surfaces.

Over the years I have also supervised a number of students whom I would like to thank. I would like to extend my gratitude to Yue Chen, Bet Rufas Talamas, Huixuan Chen, and Fan Lei for their help with surface scattering simulations and measurements.

A special mention goes out to Huawei Sweden for the fruitful discussions we had and the feedback and support they provided.

A warm thanks goes out to my fellow PhD candidates for all the laughs we shared, discussions we had, and help they provided. A special mention for Simin Zhu, Ignacio Roldan-Montero, Apostolos Pappas, Rutkay Güneri, Mareike Wendelmuth, and Berk Onat for being willing test-subjects in my measurement campaigns. I also thank my office mates, Ignacio, Simin, and Rutkay, for the many rabbit holes we dived into, but always emerged from with stronger fundamental knowledge.

Last but not least I would like to thank my friends from high school, friends from my student association, friends from my solar car racing days, my girlfriend, and my parents for their company and support. Without them, it would have been a very long four years.

About the Author

Wietse Bouwmeester received the B.Sc. degree in electrical engineering from the Delft University of Technology, Delft, The Netherlands, in 2016, the M.Sc. degree in electrical engineering from the Delft University of Technology in 2020, with a focus on telecommunications and sensing systems (cum laude), focusing on the design of a conformal phased array antenna commissioned by ASTRON, the Dutch institute for radio astronomy. In 2020, he joined the Microwave Sensing, Signals and Systems group, TU Delft, as a Ph.D. Candidate, and worked there on polarimetric approaches to classify road surfaces and other targets with mm-Wave radar for automotive applications. Wietse Bouwmeester is going to defend his thesis and obtain his PhD degree from the Delft University of Technology in September 2024.

List of Publications

Journal Papers

3. **W. Bouwmeester**, F. Fioranelli, and A. Yarovoy, “Classification of Dynamic Vulnerable Road Users Using a Polarimetric mm-Wave MIMO Radar”, under review for *IEEE Transactions on Radar Systems*, 2024.

2. **W. Bouwmeester**, F. Fioranelli, and A. Yarovoy, “Statistical Modeling of Polarimetric RCS of Road Surfaces for Scattering Simulation and Optimal Antenna Polarization Determination”, *IEEE Journal of Selected Topics in Applied Earth Observations and Remote Sensing*, 2024.

1. **W. Bouwmeester**, F. Fioranelli, and A. Yarovoy, “Road Surface Conditions Identification via H α A Decomposition and Its Application to mm-Wave Automotive Radar”, *IEEE Transactions on Radar Systems*, 2023.

Conference Proceedings

6. A. Yarovoy, **W. Bouwmeester**, B. Rufas Talamas, and F. Fioranelli, “Numerical Analysis of the MM-Wave Scattering from Randomly Rough Surfaces”, in *International Radar Conference 2024*, Rennes, France, 2024, accepted.

5. C. Zhao, A. Garcia-Tejero, **W. Bouwmeester**, Y. Aslan, O. Krasnov, and A. Yarovoy, “Calibration of Polarimetric Automotive Radar With Asymmetric MIMO Topology and Off-Broadside Beamforming”, in *2024 21th European Radar Conference (EuRAD)*, Paris, France, 2024, accepted.

4. **W. Bouwmeester**, F. Fioranelli, and A. Yarovoy, “Effect of Geometrical Anisotropy on Road Surface Radar Cross Sections”, presented at *International Conference on Microwaves for Intelligent Mobility 2024 (ICMIM)*, Boppard, Germany, 2024.

3. **W. Bouwmeester**, F. Fioranelli, and A. Yarovoy, “Convergence of Scattering Parameters and HαA-Features of Road Surfaces”, in *20th European Radar Conference (EuRAD)*, Berlin, Germany, 2023.

2. **W. Bouwmeester**, F. Fioranelli, and A. Yarovoy, “Statistical Polarimetric RCS Model of an Asphalt Road Surface for mm-Wave Automotive Radar”, in *2023 20th European Radar Conference (EuRAD)*, Berlin, Germany, 2023.

1. **W. Bouwmeester**, F. Fioranelli, and A. Yarovoy, “Dynamic Road Surface Signatures in Automotive Scenarios”, in *2021 18th European Radar Conference (EuRAD)*, London, United Kingdom, 2022.

Datasets

2. **W. Bouwmeester**, F. Fioranelli, and A. Yarovoy, “Dataset of Moving Vulnerable Road Users and Vehicle Using a Fully Polarimetric mm-Wave MIMO Radar”, *4TU.ResearchData*, 2024.

1. **W. Bouwmeester**, F. Fioranelli, and A. Yarovoy, “Dataset of Fully Polarimetric Rough Surface Scattering from Sandpaper and Road Surfaces in Various Conditions Measured at 75 to 85 GHz”, *4TU.ResearchData*, 2023.